

First Studies of the Halo Collimation Needs in the FCC-ee

Author: Maitreyee Mahasweta Moudgalya

Supervisors: Roderik Bruce (CERN) and
Tatiana Pieloni (EPFL-LPAP)

Word Count: 13272

Department of Physics
Imperial College London
July 2021

CERN-THESIS-2021-326
//2021


Abstract

The Future Circular Collider, FCC-ee, is an electron-positron collider that is currently being studied and is designed to be the highest-luminosity high-energy lepton collider to date. The total stored beam energy in the FCC-ee can reach values of up to 20 MJ, which can cause severe damage to accelerator components in the event of beam losses. Therefore a system of halo collimators is required to intercept stray beam particles and localise beam losses away from experiments and sensitive equipment. The purpose of this work was to study the halo collimation needs of the FCC-ee. This was done by creating an aperture model of the accelerator, which defines the shape and size of the physical openings of all the elements. Based on first estimates of the orbit and optics errors, this aperture model was used to calculate the available aperture around the ring, normalised to the transverse local beam size (i.e. in units of RMS beam size "sigma"), for on-momentum and off-momentum particles, in order to identify potential performance bottlenecks. The lowest horizontal and vertical on-momentum aperture bottlenecks were shown to be $14.88\,\sigma$ and $10.26\,\sigma$ respectively, allowing for the collimator jaw openings to be placed at $12\,\sigma$ and $8\,\sigma$ (to guarantee beam "lifetime") as a first minimum estimate of the betatron collimator cuts on the Gaussian tails of the particle beams. The off-momentum aperture studies showed bottlenecks much lower than $10\,\sigma$, motivating the need for a limit of 1.2 and 5.0 to be imposed on the residual beam size growth factor in the horizontal and vertical planes respectively, and for the fractional parasitic dispersion to be corrected to at least 0.02, which could be the goals for local optics corrections. The aperture was also studied in momentum space, and a momentum cut of 3% can be proposed to allow operational margins and guarantee aperture protection. Future iterations of this work should be performed using additional improved corrections of the optics.

Résumé

Le futur collisionneur circulaire d'électrons et positrons, FCC-ee, est actuellement développé pour devenir le collisionneur de leptons à haute énergie à la plus élevée luminosité. L'énergie totale de chaque faisceau stockée dans le FCC-ee peut atteindre des valeurs de 20 MJ, ce qui peut, en cas de perte de faisceau, sérieusement endommager les composants de l'accélérateur. C'est pour cela qu'un système de collimation du faisceau est nécessaire pour intercepter les particules du halo et isoler leur pertes loin des détecteurs installés autours des points de collision et loin des équipements sensibles de l'accélerateur. Le but de ce travail de thèse est d'étudier les besoins de collimation du halo du FCC-ee. Cela a été fait en créant un modèle d'ouverture qui définit la forme et la taille des ouvertures physiques de tous les éléments du collisionneur. Grace à une première estimation des erreurs attendus pour l'orbite et l'optique des particules circulantes en FCC-ee, ce modèle a été utilisé pour calculer l'ouverture disponible autour de l'anneau, normalisée à la taille du faisceau local transversal (c.à.d. en unités de taille faisceau RMS « sigma »), pour les particules dont l'impulsion est égale à l'impulsion nominale et pour celles dont l'impulsion ne l'est pas, afin d'identifier les limitations de performances potentielles. Les plus petites ouvertures horizontales et verticales pour les particules avec l'impulsion nominale sont égaux respectivement à 14.88 σ et à 10.26 σ, permettant aux ouvertures de collimateur d'être placées à 12 σ et 8 σ (ce qui permettrait de garantir une bonne « durée de vie » du faisceau). Cet étude a permi une première estimation des réglages du collimateur halo sur les extrémités gaussiennes des faisceaux de particules pour le FCC-ee. Les calculs d'ouverture pour les particules qui n'ont pas l'impulsion nominale ont permis d'obtenir des ouvertures beaucoup plus bas de 10 σ, motivant ainsi le besoin d'imposer une limite de 1.2 et 5.0 au facteur de croissance résiduel de la taille du faisceau, respectivement dans les plans horizontal et vertical. Le besoin de diminuer la dispersion parasite fractionnaire à au moins 0.02 a aussi été identifié, ce qui définit l'objectif des corrections locales de l'optique. L'ouverture a aussi été étudiée dans l'espace d'impulsion et une coupure d'impulsion de 3% peut être suggérée pour garantir des marges opérationnelles et garantir la protection de l'ouverture. De futures itérations de ce travail devraient être effectuées en utilisant des corrections améliorées de l'optique.

Dedication

This thesis is dedicated to my dearest Friend, Govinda, my dearest Guru, Sri Aurobindo, and my dearest the Mother, to whom my gratitude is best expressed in Sanskrit.

Om Namo Bhagavate Vāsudevāya

Om Namo Bhagavate Sri Aravindāya

Om Ānandamayi Chaitanyamayi Satyamayi Parame

Contents

Preface

For this project, I was mainly working with the Collimation team from CERN, under the supervision of Roderik Bruce and with Tatiana Pieloni from EPFL.

In the work, my tasks involved studying the optical layouts of the accelerator lattice to create the aperture model, which I did using the python scripting language, and then using the model to perform the aperture calculations in MAD-X (a programme used at CERN for the accelerator design), with guidance from Roderik. This involved carefully deciding which estimates of the errors and tolerances to use for the FCC-ee, of which the initial parameters were provided by Tessa Charles (from the FCC-ee collaboration) from her global optics correction studies. We also collaborated with Michael Hofer (from the CERN Optics team), Tobias Persson (from the MAD-X team) along with Tessa, to propose initial optics error estimates that also accounted for horizontal-vertical coupling in the machine. I then decided on using three parameter sets, firstly with no errors in order to get the bare lattice structure of a perfect machine, then with the FCC-ee tolerances, and finally with the HL-LHC tolerances as a comparison. From the aperture calculations, I plotted the available normalised aperture around the ring in python (with help from Andrey Abramov from the Collimation team to add the beamline above the plots) and identified the aperture bottlenecks. I also studied the aperture in momentum space and plotted the available momentum acceptance around the ring, again identifying the bottlenecks. With these results I then proposed first estimates of the collimator cuts.

During the project, when running MAD-X, we also received help from Leon Van Riesen-Haupt from the Optics team and Tobias with issues such as adding tapering (the change of individual magnet strengths to compensate the energy variation around the ring) and correctly matching the phase of Radio Frequency cavities accordingly. Later on in studies, a couple of bugs were found that were causing strange results for the on-momentum aperture calculations. Tobias

kindly removed these from the programme and provided us with a modified version of MAD-X.

The python script used to plot the beam halos was written by J.B. Jeanneret and was provided to me by Roderik, which I then modified slightly for my work. Roderik also provided an alternative script for plotting halos in Mathematica.

Of course, there are many other researchers to acknowledge for their inputs and useful discussions for my work, who will be properly thanked in the Acknowledgements section.

Chapter 1

Introduction

The electron-positron Future Circular Collider (FCC-ee) is being designed by an international collaboration coordinated by CERN. This design study was endorsed by the European Strategy for Particle Physics in 2013 [1]. The FCC-ee is conceived to be a very high-precision instrument that will study the Z, W and Higgs bosons and top quark pairs with a sensitivity high enough to point to potential physics beyond the Standard Model [1]. Such capabilities stem from the fact that this collider is designed to achieve luminosities of up to $230 \times 10^{34} \mathrm{cm}^{-2}\,\mathrm{s}^{-1}$, the highest of any lepton collider to date [1].

The particle beams in the FCC-ee carry a large amount of energy. Figure 1.1 shows the total energy stored in each beam for different lepton colliders. For the FCC-ee, while the highest mode of operation has a beam energy of 182.5 GeV for the top quark pair measurements, the total stored beam energy is highest at the lowest mode of operation, 45.6 GeV, at the Z pole, with 20.7 MJ stored in each beam (See Appendix A). At such high total energies, even a very small beam loss can cause experimental background, quenches of superconducting elements, or even significant damage to accelerator components in the event of regular and irregular beam losses. Therefore a system of collimators, which are blocks of material that absorb stray beam particles, is required to localise these losses away from experiments and sensitive equipment [2].

The most powerful lepton collider at present, SuperKEKB [3], suffered from damage to the collimator jaws due to unexpected beam losses [4]. Figure 1.2 shows the damage done to a pair of collimator jaws due to abnormal beams operating at high currents of 500 mA or above [4]. In the context of the FCC-ee, the damage reported in the SuperKEKB is of concern, because

the maximum stored beam energy of 20.7 MJ in the FCC-ee is more than twice the order of magnitude of the maximum stored beam energy of 0.18 MJ in the SuperKEKB, denoted by the dark blue dot and orange cross respectively in Figure 1.1. This clearly motivates the need to study halo collimation in the FCC-ee, whereby halo particles (those situated at the very edges of the beam due to diffusion processes such as intra-beam scattering [5] or point-like processes such as beam-beam or beamstrahlung) are intercepted safely before being lost at sensitive machine elements.

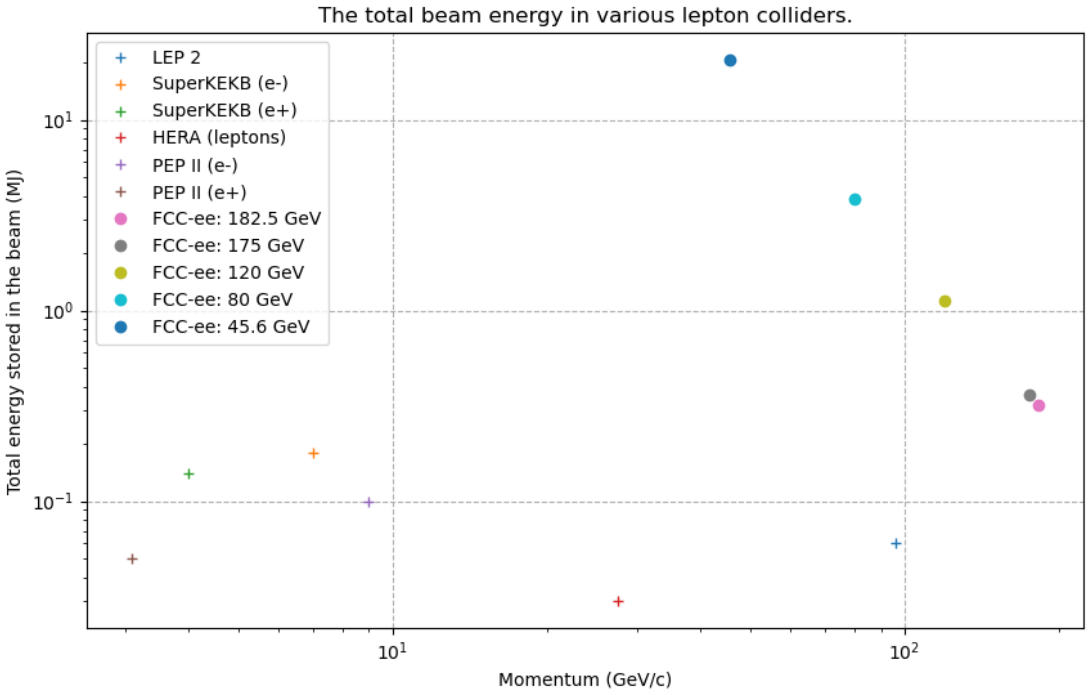

Figure 1.1: The total beam energy versus nominal particle momentum for various lepton colliders. The dots denote the different modes of operation in the FCC-ee, and the crosses denote the beam energies for the remaining lepton colliders.

In addition to cleaning the beam halos, collimation systems play several other roles in particle colliders [2]: Firstly, being the closest elements to the beam, the collimation system provides "passive machine protection" [2, p. 3] as it acts as the first stage of protection in the events of regular and irregular beam losses, so the collimators need to be able to survive operational failures. The collimation system must also be able to clean collision products in colliders, as well as minimise background noise in detectors caused by the beam halo or synchrotron radiation photons (in the case of lepton colliders). Likewise, equipment needs to be protected locally against radiation effects (such as synchrotron radiation in the arc magnets and beamstrahlung at the experiments) in order to maximise their lifetime. Additonally, the collimation system

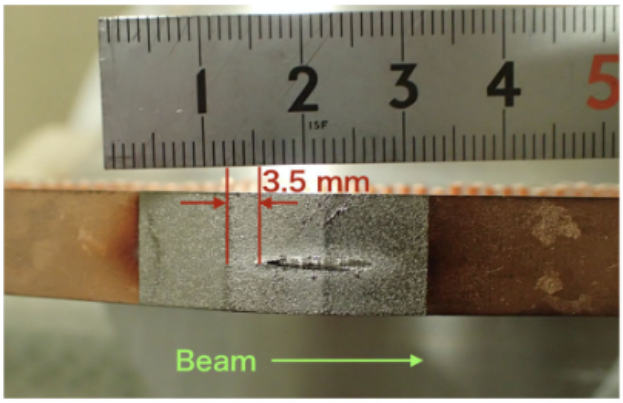

(a)

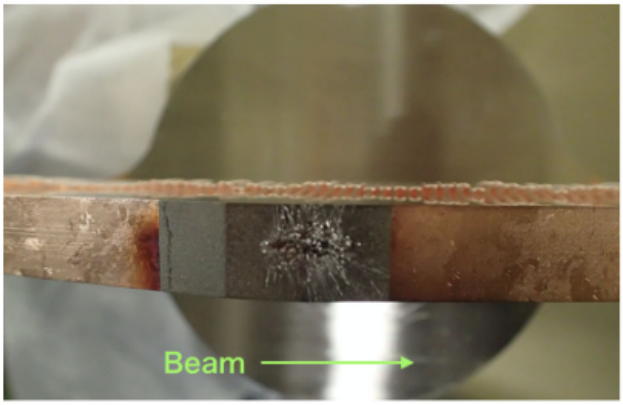

(b)

Figure 1.2: Pictures of the damage done to a pair of collimator jaws in the SuperKEKB due to high-current abnormal beams operating at 500 mA or above [4, Figure 16].

should localise beam losses to specific areas, so that the radiation dose is concentrated to one area as opposed to being spread across several points around the ring, allowing for safe access to the largest possible proportion of the ring for maintenance [2].

In the FCC-ee, the main roles of collimation will be to minimise and control the background noise in detectors, to locally protect the machine from synchrotron radiation photons and beamstrahlung photons, and, to clean the beam halo and protect the machine from regular and irregular beam losses, the latter role being the driving requirement as the stored beam energy can reach 20.7 MJ. While most of the magnets in the FCC-ee are normal-conducting, there are still some superconducting elements such as the Radio Frequency (RF) cavities, final-focus doublets at the interaction points, and one of the detector solenoids [1], which must be protected from impacting losses by the collimation system in order to avoid quenching.

In comparison, collimation in other lepton colliders was mostly used to minimise background noise in detectors and protect the machine from synchrotron radiation. For example in LEP2, collimation was used to suppress the background synchrotron radiation at the experiments and to protect the accelerator components from the radiation power which could go up to 10 kW [6]; in contrast, the total synchrotron radiation power per beam is 50 MW in the FCC-ee [1]. Similarly, in PEP-II, movable collimators were used to intercept scattered particles from bremstrahlung and beam-gas collisions to minimise the background in the BaBar detector and to protect it from the damage caused by radiation [7]. In the SuperKEKB, collimators were used to reduce background specifically caused by the Touschek effect and beam-gas scattering in the interaction regions [8]. For the FCC-ee, the first studies of the collimation required for background control in detectors have been performed and 20 collimators have been inserted into the ring layout closely upstream of the experiments [1].

This thesis describes the first studies of halo collimation needs in the FCC-ee. The focus is to study the machine aperture, to develop an aperture model of the whole ring, and to study the available normalised aperture for on-momentum and off-momentum particles to help identify any potential performance bottlenecks. The aim is then to use these results to propose an initial estimate of the required collimator cuts (the placement of the collimator jaw openings) in order for the collimators to be the limiting normalised apertures in the ring.

Chapter 2

Theoretical Background

2.1 Basic Linear Beam Dynamics

2.1.1 Transverse Dynamics

In a circular particle accelerator, the beam is bent along the circular path by dipole magnets and is focussed using quadrupole magnets. Using a linear approximation, the uncoupled equations of motion for a particle are given by [5]:

$$x''(s) + K(s) \cdot x(s) = \frac{1}{\rho(s)} \frac{\Delta p}{p_0}, \tag{2.1}$$

$$y''(s) - k(s) \cdot y(s) = 0, \tag{2.2}$$

where x and y are the horizontal and vertical deviations of the particle from the ideal orbit, s is the longitudinal coordinate denoting the position around the ring which has replaced the time coordinate ($s = ct$, where c is the speed of light), ρ is the bending radius of the dipole magnet, p_0 is the nominal momentum and Δp is momentum offset. The focusing coefficient, $K(s)$, is given by $K(s) = \frac{1}{\rho^2(s)} + k(s)$, where $k(s)$ is the focusing strength, give by $k(s) = \frac{eg}{p_0}$, where g is the local gradient of the magnetic field and e is the electric charge [5]. The focusing coefficient changes its form depending on the machine element; for example, in drift spaces,

$K(s) = 0$ as there is no magnetic field and the bending radius can be taken to be infinite, in dipoles, $K(s) = \frac{1}{\rho^2}$ as the magnetic field is uniform, and in quadrupoles $K(s) = k(s)$, again, due to an infinite bending radius [9]. These equations of motion assume that the beam is bent purely in the horizontal plane.

The full analytic solution to equations 2.1 and 2.2 is given by [5]:

$$z(s) = A_z\sqrt{\beta_z(s)}\cos\left(\phi_z(s) - \phi_{z_0}\right) + D_z(s)\delta, \tag{2.3}$$

where z has been used to denote x or y, $\delta = \frac{\Delta p}{p_0}$, and A_z and ϕ_{z_0} are constants of motion. The sinusoidal term in equation 2.3 is the general solution to the homogeneous version of the equation of motion 2.1, for the case of an on-momentum particle, $\Delta p = 0$. This term represents the betatron oscillations of the particle as a function of the phase advance, the amplitude of which is modulated by the $\beta_z(s)$ function, which is determined by the accelerator optics. The second term in equation 2.3 is the particular solution to the inhomogeneous equation of motion [9], 2.1, representing the amplitude contribution due to the particle's energy deviations (off-momentum or dispersive effects), where $D_z(s)$ is the dispersion function, which is a property of the machine and describes a new closed orbit with respect to the nominal orbit for particles with momentum deviation [5].

The phase advance, $\phi_z(s)$, is given by

$$\phi_z(s) = \int_{s_0}^{s} \frac{1}{\beta_z(s')}\, ds'. \tag{2.4}$$

The tune of an accelerator, Q_z, is the number of betatron oscillations performed per turn of the particle around the ring and is defined as

$$Q_z = \frac{1}{2\pi}\int_0^C \frac{1}{\beta_z(s')}\, ds' = \frac{\phi_z(s)}{2\pi}, \tag{2.5}$$

where C is the circumference of the accelerator [5]. The tune of an accelerator must be a carefully chosen irrational number, so as to avoid any coherent addition of kicks caused by any imperfections or small distortions in the magnets, which could otherwise result in large

betatron oscillation amplitudes [5].

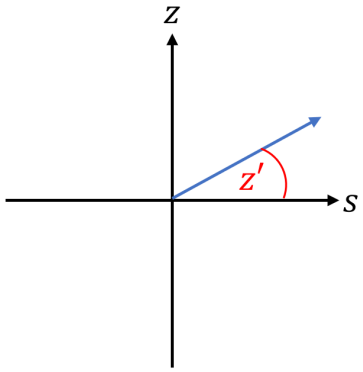

Figure 2.1: The blue arrow represents part of a particle's trajectory in one of the transverse planes, x or y, denoted here by z, with respect to the longitudinal coordinate, s. The derivative of z with respect to s is given by z', which for small values is represented by the angle in red, and is associated with the particle's momentum.

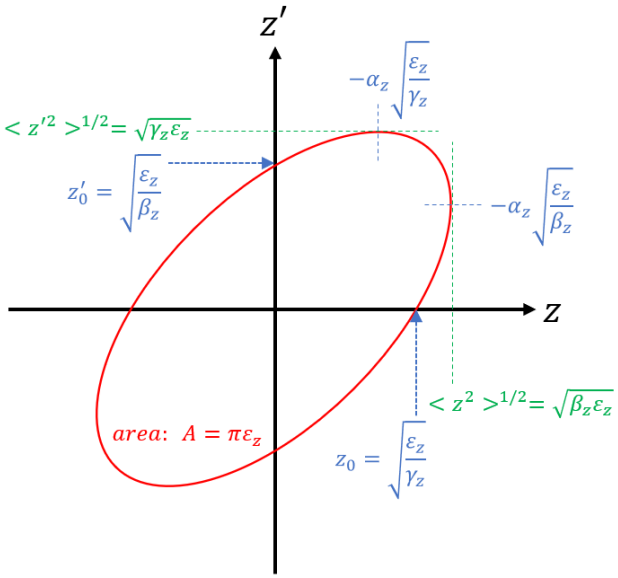

Figure 2.2: The ellipse in red formed by particles in horizontal or vertical phase space, denoted by z and z', defined by the emittance, ε_z, and Twiss paramters, α_z, β_z and γ_z. The area of the ellipse is given by $\pi\varepsilon_z$. (Reproduced from [5]).

The derivative of z with respect to s, $z'(s) = \frac{dz(s)}{ds}$, is given by the slope of a particle's trajectory [5], as shown in Figure 2.1. This, along with the nominal momentum gives the transverse momentum, $p_z \approx p_0 \sin z' \approx p_0 z'$ (for small z') [5]. The particle momenta are used to study the beam dynamics, but in the case of constant beam energy, the (small) angle of the particle trajectory z' is referred to rather than the tranverse momentum p_z [5].

Turn after turn, a given beam particle tends to map out an ellipse in phase space $z - z'$, defined by the geometric single-particle emittance [5], ε_z, given by

$$\varepsilon_z = \gamma_z z^2 + 2\alpha_z z z' + \beta_z z'^2, \tag{2.6}$$

where

$$\alpha_z = -\frac{1}{2}\beta'_z, \tag{2.7}$$

where $\beta'_z = \frac{d\beta_z(s)}{ds}$, and

$$\gamma_z = \frac{1+\alpha_z^2}{\beta_z}. \tag{2.8}$$

Together, α_z, β_z and γ_z are known as the *Twiss parameters* and are determined by the machine optics. Figure 2.2 shows a diagram of the phase space ellipse labelled with some of its key parameters. The area of the phase space ellipse is given by

$$\int_{ellipse} dz dz' = \pi\varepsilon_z, \tag{2.9}$$

and, by Liouville's theorem, it stays constant if there is no acceleration of the beam [5]. One can also define an emittance for the whole beam, which is a statistical property depending on all its single-particle emittances. It is possible to calculate this "root mean square emittance", $\varepsilon_{rms,z}$, as

$$\varepsilon_{rms,z} = \sqrt{< z^2 >< z'^2 > - < zz' >^2}. \tag{2.10}$$

The transverse beam size (beam half-width) at one standard deviation, assuming a Gaussian profile due to the betatron oscillations, σ_z, is then given by

$$\sigma_z(s) = \sqrt{\beta_z(s)\varepsilon_{rms,z}}, \tag{2.11}$$

and the divergence, also called the angular spread, is given by [5]

$$\sigma_z' = \sqrt{\gamma_z \varepsilon_{rms,z}}. \tag{2.12}$$

The transverse beam dynamics described thus far has treated the horizontal and vertical motions as being independent of each other, which would be the case for an ideal accelerator. In reality, the motions in the two transverse planes are coupled, primarily due to skew quadrupole fields and solenoidal fields [10]. The behaviour of the betatron oscillations in the horizontal and vertical planes is analogous to that of coupled pendula, where the oscillations in one plane transfer energy to the other plane with a frequency that is the difference between their tunes [10]. This means that the horizontal emittance can contribute to the vertical emittance, thereby increasing the vertical beam size and reducing the available vertical aperture [10]. The coupled equations of motions are

$$x''(s) + K(s) \cdot x(s) = \frac{1}{\rho(s)} \frac{\Delta p}{p_0} + \underline{k}(s) \cdot y(s), \tag{2.13}$$

$$y''(s) - k(s) \cdot y(s) = \underline{k}(s) \cdot x(s), \tag{2.14}$$

where $\underline{k}$ is the skew gradient of the quadrupole field [5].

2.1.2 Longitudinal Dynamics

The particles in synchrotrons are accelerated by RF cavities [11], where the time-dependent RF voltage, V_{RF}, varies sinusoidally with an angular frequency of ω_{RF}, in order to keep the beam bunched longitudinally. In lepton colliders, the RF cavities also serve the role of compensating the energy loss from synchrotron radiation [11]. The energy gain of the particle ($\Delta E = eV_{RF}$, where e is the electric charge) depends on its arrival time at the cavity, therefore the RF frequency must be synchronised with the revolution frequency of the particle. In other words, the RF frequency must be an integer multiple of the revolution frequency [11]:

$$\omega_{RF} = h \cdot \omega_{rev}, \tag{2.15}$$

where the harmonic number, h, is an integer. An RF bucket is a stable location in longitudinal phase space where the particles can be accelerated and kept synchronous [12], shown in Figure 2.3. It turns out that the number of RF buckets that can fit around the ring is equal to h, which are positioned equidistantly around the circumference of the accelerator [12].

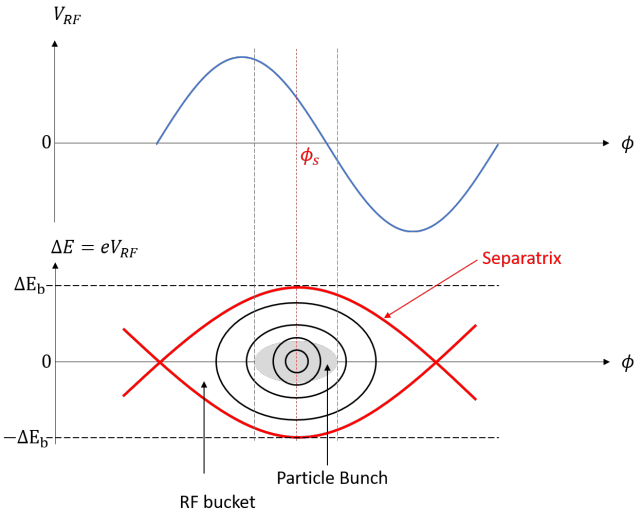

Figure 2.3: Example of an RF bucket marked with trajectories (black circles) of accelerated particles in longitudinal phase space (energy gain ΔE versus phase ϕ). The centre of the RF bucket is located at the synchronous phase, ϕ_s. The separatrix is the boundary beyond which particle motion becomes longitudinally unstable [12]. ΔE_b marks half the bucket height. The RF bucket has been pictured against the corresponding RF voltage.

The energy acceptance, $\frac{\Delta E}{E_0} \approx \delta$, is the maximum energy deviation a particle can have for it to be in the stable region delimited by the separatrix [12] (see Figure 2.3). Therefore, the maximum energy acceptance is denoted by ΔE_b (the bucket height), and is given by the area contained within the separatrix (for particles with positive or negative energy deviations).

2.2 Beam Losses and Aperture

The geometric aperture refers to the physical openings of elements in an accelerator, which limits the maximum transverse beam size. The amplitude of the particles must be well within the geometric aperture all around the ring to avoid beam losses [5], which occur when the tail of the beam touches the aperture.

The beam lifetime refers to how long a particle beam can typically circulate in the accelerator before it gets lost. The total beam intensity is usually assumed to have an exponential decay,

and the lifetime is defined as the time after which only a fraction $1/e$ of the initial intensity remains. There are several mechanisms which can drive particles onto the geometric aperture, causing them to be lost: Beam-gas scattering occurs when the beam particles are scattered by the residual gas particles in the vacuum chamber [10]. There is also the effect of thermal photon scattering, which is an example of inverse Compton scattering whereby the electrons or positrons from the beam interact with photons from black body radiation in the beam pipe and transfer energy to the photons [10]. Within the beam itself, particles performing longitudinal synchrotron oscillations [5] can undergo elastic collisions. Sometimes their large transverse momenta can transfer into their longitudinal momenta, resulting in the loss of both particles when they perform head-on collisions in such a scenario [5]. This is called the Touschek effect and becomes significant when there are dense particle bunches at high energies. Radiative Bhabha scattering is an electron-positron scattering process, for which there are two leading-order Feynman diagrams, one of annihilation and the other, a scattering process, that can explain this interaction, which is one of the major effects that dominates beam lifetime in the FCC-ee [1].

There are also beam loss effects which result from the magnetic field of the opposing beam. One such effect is beamstrahlung, which is synchrotron radiation that gets emitted during the collision in the presence of the electromagnetic field of the other beam [13]. The high-energy photons from beamstrahlung greatly affect the energy spread of the beam, and the particle which emitted the photon is lost if its resulting lower energy falls outside the energy acceptance [13]. Beamstrahlung is the other main effect which dominates beam lifetime in the FCC-ee [1]. Another effect is the beam-beam effect, where the trajectories of the particles in one beam can get perturbed by the strong non-linear field of the opposing beam [5].

The dynamic aperture (DA) is the amplitude in real space within which all particles stay confined (are not lost) over several revolutions in the accelerator. In an ideal machine, the DA would be greater than the geometric aperture [5]. In reality, the accelerator lattice contains elements, such as sextupole magnets, which introduce non-linearities in magnetic field components. This affects the particle dynamics and hence such elements contribute to the DA of the machine [5] by reducing it. Beyond the DA, particles show a chaotic behaviour and are eventually lost. If the DA is smaller than the geometric aperture, then the particles at amplitudes larger than the DA might be pushed to larger amplitudes by the non-linear forces and hit

the vacuum chamber. The particles that fall outside the DA contribute to the beam halo (see Figure 2.4), for which halo collimation is then needed to protect the machine elements from beam losses.

In this piece of work, however, it is actually the available normalised aperture that will be studied; this is essentially the available geometric aperture divided by the local betatronic beam size, so the the aperture will be obtained in units of beam size σ_z in Eq. (2.11). The placement of the collimator jaws will essentially be cutting into the beam. Typically, several beam sigmas of clear space are needed around the beam in order to prevent the tails from touching the geometric aperture. However, in the FCC-ee, significantly more beam sigmas are required (many tens of sigmas - yet to be verified) in the vertical plane to avoid losing particles that are kicked by beamstrahlung or the beam-beam effect.

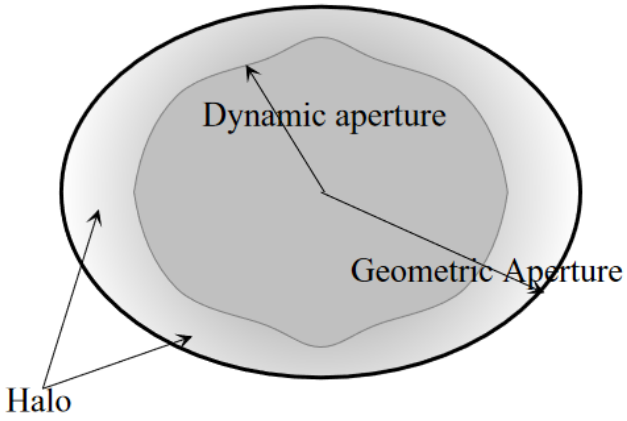

Figure 2.4: An example of the geometric and dynamic apertures in a circular accelerator, where the latter is smaller than the former. The beam halo is formed by the particles outside the dynamic aperture, which are subsequently lost through beam loss mechanisms, highlighting the need for halo collimators to protect the aperture. Diagram from [14, Figure 1.3].

Chapter 3

Theory of the Aperture Model

The work in this study was carried out mainly using the computer programme called MAD-X, which was developed at CERN as a tool to simulate accelerator optics to study the design of an accelerator [15]. This chapter describes the use of MAD-X to calculate the available aperture, as well as simple 1D standalone calculations used for comparison and to compute the momentum acceptance.

In order to design an accelerator in MAD-X, each machine element must be defined with its corresponding parameters (such as magnetic field strength, magnet length etc.). The definitions of the elements are typically found in a sequence file, ".seq", and the strengths in a separate file, ".str", although the two could also be combined. These files are then used as an input in the ".madx" script, where other important parameters such as beam energy, type of particle, number of bunches per beam etc. are defined. Such files for the FCC-ee were obtained from the CERN GitLab repository [16]. These files were then used as the basis for performing aperture calculations, as will be explained in the subsequent sections.

3.1 The Aperture Command in MAD-X

The aperture command in MAD-X can be used to calculate the available normalised aperture around the ring. Essentially, the calculation uses the vector sum of several different errors, detailed in the subsequent sections, to calculate a new worst-case central orbit that has been displaced from its ideal position (O' in Figure 3.1), which now forms the new centre of the

beam halo [17, 18]. From here, by scanning across the azimuthal angle of the closed orbit, the largest possible secondary halo is calculated, such that it exactly reaches the geometrical aperture [17, 18], shown in red in Figure 3.1. From this value, and the assumed shapes of the primary and secondary halos, the maximum opening of the primary collimator that still protects the aperture is derived, shown in green, and is then normalised to the local betatronic beam size. This value is called n_1 [17, 18].

In this study, the aperture command was instead used to find largest possible halo extension that still fits in between the new central orbit and physical aperture, which was then used to calculate the beam-stay-clear in the same manner it was used for the HL-LHC [17, 18].

The aperture command takes several different input parameters to define the errors it uses to find the available aperture. It reads in mechanical tolerances, usually from an input file, and takes other input parameters about the beam as arguments in the aperture command itself [15]. These inputs are explained in the following sections.

Additionally, the aperture command uses the optical β_z functions and dispersion D_z functions as inputs, that must be calculated in a previous TWISS command in MAD-X [15]. The TWISS command is used to calculate the linear optical functions around the lattice, which include the *Twiss* β_z and α_z functions, the phase advance ϕ_z, the dispersion functions D_z and a few others, detailed in [15]. It is also possible to calculate the optical functions for off-momentum particles using the DELTAP argument of the TWISS command, where DELTAP is defined as $\frac{\Delta p}{p_0}$.

3.1.1 Aperture Tolerance Definition

One of the errors that leads to the displacement of the central orbit is the misalignment and imperfections in the manufacturing of element apertures around the ring. These are referred to as mechanical tolerances, and they are defined for each element in MAD-X in the transverse plane using a racetrack shape. The associated parameters of this definition are then used as arguments in the aperture tolerance command, APER_TOL = {r, g, s}, defined in Figure 3.2.

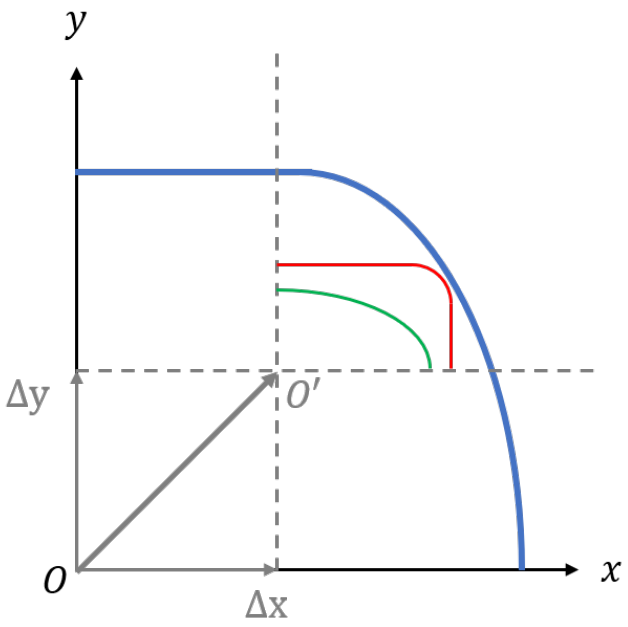

Figure 3.1: An example of the upper right quadrant of a beam pipe of arbitrary shape and size (given in blue), i.e. the geometric aperture. The displacements Δx and Δy give the new origin, O', of the beam centre, which is due to a combination of mechanical and beam tolerances. In the n_1 calculation, the sizes of the primary halo (green) and secondary halo (red) are calculated such that the secondary halo reaches the geometric aperture [17]. (Adapted from [18]).

.

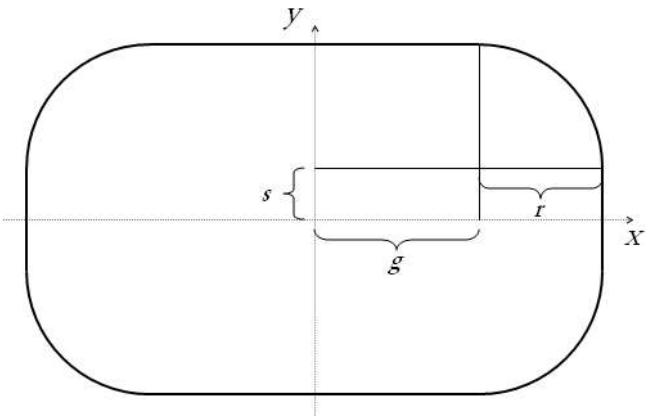

Figure 3.2: The misalignment of elements in MAD-X are defined in the transverse plane using a racetrack shape. The parameters r, g and s are used in the APER_TOL = {r, g, s} command to define the aperture tolerance for each element [15, Figure 23.1].

Tolerance Parameter	Meaning	Default Value
COR [m]	Maximum radial closed orbit.	0.004
BBEAT	Increase of the beam size.	1.1
DQF [m]	Peak linear dispersion.	2.086
DPARX	Fractional horizontal parasitic dispersion.	0.273
DPARY	Fractional vertical parasitic dispersion.	0.273
DP	Bucket edge at the current beam energy.	0.0015
BETAQFX [m]	Optical β_x function in a focusing arc quadrupole.	170.25

Table 3.1: Summary of the additional beam tolerances taken as input parameters into the aperture command in MAD-X.

3.1.2 Beam Tolerances

The other errors used by the aperture command come from the beam tolerances, for which the additional input parameters have been summarised in Table 3.1. The maximum radial closed orbit, COR, directly affects the displacement of the beam centre as this refers to the deviation of the closed orbit from the ideal orbit. The displacement of the central orbit is also affected by a contribution from the product of the momentum offset and the total dispersion. Here, the total dispersion refers to the ideal periodic dispersion function in the plane that is being considered, increased by a factor k_β (BBEAT in Table 3.1) representing a potentially larger beam size due to an imperfect optics correction, plus a contribution from a quantity called the spurious dispersion. The latter refers to the parasitic contribution from an imperfect optics correction in the arc [18]. The equation for the total dispersion, $\tilde{D}_z(s)$, is given by [17]:

$$\tilde{D}_z(s) = k_\beta \left(D_z(s) + D_{qf} D_{para} \sqrt{\frac{\beta_z(s)}{\beta_{qf}}} \right), \tag{3.1}$$

where D_{qf} is the maximum dispersion in a focusing arc quadrupole (DQF), D_{para} is the fractional parasitic dispersion (DPARX or DPARY), β_{qf} is the peak optical β_x function in a focusing quadrupole (BETAQFX), and $D_z(s)$ and $\beta_z(s)$ are the optical dispersion and beta functions respectively calculated from the required previous TWISS command. As before, z denotes x or y.

The factor k_β often accounts for several effects that lead to a change (usually increase) in the beam size. The most common effect is the beating of the beta function, beta-beating, which is caused by effects from non-linear elements in the lattice, such as sextupole magnets [5]. The

beam size growth is also caused by emittance increases around the ring and coupling. In the aperture calculation, when the halo is normalised to the local beam size, it is actually the local beam size scaled by this k_β factor that is used [17].

3.2 Momentum Acceptance and 1D Transverse Aperture Calculation

The maximum momentum acceptance, $\delta_{\max}$, was calculated around the ring for particles with a given betatron oscillation amplitude n and for each of the beam energies as:

$$\delta_{\max} = \frac{A_x - n\sigma}{D_x}, \tag{3.2}$$

where A_x is the available geometric aperture in the horizontal plane, D_x is the horizontal dispersion, and σ is the betatronic beam size given by $\sqrt{\beta_x \varepsilon_x}$, for which the design emittances were used. The momentum acceptance was calculated using $n = 0, 7$ and 8, because a minimum of seven or eight sigma is an estimated requirement to guarantee an acceptable beam lifetime [19], and it will be interesting to see the comparison with zero sigma.

As a comparison to the MAD-X results, the beam-stay-clear values, n_z, were also calculated using a one-dimensional calculation given by:

$$n_z = \frac{A_z - z_{co} - z_{tol} - \Delta z_D}{k_\beta \sqrt{\beta_z \varepsilon_z}}, \tag{3.3}$$

where A_z is again the available geometric aperture, z_{co} is the maximum radial closed orbit, z_{tol} is the contribution from the mechanical tolerances, and Δz_D is the offset from the total dispersion, with z denoting x or y. For the mechanical tolerances, x_{tol} is given by $g + r$ from the APER_TOL parameters, and similarly y_{tol} is given by $s + r$ in this 1D setup. The dispersion contribution Δz_D is calculated by:

$$\Delta z_D = k_\beta \left(|\delta_{dp} D_z| + \left(|\delta_{twiss} + \delta_{dp}| D_{qf} D_{para} \sqrt{\frac{\beta_z}{\beta_{qf}}} \right) \right), \tag{3.4}$$

where δ_{dp} refers to DP in Table 3.1 and $\delta_{twiss} = \frac{\Delta p}{p_0}$ which is given by the DELTAP argument in the TWISS command.

One of the differences between the MAD-X aperture calculation and the one dimensional calculation is that for elements longer than 1 m, MAD-X slices the element at specified intervals (the default interval value being 1 m) and calculates the available normalised aperture at each slice. Whereas with the 1D calculation, the optical functions calculated by the TWISS commmand are used, which have been evaluated only at the end of each element, meaning there is no slicing involved, resulting in a less detailed picture of the aperture around the ring.

Chapter 4

Setting Up the Aperture Model

4.1 FCC-ee MAD-X Aperture Model

The aperture model is essentially a ".madx" file in which the physical apertures of each element in the accelerator are defined by specifying their shape and size [15]. It is required by MAD-X in order to perform aperture calculations.

Previously for the FCC-ee, the available aperture model only contained aperture definitions for the two experimental insertions (IRA and IRG), and not for the rest of the ring. The final optics and apertures for the FCC-ee have not yet been decided, therefore as an initial estimate, the aperture model was completed by approximating the remainder of the ring as having a homogeneous aperture that is a circular vacuum chamber (beam pipe) with a radius of 35 mm [1], shown in Figure 4.1. The present ring design foresees this design for a vast majority of the elements, although with small horizontal rectangular slits (antechambers) on each side of the beam pipe to extract photons from synchrotron radiation onto absorbers [1], as shown in Figure 4.2. No element should have an aperture that is smaller than this, hence this is a conservative assumption. In future work, this aperture model can be adjusted to incorporate the antechambers.

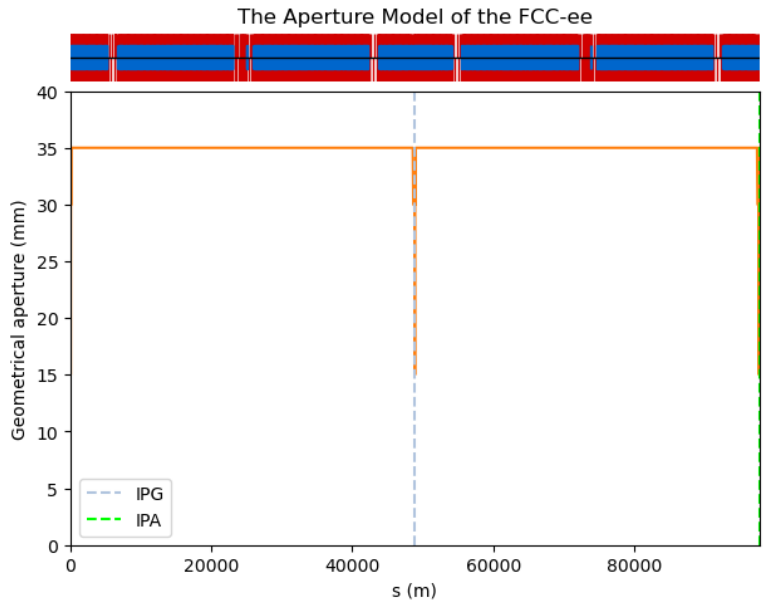

Figure 4.1: The geometrical aperture in the FCC-ee lattice, with a homogeneous aperture in the arc sections, that is a circular vacuum chamber with a radius of 35 mm [1]. The interaction regions, indicated by the positions of the interaction points, IPG and IPA, have smaller circular apertures. The longitudinal coordinates of the lattice, s, start from and finish in the middle of IPA [1]. Above the plot is a schematic diagram of the lattice layout: the central black line indicates drift space, the blue indicates dipoles, the red elements above and below the drift space represent focusing and defocusing quadrupoles respectively.

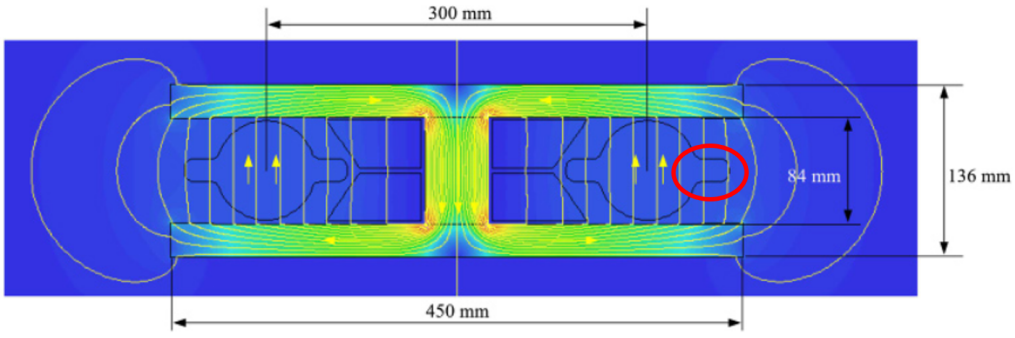

Figure 4.2: The cross-section of the main dipole magnet in the FCC-ee, along with its magnetic field lines. An outline of the two vacuum chambers and their antechambers, one of which has been circled in red, is also presented [1, Figure 3.1].

4.2 FCC-ee Mechanical Tolerances

The FCC-ee mechanical tolerances were calculated from the RMS misalignment tolerances given in [20], which were assumed for studies of global optics corrections. The relevant parameters have been summarised in Table 4.1 and defined in Figure 4.3. The mechanical tolerances calculated from these resulting RMS tolerances remain constant for all the elements in the subsequent aperture calculations in MAD-X.

Type	**ΔX** (μm)	**ΔY** (μm)	ΔΘ (μrad)	ΔΦ (μrad)
Arc quadrupoles	50	50	100	100
Arc Sextupoles	50	50	100	100
Dipoles	1000	1000	0	0
IR quadrupoles	75	75	75	75
IR sextupoles	75	75	75	75

Table 4.1: The RMS misalignment of the elements in the FCC-ee, where ΔX and ΔY indicate the horizontal and vertical misalignment of the element from the centre of the girder, and, ΔΘ and ΔΦ indicate the horizontal and vertical tilts of the elements about the girder respectively, defined in Figure 4.3 [20]. The tilts of the dipoles are not yet known.

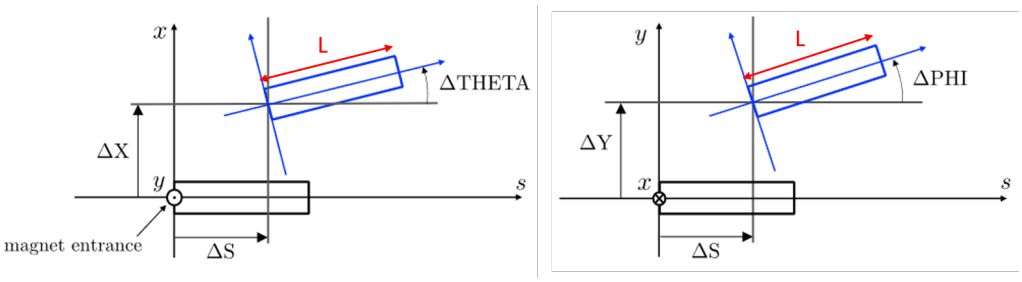

Figure 4.3: The x, y and s axes correspond to that of the girder which supports the elements. The parameters ΔX and ΔY correspond to the horizontal and vertical displacements of the element from the centre of the girder, and, ΔΘ and ΔΦ correspond to the horizontal and vertical tilts of the element respectively about the s axis. The longitudinal misalignment is indicated by ΔS. The lengths of the magnets are indicated in red by L. (Adapted from [20]).

For the FCC-ee, the g and s parameters for the mechanical tolerances were calculated using the following equations:

$$g = \Delta X + L \sin \Delta\Theta, \tag{4.1}$$

$$s = \Delta Y + L \sin \Delta\Phi. \tag{4.2}$$

Type	Element	Length (m)	{r, g, s} (m)
Arc quadrupoles	All	2.90	{0, 3.4e-4, 3.4e-4}
Arc sextupoles	All	1.40	{0, 1.9e-4, 1.9e-4}
Dipoles	All	23.00	{0, 1e-3, 1e-3}
IR quadrupoles	QC4L, QC3L, QC3, QC4, QC5, QC6	3.50	{0, 3.375e-4, 3.375e-4}
	QC2L2, QC2L1, QC2R1, QC2R2	1.25	{0, 1.687e-4, 1.687e-4}
	Remaining	1.00	{0, 1.5e-4, 1.5e-4}
IR sextupoles	All	0.15	{0, 8.625e-5, 8.625e-5}

Table 4.2: Summary of the mechanical tolerances used for the elements in the FCC-ee. The average length of each element type has been used, except in the case of the quadrupoles in the interaction region (IR), where three different lengths have been used to improve accuracy.

Table 4.2 summarises the resulting mechanical tolerances calculated for each type of element, which were used in the subsequent aperture calculations. The average length of each type of element was used, except for the IR quadrupoles as their lengths differed a lot, so three different lengths were used for accuracy.

4.3 FCC-ee Beam Tolerances

The normalised aperture was calculated for three different parameter sets; firstly, with no beam tolerances or mechanical tolerances, in order to get the bare lattice structure, secondly, using the best estimates of the FCC-ee tolerances (detailed below), and finally with the HL-LHC tolerances [21] for comparison. The beam tolerances for these three scenarios are summarised in Table 4.4.

For the FCC-ee, the maximum radial closed orbit (COR) was obtained from the global optics corrections performed by T. Charles [20] and was found to be around 250 μm for on-momentum particles and 3.7 mm for off-momentum particles with a momentum deviation of 1 %. The parasitic dispersion for the FCC-ee has not yet been calculated, so the parasitic dispersion values for the HL-LHC, 0.1, were used instead.

As for the beam size increase, the beam growth is not necessarily dominated by the beta-beating and the dispersion function, as it is typically assumed for hadron accelerators, but it is also due to imperfect equilibrium emittances and coupling. The emittance tuning studies for on-momentum particles by T. Charles [22] takes into account of all these effects. The net combined result of these effects can be accounted for in the BBEAT parameter, as opposed to

setting larger emittances, for example. However, this still does not account for the possibility of a tilted beam envelope, the effect from which is likely to be small, but should still be investigated in future studies. This would, however, require a new version of MAD-X that can incorporate the tilting of the beam envelope in the aperture calculations. From the emittance tuning studies [22], it was found for on-momentum studies that a maximum beam size increase of $\frac{\sigma_x}{\sigma_{x_0}} = 1.1$ covers practically all simulated bunches in the horizontal plane, where σ_{x_0} is the horizontal reference beam size. The horizontal beam size growth is attributed to beta-beating and emittance increases, which are covered by BBEAT = 1.1.

In the vertical plane, there is a very large spread between the results from different random bunches in [22]. The large growth simulated in the vertical plane is predominantly due to coupling and emittance increases, as well as some beta-beating, all of which are accounted for with BBEAT = 10, which is a pessimistic estimate. From the emittance tuning studies where the reference beam sizes were calculated using the design emittance values [22, slide 12], which is the most suitable method for the collimation studies, the beam size increase reaches a factor of 4. Therefore, to ensure that all effects are accounted for, another suitable value to use for the vertical on-momentum aperture studies would be BBEAT = 5. Both these values are therefore used in the subsequent aperture calculations.

As the two planes have very different characteristics in terms of emittance and beam size beating, they were studied separately. In Chapter 5, it will be shown that the aperture bottleneck lies in one of the two planes, as opposed to a skew plane, allowing for the aperture to be studied separately in the horizontal and vertical planes.

As for the beam size increase for off-momentum particles, the studies done so far by T. Charles [20] are only preliminary, and only a few of the particle bunches converged. Nevertheless, from [20, slide 9], it can be seen that the beta-beating factor for particles with a 1 % momentum deviation is around 90 % in the horizontal plane, which translates to a beam size increase factor of around 1.4 that can be used as a first estimate for the BBEAT parameter. For the vertical plane, the beam size increase for off-momentum particles has not yet been studied. Therefore, a first estimate to use could be BBEAT = 10, as the off-momentum aperture will be worse than the on-momentum aperture, but local optics corrections are yet to be performed, which are expected to greatly improve the beam size increase overall for both planes. Hence, this first estimate seems like a reasonable value, but would have to be studied in more detail.

4.4 Emittance

To run the aperture command, the horizontal and vertical emittances must be defined in the BEAM command in MAD-X, in order to calculate the normalised aperture using the transverse beam size. For the horizontal aperture calculations, the horizontal and vertical design emittances [1] were used, shown in Table 4.3, and any potential imperfections on the emittances were accounted for in the BBEAT parameter. The horizontal design emittances are about a factor of 500 times larger than the vertical design emittances, so naturally, the aperture bottleneck will be found in the horizontal plane when using the design emittances. Therefore, in order to bias the results and probe the vertical plane, the horizontal emittances were set to be 100 times smaller than the vertical design emittances (listed in the last row of Table 4.3), in terms of order of magnitude, so that the vertical plane dominates, allowing for the vertical aperture bottlenecks to be calculated separately.

Beam Energy (GeV)	45.6	80	120	175	182.5
Horizontal Design Emittance (nm rad)	0.27	0.84	0.63	1.34	1.46
Vertical Design Emittance (pm rad)	1	1.7	1.3	2.7	2.9
Horizontal Emittance (pm rad) (used for the vertical aperture calculation)	0.0027	0.0084	0.0063	0.0134	0.0146

Table 4.3: Summary of the emittances used in the aperture calculations. The design emittances were used to calculate the horizontal normalised aperture. In order to get the vertical normalised aperture, the horizontal emittances were set to be 100 times smaller than the vertical design emittances.

4.5 Using Different Tolerances

The aperture was calculated for three scenarios; firstly with no tolerances, then with the FCC-ee beam and mechanical tolerances, and finally with the HL-LHC beam and mechanical tolerances as a comparison. The HL-LHC mechanical tolerances that were used are shown in Table 4.5.

The normalised aperture was also calculated for both on-momentum and off-momentum particles using the DELTAP attribute of the TWISS command in MAD-X. Evidently, this was set to zero for the on-momentum case, meanwhile for the off-momentum case, a momentum deviation of 1 % was used (i.e. DELTAP = 0.01). Table 4.6 presents the required momentum acceptance at each beam energy as specified in [1]. These specified momentum acceptances

Parameter	No Tolerance	FCC-ee Tolerances	HL-LHC Tolerances
COR [m]	0	0.00025 / 0.0037	0.002
HALO	{6,6,6,6}	{6,6,6,6}	{6,6,6,6}
BBEAT (horizontal plane)	1	1.1 / 1.4	1.1 / 1.4
BBEAT (vertical plane)	1	5 & 10 / 10	5 & 10 / 10
DP	0 / 0	0 / 0	0 / 0.0002
DPARX	0 / 0	0 / 0.1	0 / 0.1
DPARY	0 / 0	0 / 0.1	0 / 0.1
DQF [m]	0.25	0.25	0.25
BETAQFX [m]	93	93	93

Table 4.4: Summary of the beam tolerances used for each scenario; with no tolerances, using the FCC-ee tolerances, and using HL-LHC tolerances. Where there are more values than one present, the value(s) before the backslash corresponds to the on-momentum calculation and the value(s) after the backslash corresponds to the off-momentum calculation.

Type	{r, g, s} (m)
Dipoles	{0.001650, 0.001100, 0.000000}
Quadrupoles	{0.001140, 0.000900, 0.000000}

Table 4.5: The HL-LHC mechanical tolerances for all the dipoles and quadrupoles.

are needed to prevent the loss of too many particles during collisions; beamstrahlung plays a significant role in terms of beam losses in the FCC-ee, especially at the $t\bar{t}$ energies, which is why a wide momentum acceptance of -2.8% +2.4% is required [1]. Based on the momentum acceptances, and the fact that most random bunches with 2% momentum deviation did not converge to a stable solution in the studies from [20], DELTAP = 0.01 seemed like an appropriate parameter to use for the first off-momentum aperture studies. However, once the studies for off-momentum optics corrections are more refined, the off-momentum aperture studies must be redone, potentially for a larger value of DELTAP.

	Z	WW	ZH	$t\bar{t}$	
Beam Energy (GeV)	45.6	80	120	175	182.5
Required Momentum Acceptance (%)	±1.3	±1.3	±1.7	-2.8 +2.4	

Table 4.6: The required momentum acceptance at each beam energy as specified in [1].

To summarise, the normalised aperture was calculated in the horizontal and vertical planes using no tolerances, FCC-ee tolerances, and HL-LHC tolerances for on-momentum and off-momentum particles, across all the beam energies (listed in Table 4.6).

Chapter 5

Results

5.1 Beam-Stay-Clear Results

In the following sections, the beam-stay-clear results are presented for the on-momentum and off-momentum calculations in the horizontal and vertical planes. These results have been plotted for each beam energy, using the three tolerance sets. The points on the graphs indicate the normalised aperture limit at that particular position in the accelerator, in units of beam sigma. As mentioned previously, the first parameter set used to calculate the beam-stay-clear was with no beam or aperture tolerances, in order to obtain the bare aperture for a perfect machine. This is shown in blue in the figures which present the beam-stay-clear calculated using all three tolerance sets. As expected, adding the first estimates of the FCC-ee on-momentum tolerances produced lower normalised aperture limits, given in green in those figures. Lastly, as the HL-LHC tolerances were more pessimistic than those of the FCC-ee, the corresponding normalised aperture limits are the lowest, given in orange, for the on-momentum plots. For the off-momentum calculations, the maximum radial closed orbit (COR) for the FCC-ee was greater than that for the HL-LHC (see Table 4.4), hence the two tolerance sets start to have a similar effect, resulting in similar normalised aperture limits. Above each plot is also a diagram of the beam line with the central black line indicating drift space, the blue elements representing dipoles, and the red elements above and below the drift space representing focusing and defocusing quadrupoles respectively.

In this work, only the positron beam has been studied, but the results for the electron beam

will be symmetrical.

5.1.1 Position of the Aperture Bottleneck in the Transverse Plane

Firstly, it is shown that the aperture bottleneck always lies in one of the two planes, as opposed to a skew plane, which significantly simplifies the analysis, since the two planes can be treated independently. In the method described in Chapter 4 section 4.4, the horizontal emittances were artificially set to be 100 times smaller than the vertical emittances, using BBEAT = 5 or BBEAT = 10 alongside, in order to probe the vertical plane. Another way to account for the beam size beating in the vertical plane is to increase the vertical emittances instead: If we use the horizontal design emittances and BBEAT = 1.1, corresponding to the horizontal plane, this must be compensated in the vertical plane by multiplying the vertical emittances by a factor of $\left(\frac{k_{\beta_y}}{k_{\beta_x}}\right)^2$ (as $\varepsilon_z \propto \sigma^2$), where $k_{\beta_{x,y}}$ denotes the values of the BBEAT parameter in the horizontal and vertical planes, so $k_{\beta_x} = 1.1$ and $k_{\beta_y} = 5$ or 10 in this case. This should, in principle, allow the identification of the aperture bottleneck anywhere in the transverse plane, which is what can be seen in Figure 5.1c, that was produced using $k_{\beta_y} = 10$. The Figure shows the halo with size $n\sigma$, with n being the found normalized aperture that includes all beam tolerances, together with the mechanical aperture. In this case, the bottleneck is still purely in the vertical plane, and with same magnitude as for the vertical study. Figure 5.1d was produced in the exact same way as Figure 5.1c, using $k_{\beta_y} = 5$ instead, however, the global bottleneck lies in the horizontal plane at the location of the element with the horizontal aperture bottleneck, with the same normalised aperture limit, i.e. the same as Figure 5.1a that was produced using the design emittances. This could be investigated further to find at which value of k_{β_y} the aperture bottleneck crosses over the planes. Figure 5.1b shows the halo at the vertical aperture bottleneck calculated using the vertical design emittances and smaller horizontal emittances. In any case, the aperture bottleneck in is one of the two planes, allowing for the horizontal and vertical planes to be studied separately.

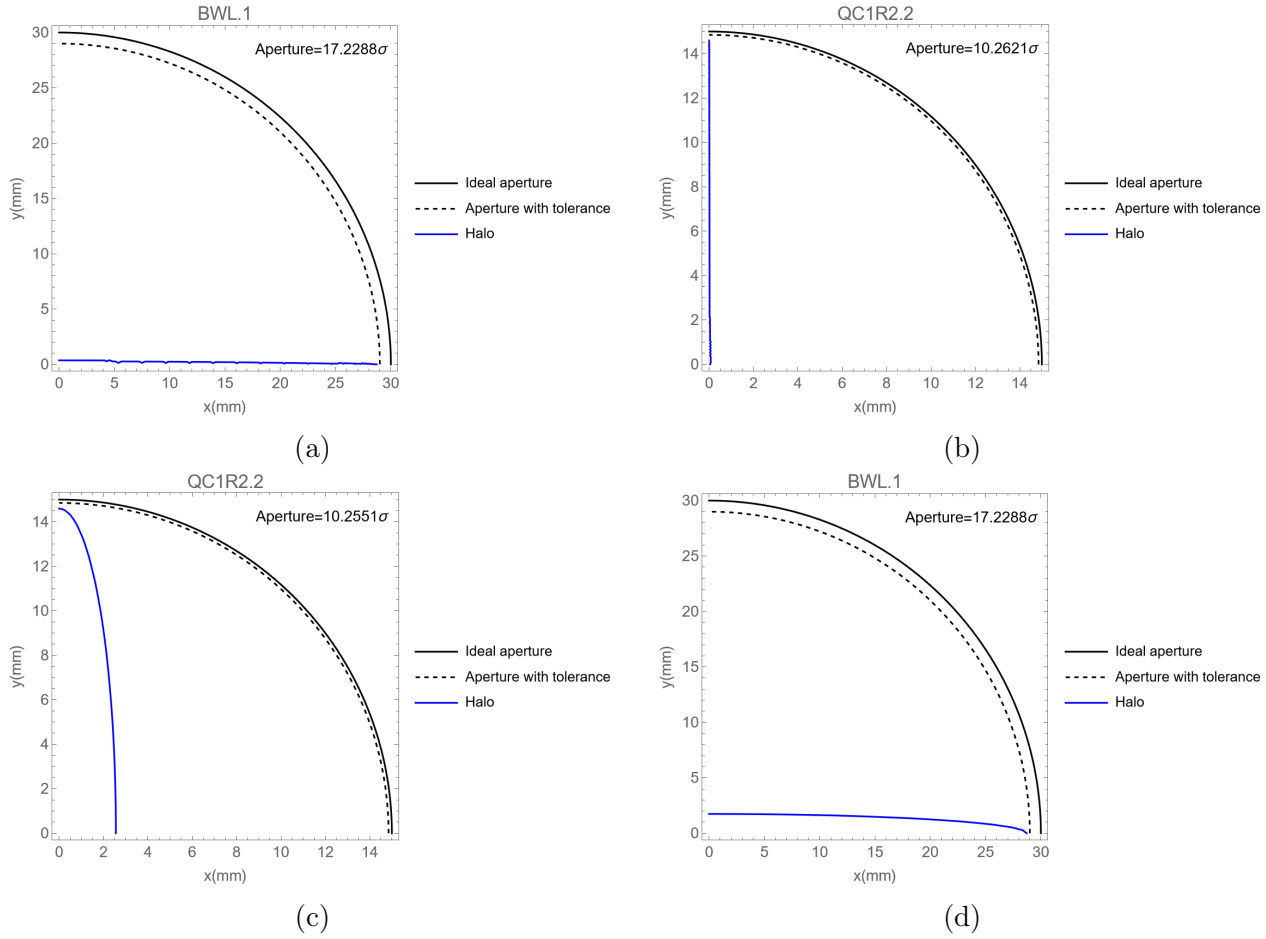

Figure 5.1: Plots of the beam halo in the transverse plane at the locations of the bottlenecks, calculated at the beam energy of 182.5 GeV for on momentum particles using BBEAT = 1.1. The halos were calculated using a) the design emittances, b) the vertical design emittance, but with the horizontal emittance set to be 100 times smaller, c) the horizontal design emittance, but with a vertical emittance increased by a factor of $\frac{k_{\beta y}^2}{k_{\beta x}^2} = \frac{10^2}{1.1^2}$, and d) the horizontal design emittance, but with a vertical emittance increased by a factor of $\frac{k_{\beta y}^2}{k_{\beta x}^2} = \frac{5^2}{1.1^2}$, where $k_{\beta_{x,y}}$ denotes the values of the BBEAT parameters used in the horizontal and vertical planes. In any case, the aperture bottleneck always lies in one of the two planes, as opposed to a skew plane.

5.1.2 On-momentum Particles

Horizontal Plane

Figure 5.2 presents the beam-stay-clear values around the ring calculated for on-momentum particles in the horizontal plane. It can be seen that the available normalised aperture is very similar at the different energies, which is also true for the other calculations. This might be the effect of the design emittances, listed in table 4.3, or it could be due to significant optics changes: Looking at the design emittances of the two extreme energies, 45.6 GeV and 182.5 Gev, and using the definition of the transverse beam size in equation 2.11, one would expect the apertures at 182.5 GeV to be lower than those at 45.6 GeV by a factor of $\frac{\sqrt{1.46}}{\sqrt{0.27}} \approx 2$, but in reality, this difference is a factor of ~ 1.5. Looking at the on-momentum optical β_x functions instead, presented in Figure 5.6 for each of the beam energies around the ring, the difference in aperture between the 45.6 GeV and 182.5 GeV at IPG should be a factor of $\frac{\sqrt{3700}}{\sqrt{1500}} \approx 1.6$, which is closer to what is observed and is the likely reason behind the similar aperture limits at each energy. The aperture bottlenecks are located near the interaction points at IPG and IPA. Figure 5.3 presents a closer view of the beam-stay-clear values at IPG. It should be noted that the interaction regions IRG and IRA are optically identical, hence the normalised aperture limits around IPA will also be identical to those around IPG presented in Figure 5.3. The bottlenecks are found in the elements BC1L, QC4L, and BWL, which are located just before each of the two IPs; this dipole-quadrupole-dipole trio can be seen in the beam line above each of the plots in Figure 5.3, located between $s \approx 48\,580\,\text{m}$ and $s \approx 48\,780\,\text{m}$, where the lowest aperture limits can be seen. From Figure 5.6, it can be seen that the values of the β_x functions are the highest just before the two IPs ($\beta_x \approx 3671\,\text{m}$ at QC4L.1 at 80 GeV), meaning the beam size is the largest at these locations, explaining why the bottlenecks are found in the dipole-quadrupole-dipole trio just before the IPs.

Table 5.2 presents a summary of the horizontal aperture bottlenecks for the on-momentum particles. The normalised aperture limits with no tolerances range from $17.03\,\sigma$, the lowest at 80 GeV, to $30.11\,\sigma$, the highest at 45.6 GeV. One would expect the extreme aperture limits to occur at the extreme energies, however, this is not the case due to the difference in the β_x functions at each energy. Table 5.1 presents the beam size at each energy at the position of the highest β_x value, which corresponds to the position of the lowest aperture bottleneck; as

a consequence of the beta functions at each energy, the smallest beam size is around 1 mm at 45.6 GeV and the largest beam size is around 1.76 mm at 80 Gev, which explains the extreme aperture limits at these two energies. Adding the FCC-ee tolerances reduces the aperture limit to $14.88\,\sigma$ at 80 GeV and $26.31\,\sigma$ at 45.6 GeV. With the HL-LHC tolerances, the lowest limit decreases further to around $13\,\sigma$ at 80 GeV.

Figure 5.5 shows a comparison of the normalised aperture limits calculated in one dimension using Eq. (3.3), considering the horizontal plane only, with the MAD-X calculation. There is good agreement between the two methods. The 1D calculation is only valid when the bottleneck purely lies in the plane that is being considered, as opposed to a skew plane where the halo would be tilted, and the good agreement with the more detailed model in MAD-X shows that the found aperture bottlenecks are effectively in the horizontal plane. Figure 5.4 shows the shape of the halo at each beam energy, which was calculated using the design emittances, and confirms that the bottleneck fully lies in the horizontal plane, validating the 1D calculation results.

Beam Energy (GeV)	β_x **(m)**	**Horizontal Emittance (nm)**	**Beam Size (mm)**
45.6	3700	0.27	1.00
80	3700	0.84	1.76
120	2400	0.63	1.23
175	1500	1.34	1.42
182.5	1500	1.46	1.48

Table 5.1: Estimates of the beam size at the position of the highest on-momentum β_x value at each energy, calculated using the design emittances. The smallest beam size is at 45.6 GeV and the largest beam size is at 80 GeV.

Vertical Plane

Figures 5.7 and 5.8 present the beam-stay-clear values around the ring calculated for on-momentum particles in the vertical plane using BBEAT = 5 and BBEAT = 10 respectively. Once again, the aperture bottlenecks are located around the interaction points IPG and IPA, and Figures 5.9 and 5.10 present a closer view of IPG. Table 5.3 presents a summary of the vertical aperture bottlenecks for the on-momentum particles. From this, it can be seen that the bare structure of the lattice has very liberal normalised aperture limits, ranging from around $105\,\sigma$, the lowest at 182.5 GeV, to around $170\,\sigma$, the highest at 45.6 GeV. With the addition of the FCC-ee tolerances, the normalised aperture limits decrease significantly to around $20.52\,\sigma$

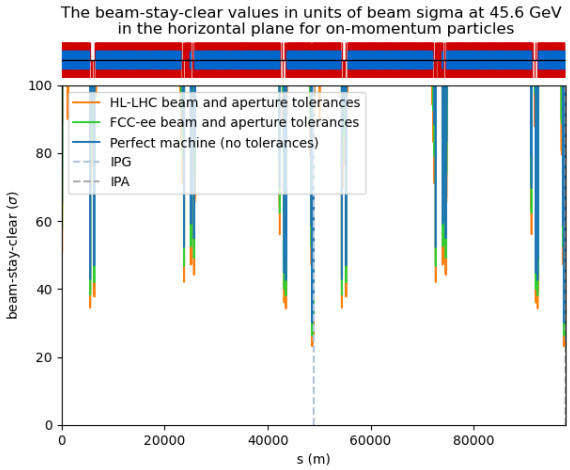

(a) 45.6 GeV

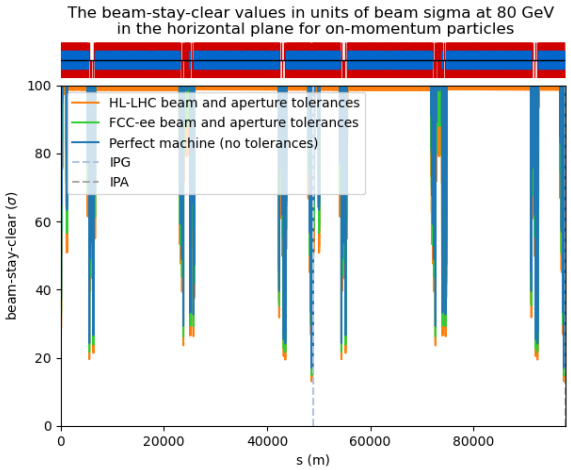

(b) 80 GeV

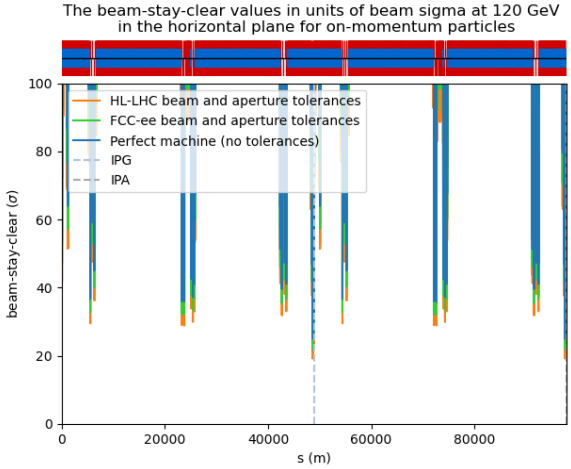

(c) 120 GeV

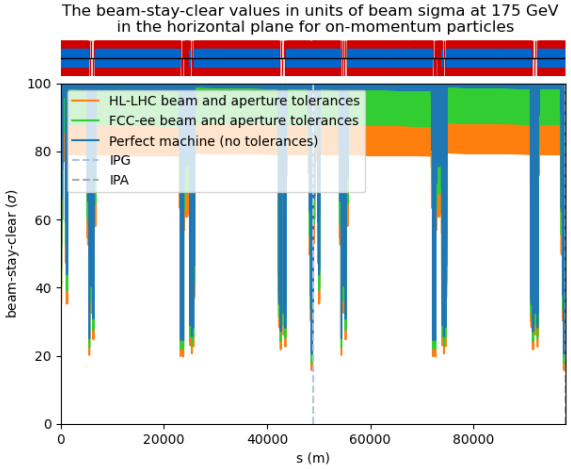

(d) 175 GeV

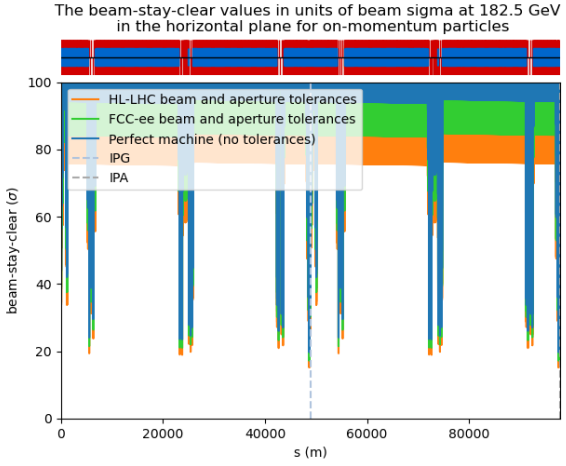

(e) 182.5 GeV

Figure 5.2: The beam-stay-clear around the full lattice for **on-momentum** particles in the **horizontal** plane for each beam energy from the MAD-X calculations. The beam-stay-clear calculated using: 1) no errors is given in blue, 2) FCC-ee tolerances is given in green, 3) HL-LHC tolerances is given in orange. The positions of IPG and IPA have been marked, with the lattice starting from and beginning in the middle of IPA. Above each plot is a schematic diagram of the lattice layout: the central black line indicates drift space, the blue indicates dipoles, and the red elements above and below the drift space represent focusing and defocusing quadrupoles respectively.

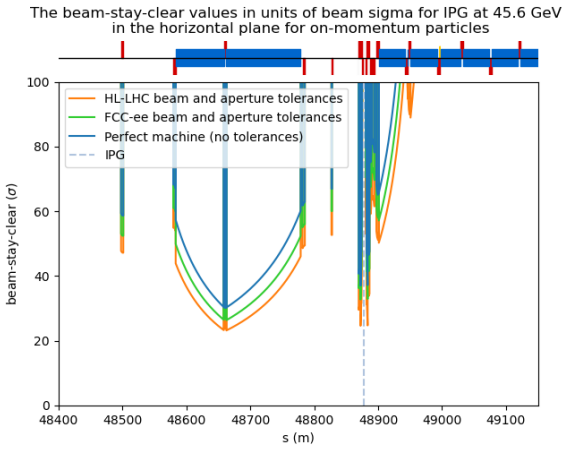

(a) 45.6 GeV

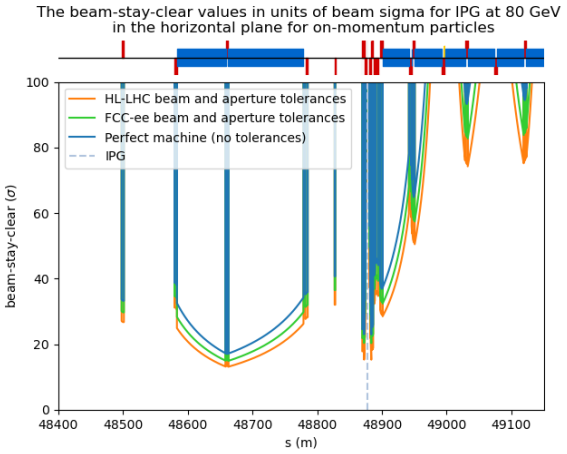

(b) 80 GeV

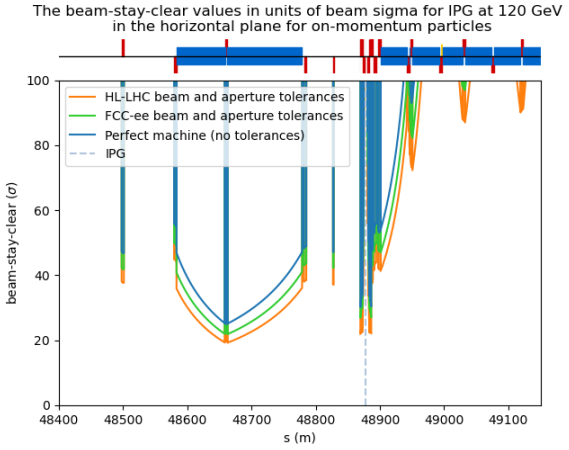

(c) 120 GeV

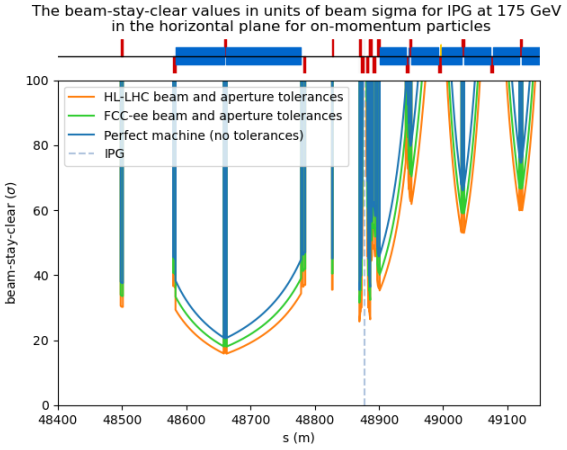

(d) 175 GeV

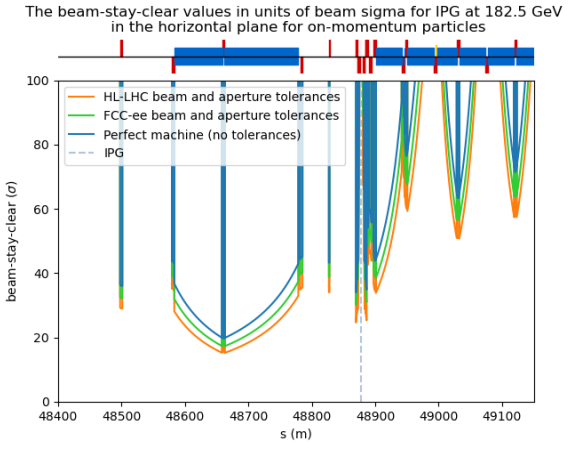

(e) 182.5 GeV

Figure 5.3: A close-up of the beam-stay-clear at the interaction point IPG (marked in light blue) for **on-momentum** particles in the **horizontal** plane for each beam energy from the MAD-X calculations. The beam-stay-clear calculated using: 1) no errors is given in blue, 2) FCC-ee tolerances is given in green, 3) HL-LHC tolerances is given in orange. Above each plot is a schematic diagram of the lattice layout: the central black line indicates drift space, the blue indicates dipoles, and the red elements above and below the drift space represent focusing and defocusing quadrupoles respectively.

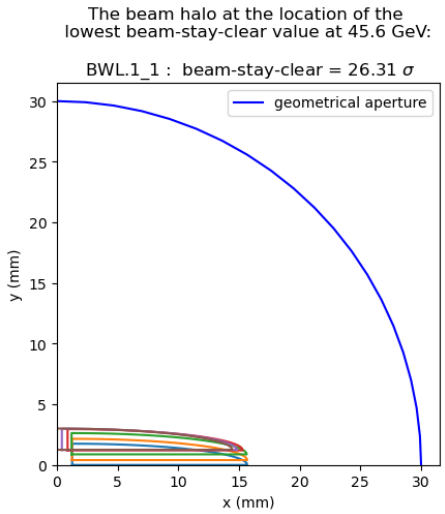

(a) 45.6 GeV

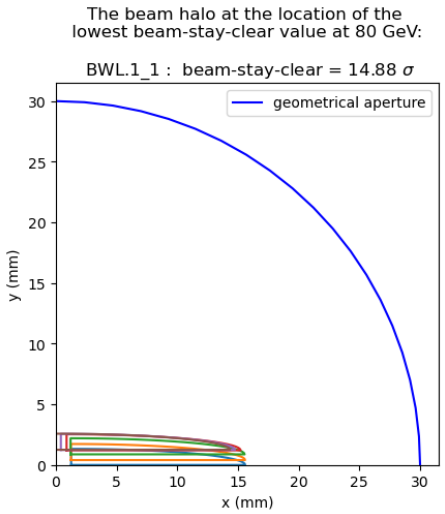

(b) 80 GeV

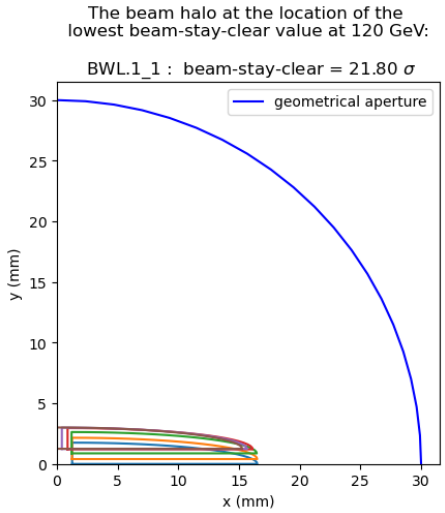

(c) 120 GeV

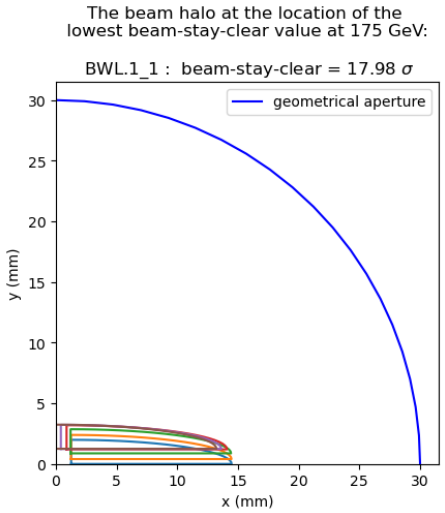

(d) 175 GeV

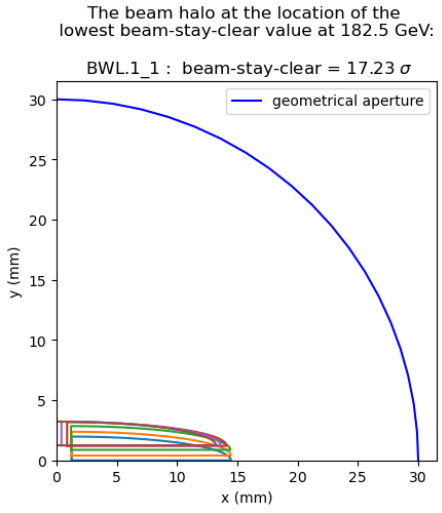

(e) 182.5 GeV

Figure 5.4: The shape of the beam halo in real space in the transverse plane at the location (given by the name of the element with the slice number after the underscore) of the horizontal aperture bottleneck for the on-momentum MAD-X calculation for each beam energy. These were calculated using the design horizontal and vertical emittances, where the former is 500 times larger than the latter, demonstrating that the aperture bottleneck naturally lies in the horizontal plane.

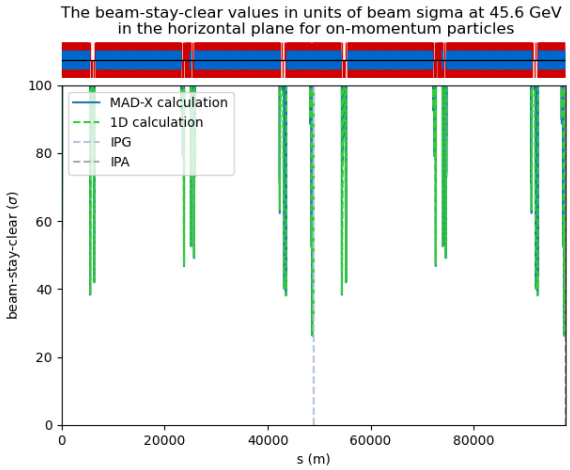

(a) 45.6 GeV

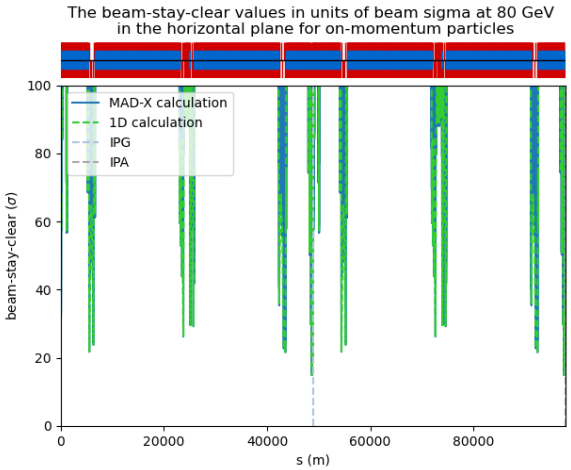

(b) 80 GeV

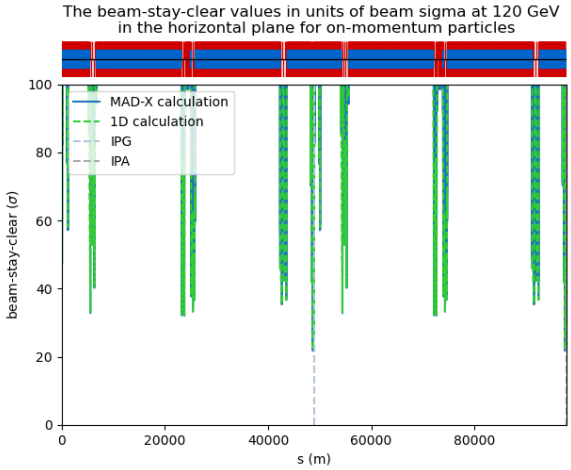

(c) 120 GeV

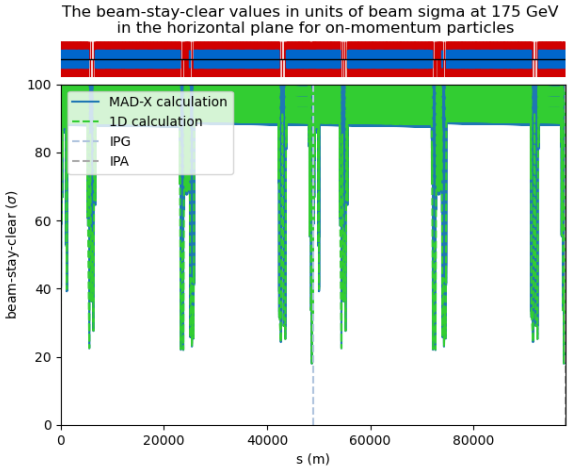

(d) 175 GeV

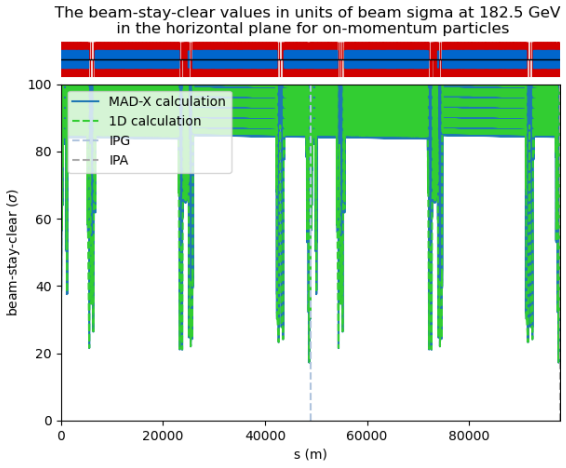

(e) 182.5 GeV

Figure 5.5: A comparison of the 1D aperture calculation and MAD-X calculation of the beam-stay-clear around the full lattice for **on-momentum** particles in the **horizontal** plane for each beam energy. The results from the 1D calculation are given in green and those from the MAD-X calculation are given in blue. The positions of IPG and IPA have been marked, with the lattice starting from and beginning in the middle of IPA. Above each plot is a schematic diagram of the lattice layout: the central black line indicates drift space, the blue indicates dipoles, and the red elements above and below the drift space represent focusing and defocusing quadrupoles respectively.

Beam Energy [GeV]	Element	Type	s [m]	beam-stay-clear (σ)			s [m] (for twiss)	Momentum Acceptance - 0 σ	Momentum Acceptance - 7 σ	Momentum Acceptance - 8 σ
				No Tolerance	FCC - ee Tolerances	HL - LHC Tolerances				
45.6	BC1L.1	Dipole	48658.52735	30.36	26.42	23.23	48658.52735	0.578	0.445	0.426
	QC4L.1	Quadrupole	48661.16068	**30.11**	26.83	23.69	48662.32735	0.603	0.463	0.443
	BWL.1	Dipole	48662.62735	30.24	**26.31**	**23.14**	48778.79803	21463.651	18966.468	18609.728
	BC1L.2	Dipole	97536.55949	30.36	26.42	23.23	97536.55949	0.578	0.445	0.426
	QC4L.2	Quadrupole	97539.19282	**30.11**	26.83	23.69	97540.35949	0.603	0.463	0.443
	BWL.2	Dipole	97540.65949	30.24	**26.31**	**23.14**	97656.83018	21691.687	19167.973	18807.443
80	BC1L.1	Dipole	48658.52735	17.17	14.94	13.14	48658.52735	0.578	0.343	0.309
	QC4L.1	Quadrupole	48661.16068	**17.03**	15.18	13.40	48662.32735	0.603	0.356	0.321
	BWL.1	Dipole	48662.62735	17.11	**14.88**	**13.09**	48778.79803	4002.530	3184.490	3067.627
	BC1L.2	Dipole	97536.55949	17.17	14.94	13.14	97536.55949	0.578	0.343	0.309
	QC4L.2	Quadrupole	97539.19282	**17.03**	15.18	13.40	97540.35949	0.603	0.356	0.321
	BWL.2	Dipole	97540.65949	17.11	**14.88**	**13.09**	97656.83018	4231.286	3366.493	3242.951
120	BC1L.1	Dipole	48658.52735	25.17	21.90	19.26	48658.52735	0.578	0.417	0.394
	QC4L.1	Quadrupole	48661.16068	**24.96**	22.24	19.64	48662.32735	0.603	0.434	0.410
	BWL.1	Dipole	48662.62735	25.06	**21.80**	**19.17**	48778.79803	4197.707	3574.677	3485.672
	BC1L.2	Dipole	97536.55949	25.17	21.90	19.26	97536.55949	0.578	0.417	0.394
	QC4L.2	Quadrupole	97539.19282	**24.96**	22.24	19.64	97540.35949	0.603	0.434	0.410
	BWL.2	Dipole	97540.65949	25.06	**21.80**	**19.17**	97656.83018	4113.676	3503.118	3415.895
175	BC1L.1	Dipole	48658.52735	20.73	18.04	15.86	48658.52735	0.578	0.383	0.355
	QC4L.1	Quadrupole	48661.16068	**20.57**	18.33	16.18	48662.32735	0.603	0.398	0.369
	BWL.1	Dipole	48662.62735	20.67	**17.98**	**15.81**	48778.79803	2218.432	1872.505	1823.086
	BC1L.2	Dipole	97536.55949	20.73	18.04	15.86	97536.55949	0.578	0.383	0.355
	QC4L.2	Quadrupole	97539.19282	**20.57**	18.33	16.18	97540.35949	0.603	0.398	0.369
	BWL.2	Dipole	97540.65949	20.67	**17.98**	**15.81**	97656.83018	1847.934	1559.780	1518.615
182.5	BC1L.1	Dipole	48658.52735	19.86	17.28	15.20	48658.52735	0.578	0.374	0.345
	QC4L.1	Quadrupole	48661.16068	**19.71**	17.56	15.50	48662.32735	0.603	0.389	0.359
	BWL.1	Dipole	48662.62735	19.80	**17.23**	**15.15**	48778.79803	1935.917	1620.821	1575.807
	BC1L.2	Dipole	97536.55949	19.86	17.28	15.20	97536.55949	0.578	0.374	0.345
	QC4L.2	Quadrupole	97539.19282	**19.71**	17.56	15.50	97540.35949	0.603	0.389	0.359
	BWL.2	Dipole	97540.65949	19.80	**17.23**	**15.15**	97656.83018	1703.386	1426.137	1386.530

Table 5.2: Summary of the **horizontal** aperture bottlenecks for the **on-momentum** particles at each beam energy calculated in MAD-X using no tolerances, the FCC-ee tolerances, and HL-LHC tolerances, with the corresponding maximum momentum acceptance at each element. The lowest beam-stay-clear values are in bold for each beam energy and tolerance set. The first s column corresponds to the position of the element slice at which the lowest beam-stay-clear value was found, and the second s column corresponds to the position at which the maximum momentum acceptance was calculated for that element as the optical Twiss functions are evaluated at the end of each element.

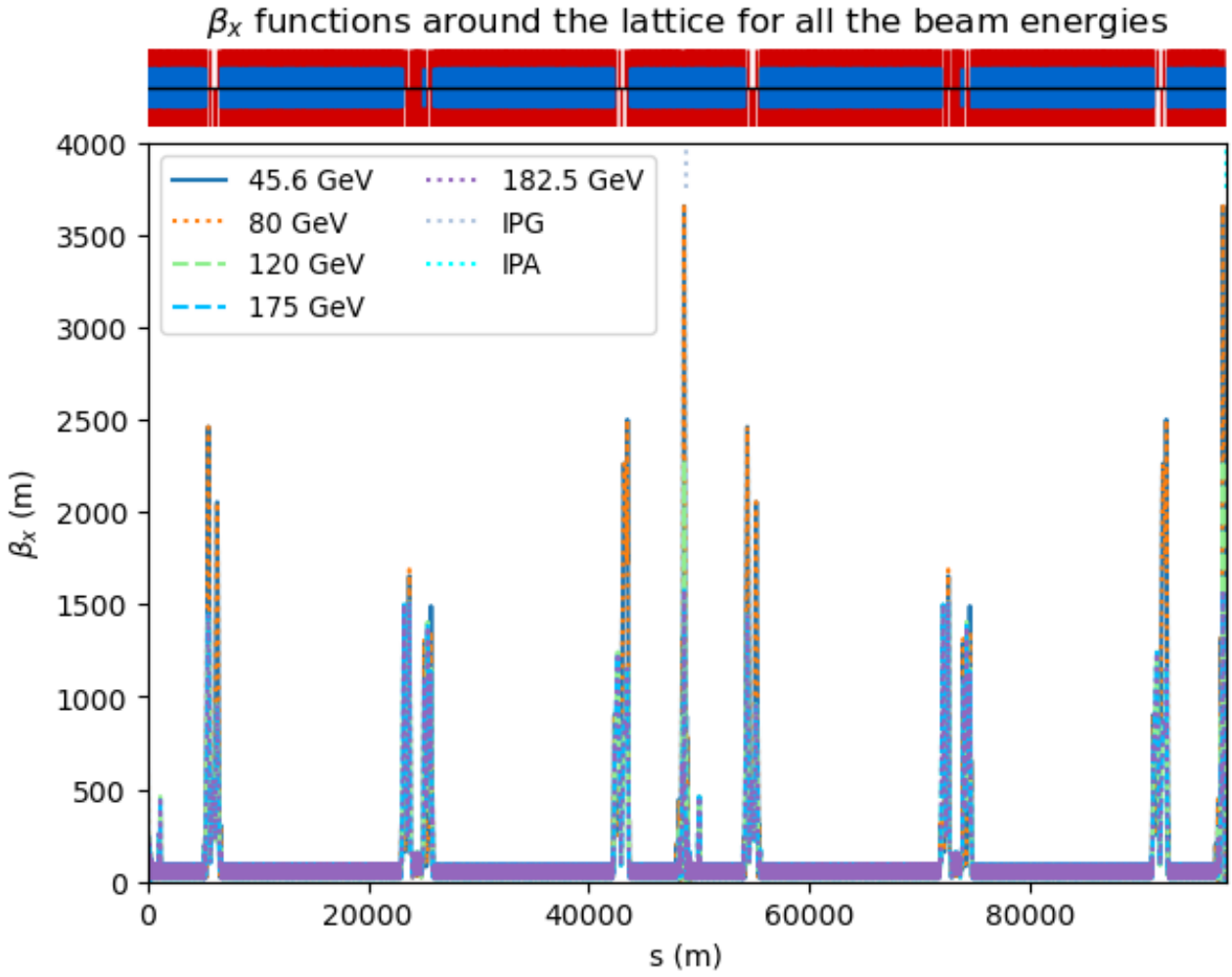

Figure 5.6: The β_x function around the ring for each of the beam energies for **on-momentum** particles, with the positions of the interaction points IPG and IPA marked. Above the plot is a schematic diagram of the lattice layout: the central black line indicates drift space, the blue indicates dipoles, and the red elements above and below the drift space represent focusing and defocusing quadrupoles respectively.

at 182.5 GeV and 33.19 σ at 45.6 GeV when using BBEAT = 5. And with twice the beam size increase factor, BBEAT = 10, the normalised aperture limits are almost half those calculated using BBEAT = 5, ranging from 10.26 σ at 182.5 GeV to 16.59 σ at 45.6 GeV. This demonstrates the large impact that imperfect equilibrium emittances and coupling, on top of beta-beating, have on the available normalised vertical aperture. In practical terms, if the collimator openings were to be placed at a minimum of 8 σ, in order to guarantee beam lifetime, the available normalised aperture would have to be at least 10 σ to allow room for the collimators, which is one of the bottlenecks at 182.5 GeV with BBEAT = 10. Ideally, to allow some operational margins, the minimum aperture should even be a few beam σ larger. This motivates the need for local optics corrections in order to reduce the beam size increase in both planes, as effects such as beam-beam have not yet been accounted for in the optics studies, which would contribute to beam growth.

The elements containing the vertical aperture bottlenecks are the quadrupoles on either side of the interaction points IPG and IPA, which can be seen in the beam lines above each plots in Figures 5.9 and 5.10; the lattice starts from and ends in the middle of IPA, and IPG is located at around s = 48 878 m. Figure 5.14 shows the β_y function around the ring for on-momentum particles at each beam energy. The highest values of β_y are located very close to the IPs ($\beta_y \approx$ 8783 m at QC1R2.2 at 120 GeV), resulting in large beam sizes, explaining why the bottlenecks are located at these positions.

Figures 5.12 and 5.13 show a comparison of the normalised aperture limits calculated in one dimension with the MAD-X calculation using BBEAT = 5 and BBEAT = 10 respectively. Once again, there is a good agreement between the two methods because the aperture bottleneck lies purely in the vertical plane, as shown in Figure 5.11, validating the 1D calculation. This confirms that the method of setting the horizontal emittances to be 100 times smaller in magnitude than the vertical design emittances does indeed bias the halo to lie in the vertical plane, allowing for the vertical aperture to be studied. It should be noted that the halo plots using BBEAT = 10 would be the exact same as those in Figure 5.11, which were produced using BBEAT = 5, except with a lower beam-stay-clear value.

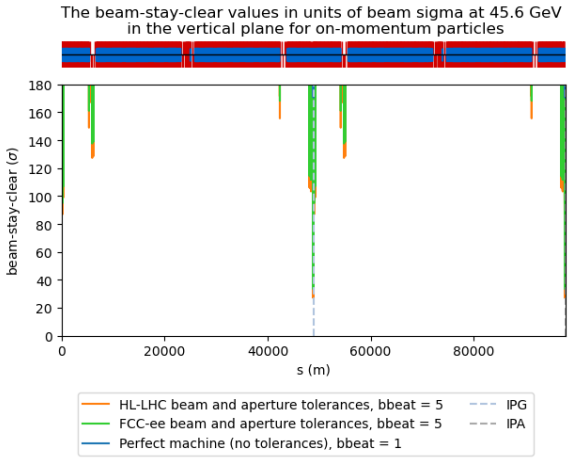

(a) 45.6 GeV

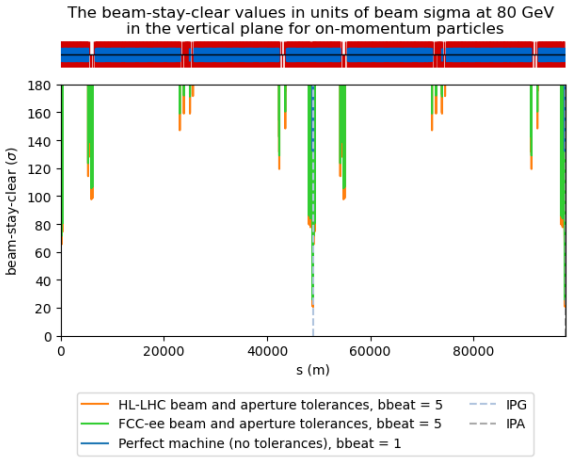

(b) 80 GeV

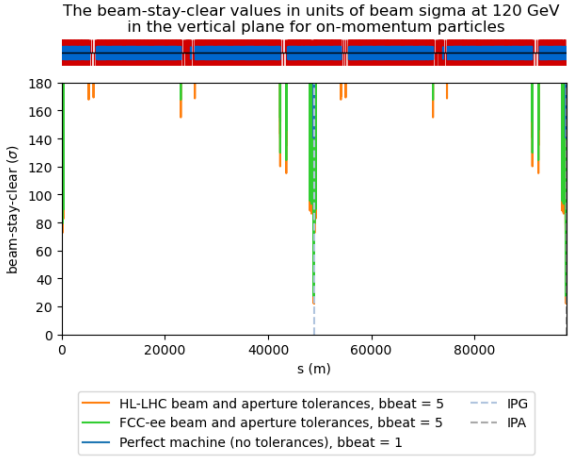

(c) 120 GeV

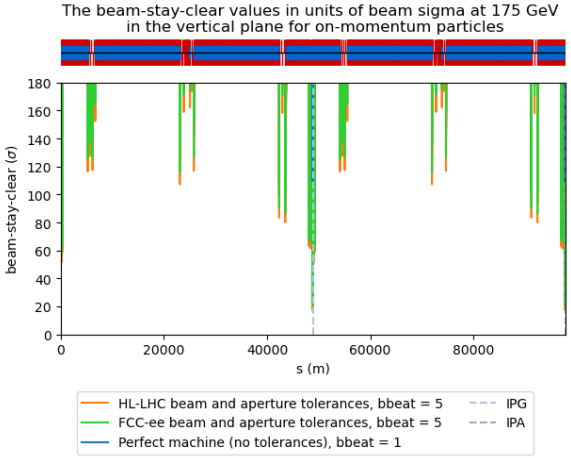

(d) 175 GeV

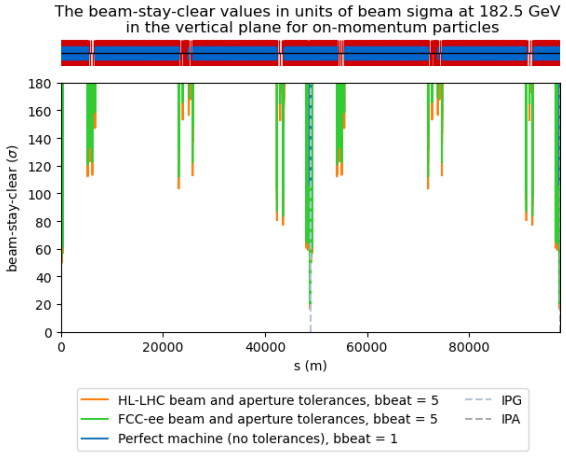

(e) 182.5 GeV

Figure 5.7: The beam-stay-clear around the full lattice for **on-momentum** particles in the **vertical** plane for each beam energy from the MAD-X calculations using **BBEAT = 5** with the FCC-ee tolerances and HL-LHC tolerances. The beam-stay-clear calculated using: 1) no errors is given in blue, 2) FCC-ee tolerances is given in green, 3) HL-LHC tolerances is given in orange. The positions of IPG and IPA have been marked, with the lattice starting from and beginning in the middle of IPA. Above each plot is a schematic diagram of the lattice layout: the central black line indicates drift space, the blue indicates dipoles, and the red elements above and below the drift space represent focusing and defocusing quadrupoles respectively.

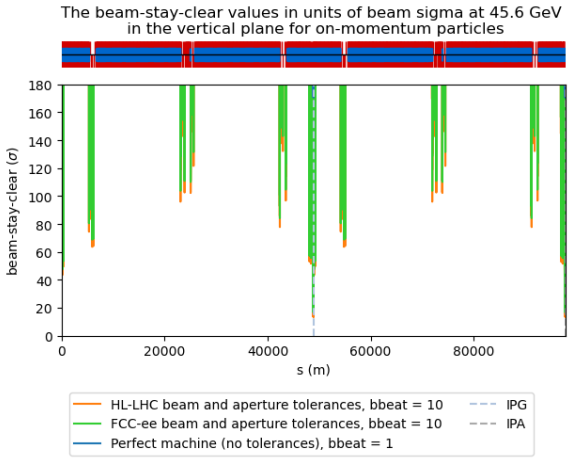

(a) 45.6 GeV

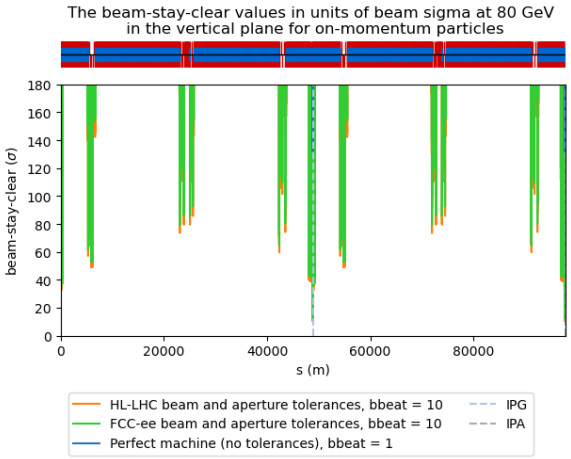

(b) 80 GeV

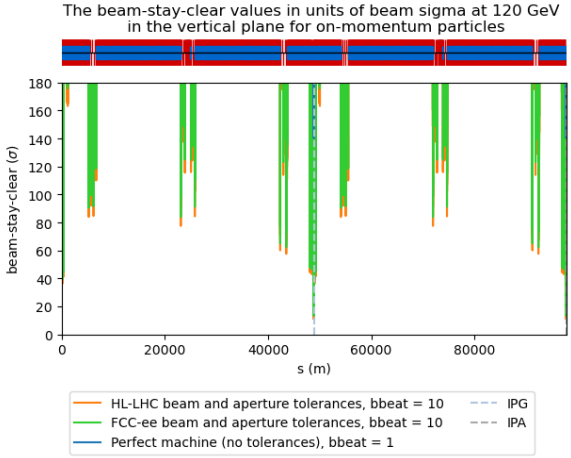

(c) 120 GeV

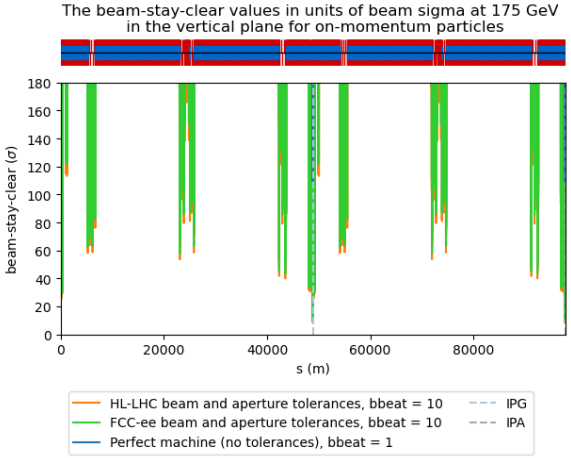

(d) 175 GeV

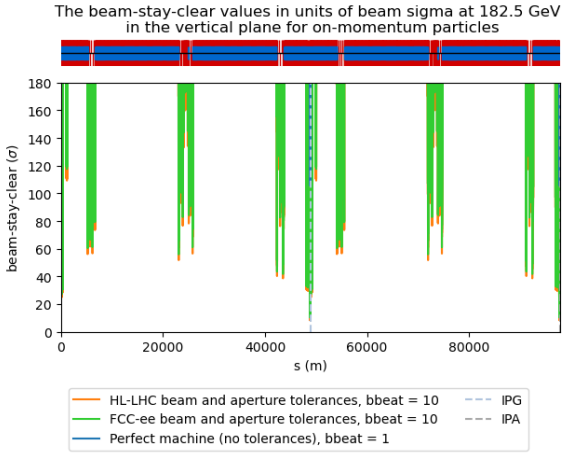

(e) 182.5 GeV

Figure 5.8: The beam-stay-clear around the full lattice for **on-momentum** particles in the **vertical** plane for each beam energy from the MAD-X calculations using **BBEAT = 10** with the FCC-ee tolerances and HL-LHC tolerances. The beam-stay-clear calculated using: 1) no errors is given in blue, 2) FCC-ee tolerances is given in green, 3) HL-LHC tolerances is given in orange. The positions of IPG and IPA have been marked, with the lattice starting from and beginning in the middle of IPA. Above each plot is a schematic diagram of the lattice layout: the central black line indicates drift space, the blue indicates dipoles, and the red elements above and below the drift space represent focusing and defocusing quadrupoles respectively.

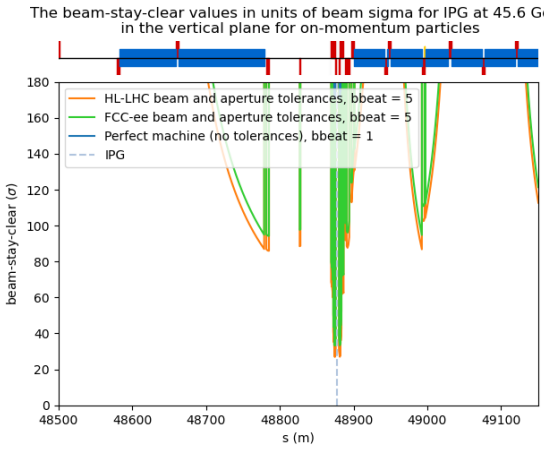

(a) 45.6 GeV

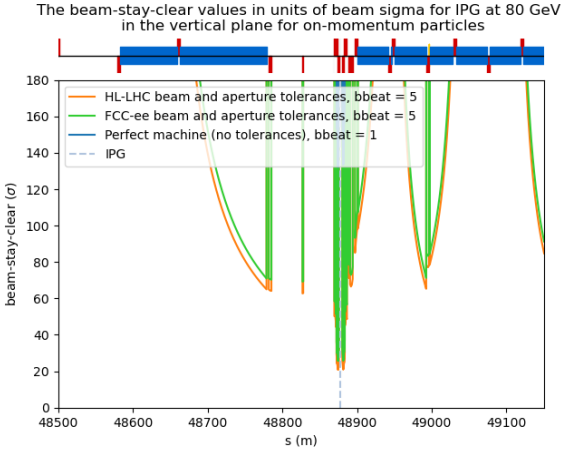

(b) 80 GeV

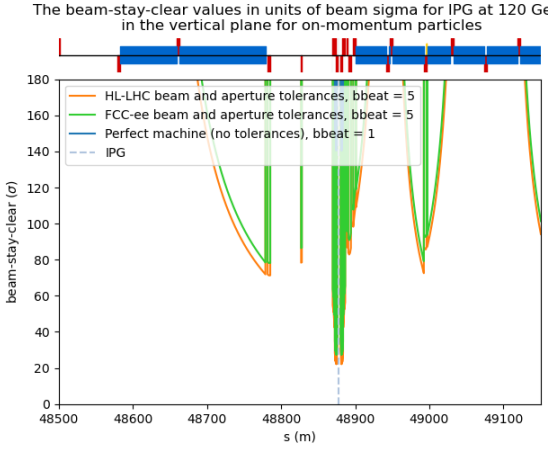

(c) 120 GeV

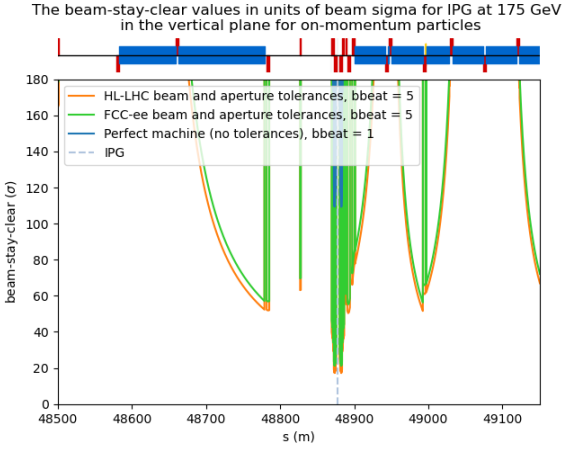

(d) 175 GeV

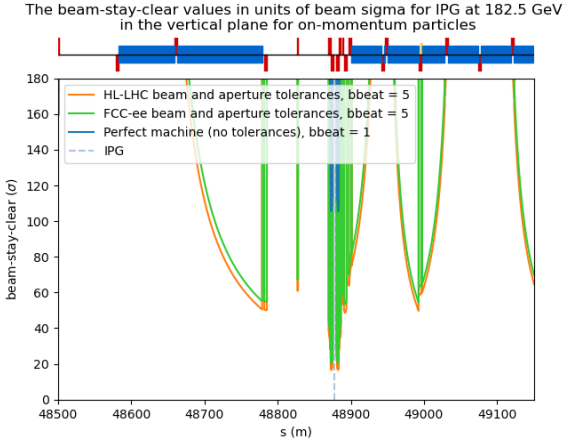

(e) 182.5 GeV

Figure 5.9: A close-up of the beam-stay-clear at the interaction point IPG (marked in light blue) for **on-momentum** particles in the **vertical** plane for each beam energy using **BBEAT = 5** with the FCC-ee tolerances and HL-LHC tolerances. The beam-stay-clear calculated in MAD-X using: 1) no errors is given in blue, 2) FCC-ee tolerances is given in green, 3) HL-LHC tolerances is given in orange. Above each plot is a schematic diagram of the lattice layout: the central black line indicates drift space, the blue indicates dipoles, and the red elements above and below the drift space represent focusing and defocusing quadrupoles respectively.

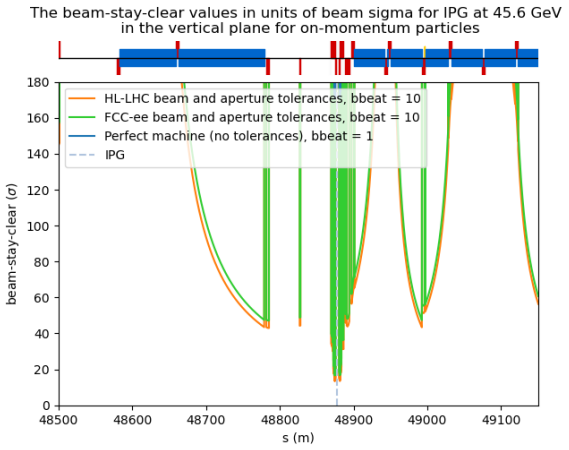

(a) 45.6 GeV

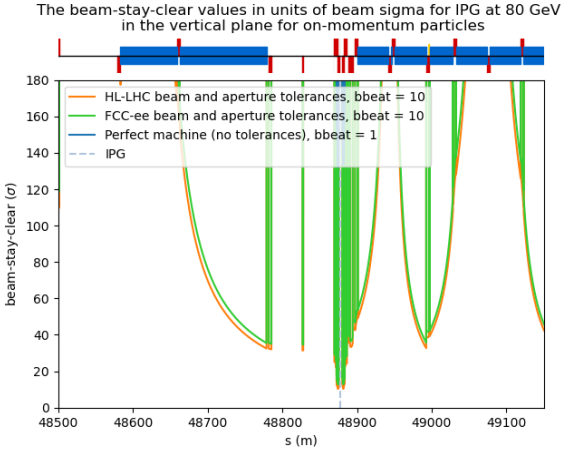

(b) 80 GeV

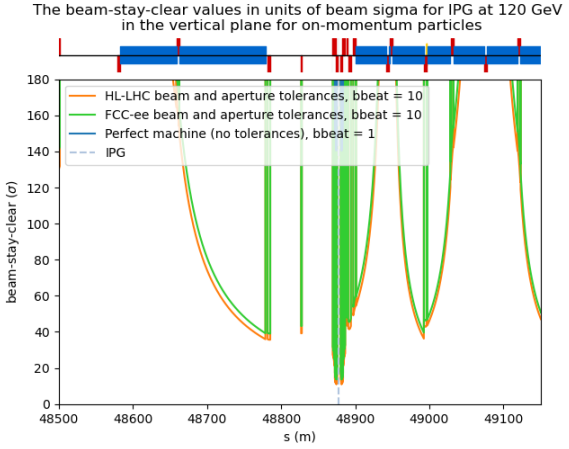

(c) 120 GeV

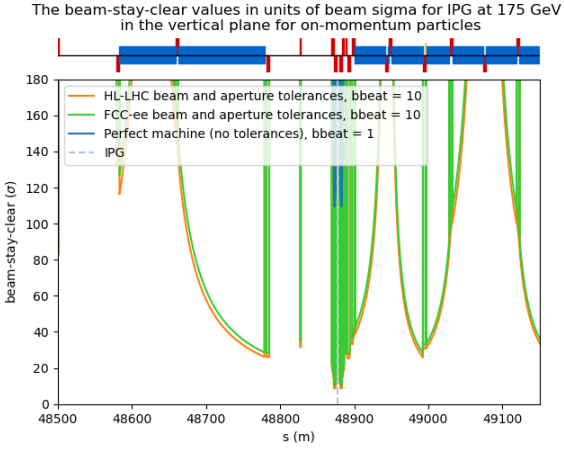

(d) 175 GeV

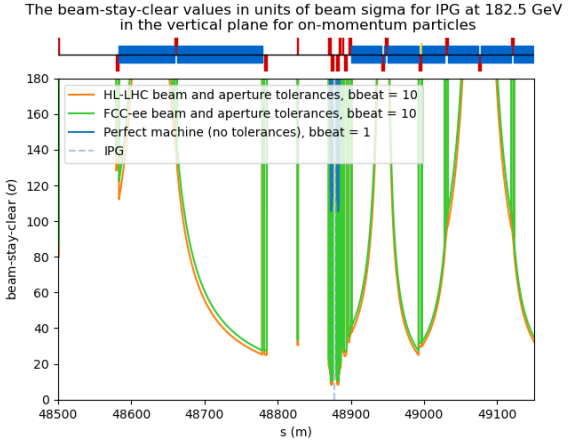

(e) 182.5 GeV

Figure 5.10: A close-up of the beam-stay-clear at the interaction point IPG (marked in light blue) for **on-momentum** particles in the **vertical** plane for each beam energy using **BBEAT = 10** with the FCC-ee tolerances and HL-LHC tolerances. The beam-stay-clear calculated in MAD-X using: 1) no errors is given in blue, 2) FCC-ee tolerances is given in green, 3) HL-LHC tolerances is given in orange. Above each plot is a schematic diagram of the lattice layout: the central black line indicates drift space, the blue indicates dipoles, and the red elements above and below the drift space represent focusing and defocusing quadrupoles respectively.

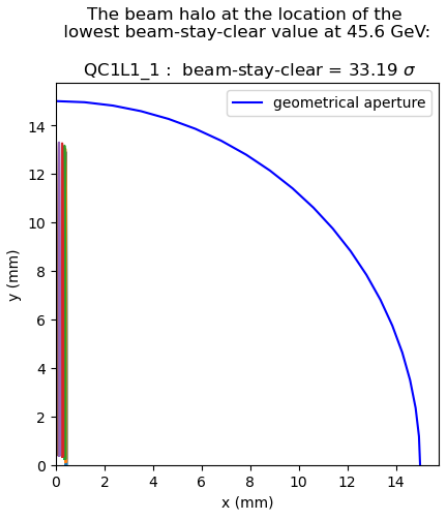

(a) 45.6 GeV

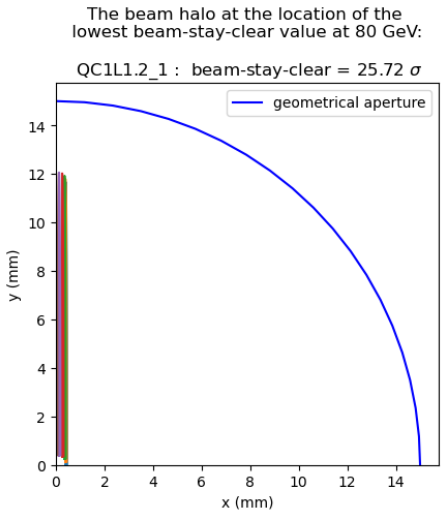

(b) 80 GeV

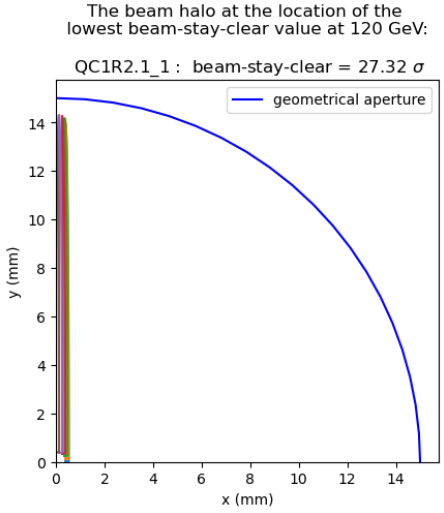

(c) 120 GeV

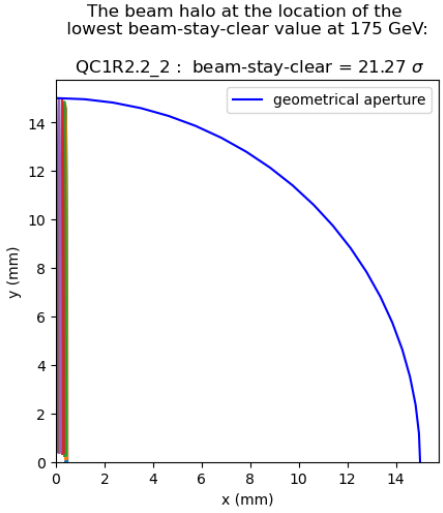

(d) 175 GeV

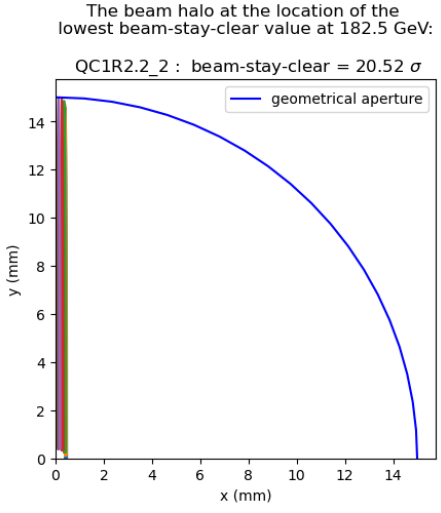

(e) 182.5 GeV

Figure 5.11: The shape of the beam halo in real space in the transverse plane at the location (given by the name of the element with the slice number after the underscore) of the vertical aperture bottleneck for the on-momentum MAD-X calculation for each beam energy, using **BBEAT = 5**. These were calculated using the horizontal emittances that were set to be 100 times smaller than the vertical design emittances, in order to bias the results and probe the vertical plane.

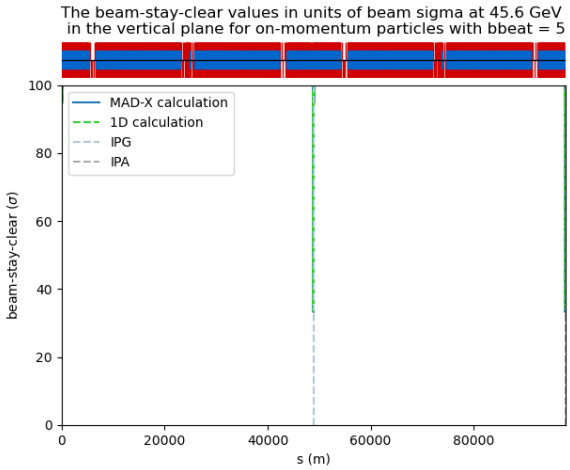

(a) 45.6 GeV

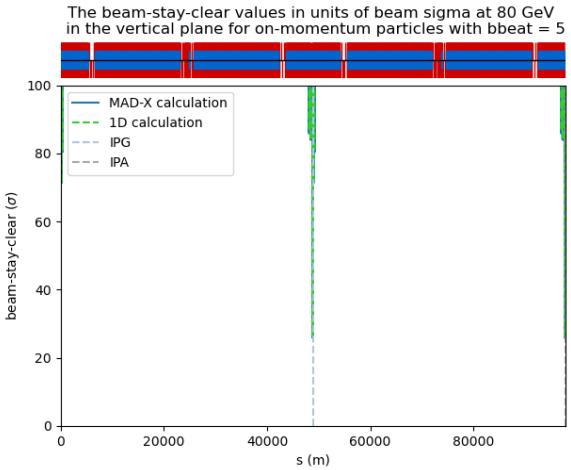

(b) 80 GeV

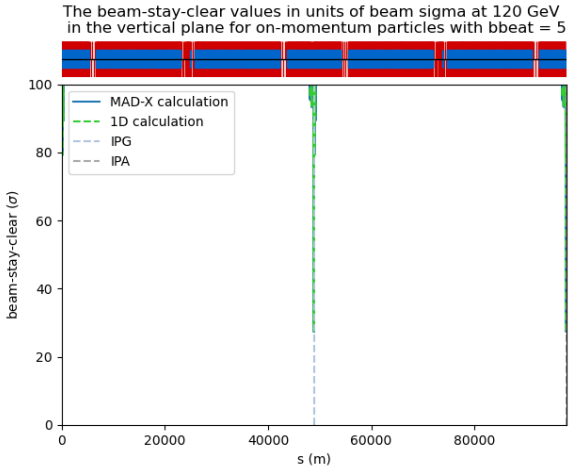

(c) 120 GeV

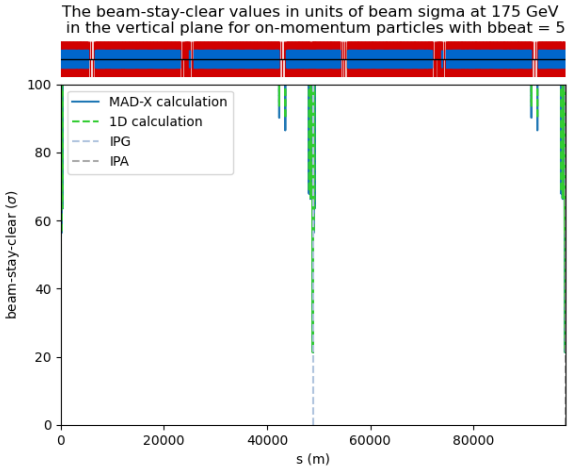

(d) 175 GeV

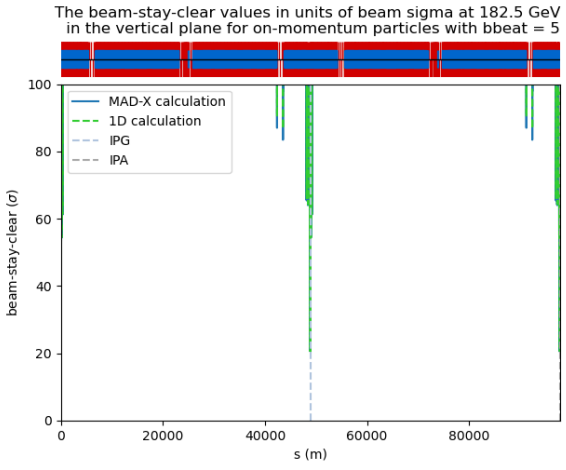

(e) 182.5 GeV

Figure 5.12: A comparison of the 1D aperture calculation and MAD-X calculation of the beam-stay-clear around the full lattice for **on-momentum** particles in the **vertical** plane for each beam energy using **BBEAT = 5** with the FCC-ee tolerances and HL-LHC tolerances. The results from the 1D calculation are given in green and those from the MAD-X calculation are given in blue. The positions of IPG and IPA have been marked, with the lattice starting from and beginning in the middle of IPA. Above each plot is a schematic diagram of the lattice layout: the central black line indicates drift space, the blue indicates dipoles, and the red elements above and below the drift space represent focusing and defocusing quadrupoles respectively.

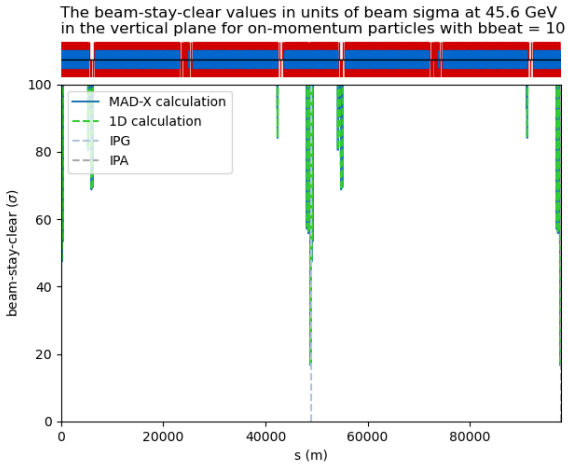

(a) 45.6 GeV

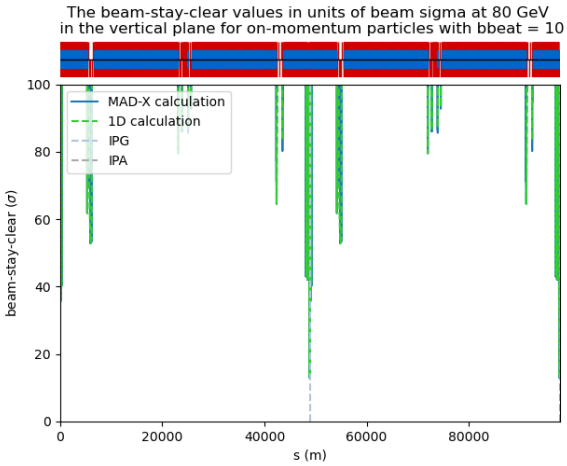

(b) 80 GeV

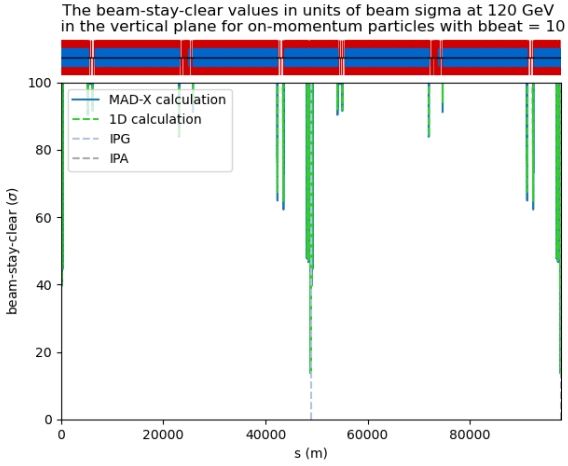

(c) 120 GeV

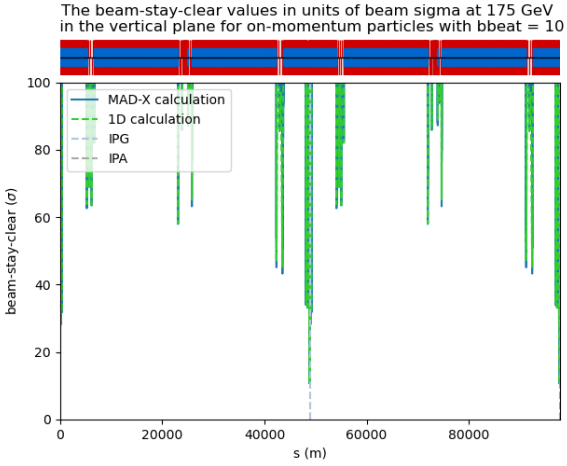

(d) 175 GeV

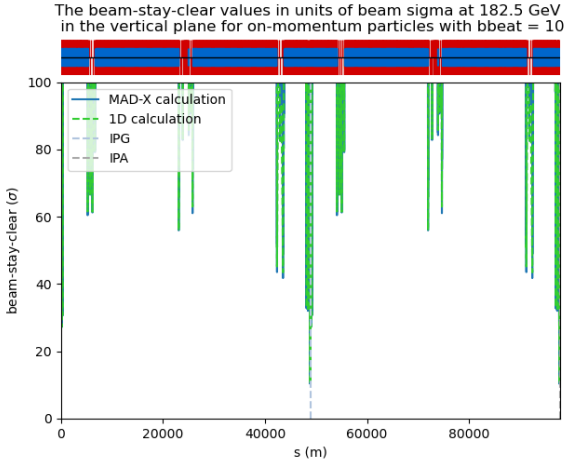

(e) 182.5 GeV

Figure 5.13: A comparison of the 1D aperture calculation and MAD-X calculation of the beam-stay-clear around the full lattice for **on-momentum** particles in the **vertical** plane for each beam energy using **BBEAT = 10** with the FCC-ee tolerances and HL-LHC tolerances. The results from the 1D calculation are given in green and those from the MAD-X calculation are given in blue. The positions of IPG and IPA have been marked, with the lattice starting from and beginning in the middle of IPA. Above each plot is a schematic diagram of the lattice layout: the central black line indicates drift space, the blue indicates dipoles, and the red elements above and below the drift space represent focusing and defocusing quadrupoles respectively.

Beam Energy [GeV]	Element	Type	s [m]	beam-stay-clear (σ)				
				No Tolerance	FCC - ee Tolerances		HL - LHC Tolerances	
				BBEAT = 1	BBEAT = 5	BBEAT = 10	BBEAT = 5	BBEAT = 10
45.6	QC1R1.1	Quadrupole	3.400225021	171.34	33.34	16.67	27.00	13.50
	QC1R2.1	Quadrupole	3.480225021	174.55	33.97	16.98	27.51	13.75
	QC1L2.1	Quadrupole	48874.55192	173.62	33.79	16.89	27.36	13.68
	QC1L1.1	Quadrupole	48874.63192	**170.54**	**33.19**	**16.59**	**26.88**	**13.44**
	QC1R1.2	Quadrupole	48881.43237	171.34	33.34	16.67	27.00	13.50
	QC1R2.2	Quadrupole	48881.51237	174.55	33.97	16.98	27.51	13.75
	QC1L2.2	Quadrupole	97752.58406	173.62	33.79	16.89	27.36	13.68
	QC1L1.2	Quadrupole	97752.66406	**170.54**	**33.19**	**16.59**	**26.88**	**13.44**
80	QC1R1.1	Quadrupole	3.400225021	133.37	25.95	12.98	21.02	10.51
	QC1R2.1	Quadrupole	3.480225021	134.00	26.08	13.04	21.12	10.56
	QC1L2.1	Quadrupole	48874.55192	132.63	25.81	12.90	20.90	10.45
	QC1L1.1	Quadrupole	48874.63192	**132.17**	**25.72**	**12.86**	**20.83**	**10.42**
	QC1R1.2	Quadrupole	48881.43237	133.37	25.95	12.98	21.02	10.51
	QC1R2.2	Quadrupole	48881.51237	134.00	26.08	13.04	21.12	10.56
	QC1L2.2	Quadrupole	97752.58406	132.63	25.81	12.90	20.90	10.45
	QC1L1.2	Quadrupole	97752.66406	**132.17**	**25.72**	**12.86**	**20.83**	**10.42**
120	QC1R1.1	Quadrupole	3.400225021	141.17	27.47	13.74	22.25	11.12
	QC1R2.1	Quadrupole	3.480225021	**140.38**	**27.32**	**13.66**	**22.12**	**11.06**
	QC1L2.1	Quadrupole	48874.55192	140.45	27.33	13.67	22.13	11.07
	QC1L1.1	Quadrupole	48874.63192	141.23	27.48	13.74	22.26	11.13
	QC1R1.2	Quadrupole	48881.43237	141.17	27.47	13.74	22.25	11.12
	QC1R2.2	Quadrupole	48881.51237	**140.38**	**27.32**	**13.66**	**22.12**	**11.06**
	QC1L2.2	Quadrupole	97752.58406	140.45	27.33	13.67	22.13	11.07
	QC1L1.2	Quadrupole	97752.66406	141.23	27.48	13.74	22.26	11.13
175	QC1R1.1	Quadrupole	3.400225021	117.79	22.92	11.46	18.56	9.28
	QC1R2.1	Quadrupole	4.480225021	**109.31**	**21.27**	**10.64**	**17.23**	**8.61**
	QC1R3.1	Quadrupole	4.560225021	109.49	21.31	10.65	17.26	8.63
	QC1L3.1	Quadrupole	48873.47192	109.62	21.33	10.67	17.28	8.64
	QC1L2.1	Quadrupole	48873.55192	109.43	21.29	10.65	17.25	8.62
	QC1L1.1	Quadrupole	48874.63192	117.83	22.93	11.46	18.57	9.29
	QC1R1.2	Quadrupole	48881.43237	117.79	22.92	11.46	18.56	9.28
	QC1R2.2	Quadrupole	48882.51237	**109.31**	**21.27**	**10.64**	**17.23**	**8.61**
	QC1R3.2	Quadrupole	48882.59237	109.49	21.31	10.65	17.26	8.63
	QC1L3.2	Quadrupole	97751.50406	109.62	21.33	10.67	17.28	8.64
	QC1L2.2	Quadrupole	97751.58406	109.43	21.29	10.65	17.25	8.62
	QC1L1.2	Quadrupole	97752.66406	117.83	22.93	11.46	18.57	9.29
182.5	QC1R1.1	Quadrupole	3.400225021	113.65	22.12	11.06	17.91	8.96
	QC1R2.1	Quadrupole	4.480225021	**105.47**	**20.52**	**10.26**	**16.62**	**8.31**
	QC1R3.1	Quadrupole	4.560225021	105.65	20.56	10.28	16.65	8.33
	QC1L3.1	Quadrupole	48873.47192	105.77	20.58	10.29	16.67	8.33
	QC1L2.1	Quadrupole	48873.55192	105.59	20.55	10.27	16.64	8.32
	QC1L1.1	Quadrupole	48874.63192	113.69	22.12	11.06	17.92	8.96
	QC1R1.2	Quadrupole	48881.43237	113.65	22.12	11.06	17.91	8.96
	QC1R2.2	Quadrupole	48882.51237	**105.47**	**20.52**	**10.26**	**16.62**	**8.31**
	QC1R3.2	Quadrupole	48882.59237	105.65	20.56	10.28	16.65	8.33
	QC1L3.2	Quadrupole	97751.50406	105.77	20.58	10.29	16.67	8.33
	QC1L2.2	Quadrupole	97751.58406	105.59	20.55	10.27	16.64	8.32
	QC1L1.2	Quadrupole	97752.66406	113.69	22.12	11.06	17.92	8.96

Table 5.3: Summary of the **vertical** aperture bottlenecks for the **on-momentum** particles at each beam energy calculated in MAD-X using no tolerances, the FCC-ee tolerances, and HL-LHC tolerances. The lowest beam-stay-clear values are in bold for each beam energy and tolerance set.

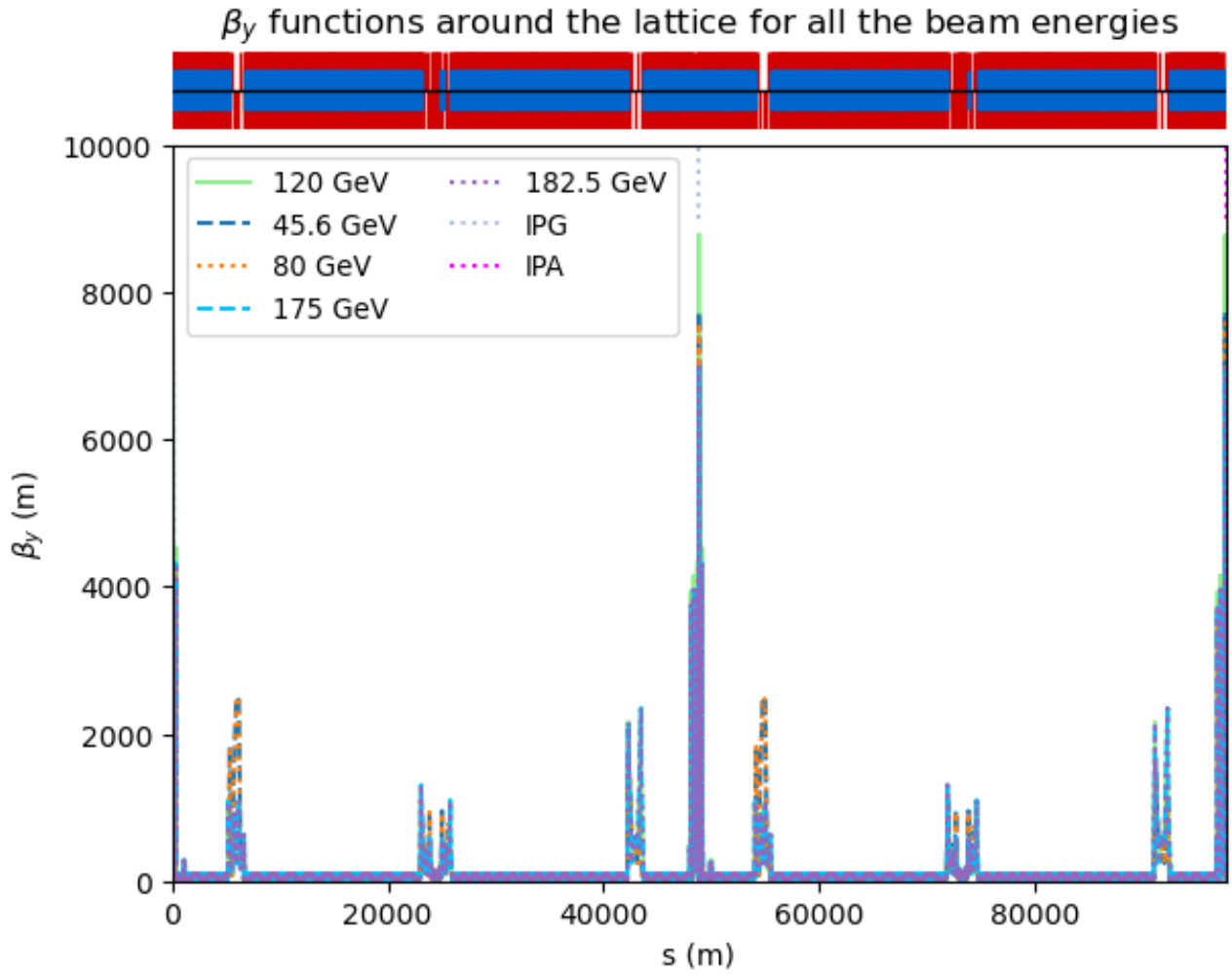

Figure 5.14: The β_y function around the ring for each of the beam energies for **on-momentum** particles, with the positions of the interaction points IPG and IPA marked. Above the plot is a schematic diagram of the lattice layout: the central black line indicates drift space, the blue indicates dipoles, and the red elements above and below the drift space represent focusing and defocusing quadrupoles respectively.

5.1.3 Off-Momentum Particles

For the off-momentum calculations, for each of the beam energies, MAD-X could not find a closed solution of the orbit and the optics. That is to say, the value of the closed orbit and optical functions (such as the beta and dispersion functions) at the beginning of the lattice differ from the values at the end of the lattice, whereas they should be identical for a closed solution. The reason for this is still to be understood in detail. The values do not differ greatly, but nevertheless this introduces a small error (yet to be quantified) on the 1D calculation results that were based on the MAD-X TWISS output. Therefore, the off-momentum 1D calculation results presented in this section only should be considered preliminary and should be taken with a significant error margin. As a further note, for the 175 GeV beam energy, the TWISS output from MAD-X contained some non-physical values, hence the off-momentum results for 175 GeV have been omitted entirely. Off-momentum aperture calculations should in any case be repeated once the correction strategy for the off-momentum lattice has been improved and finalized.

Horizontal Plane

Figure 5.15 presents the beam-stay-clear values around the ring calculated for off-momentum particles in the horizontal plane and Figure 5.16 presents a closer look at IPG, however, it is clear that for the higher beam energies the bottlenecks appear in many other elements in the ring other than those around the IPs, corresponding to the positions of high β_x in Figure 5.17. Examples of these elements include the quadrupoles QU4.1 and QU2.1 situated between $s \approx 23\,500\,\text{m}$ and $s \approx 23\,800\,\text{m}$, just before the start of the RF cavities at around $s \approx 24\,000\,\text{m}$ in the first half of the ring, and for the second half of the ring, examples include the quadrupoles QU6.2 and QU5.2 situated between $s \approx 72\,100\,\text{m}$ and $s \approx 72\,300\,\text{m}$, just before the start of the RF cavities at around $s \approx 72\,900\,\text{m}$.

Table 5.4 summarises the horizontal aperture bottlenecks for the off-momentum particles. The available normalised off-momentum aperture of the perfect machine is comparable to the normalised aperture calculated using FCC-ee tolerances and HL-LHC tolerances for the on-momentum case, except with bottlenecks that are below $8\,\sigma$ at 182.5 GeV. The available off-momentum aperture calculated using the FCC-ee tolerances and HL-LHC tolerances is al-

most half of the bare structure aperture limits, meaning there are numerous elements at 182.5 GeV with bottlenecks that are much lower than $10\,\sigma$, which would be the absolute minimum required aperture as previously stated. The machine simply cannot function with these low aperture limits, therefore the corrections of the optics should be improved such that a significantly smaller residual beam size increase is obtained, ideally no more than an increase of 20%, including coupling, equilibrium emittance and beta-beating. Additionally, the fractional horizontal parasitic dispersion should be corrected to at least 0.02, in order to guarantee an aperture limit of at least $10\,\sigma$, whereas in this study an initial estimate of 0.1 was taken. This could be a goal of additional local corrections. Alternatively, the off-momentum characteristics of the nominal optics could be improved.

Vertical Plane

Figure 5.18 presents the beam-stay-clear values around the ring calculated for off-momentum particles in the vertical plane and Figure 5.19 presents a closer look at IPG, around which most of the bottlenecks are located. At higher beam energies, there are a few other elements around the lattice which also contain bottlenecks, corresponding to the positions of high β_y in Figure 5.20.

Table 5.5 summarises the vertical aperture bottlenecks for the off-momentum particles. Once again, the bare structure of the lattice has very liberal normalised aperture limits, whereas the majority of aperture bottlenecks calculated using the FCC-ee tolerances and HL-LHC tolerances are significantly less than $10\,\sigma$, with zero aperture in multiple elements. Of course, this is not acceptable in the machine. It should be noted that the use of BBEAT = 10 was only a first estimate for the vertical off-momentum calculations, and this number must be improved greatly. This motivates the need to start studying the optics corrections for off-momentum particles, with a limit of 5 being imposed on the residual beam size increase factor left after correction. Additionally, similar to the horizontal off-momentum case, the fractional vertical parasitic dispersion should be corrected to at least 0.02, as opposed to the initial estimate of 0.1, in order to guarantee normalised aperture limits that are well above $10\,\sigma$.

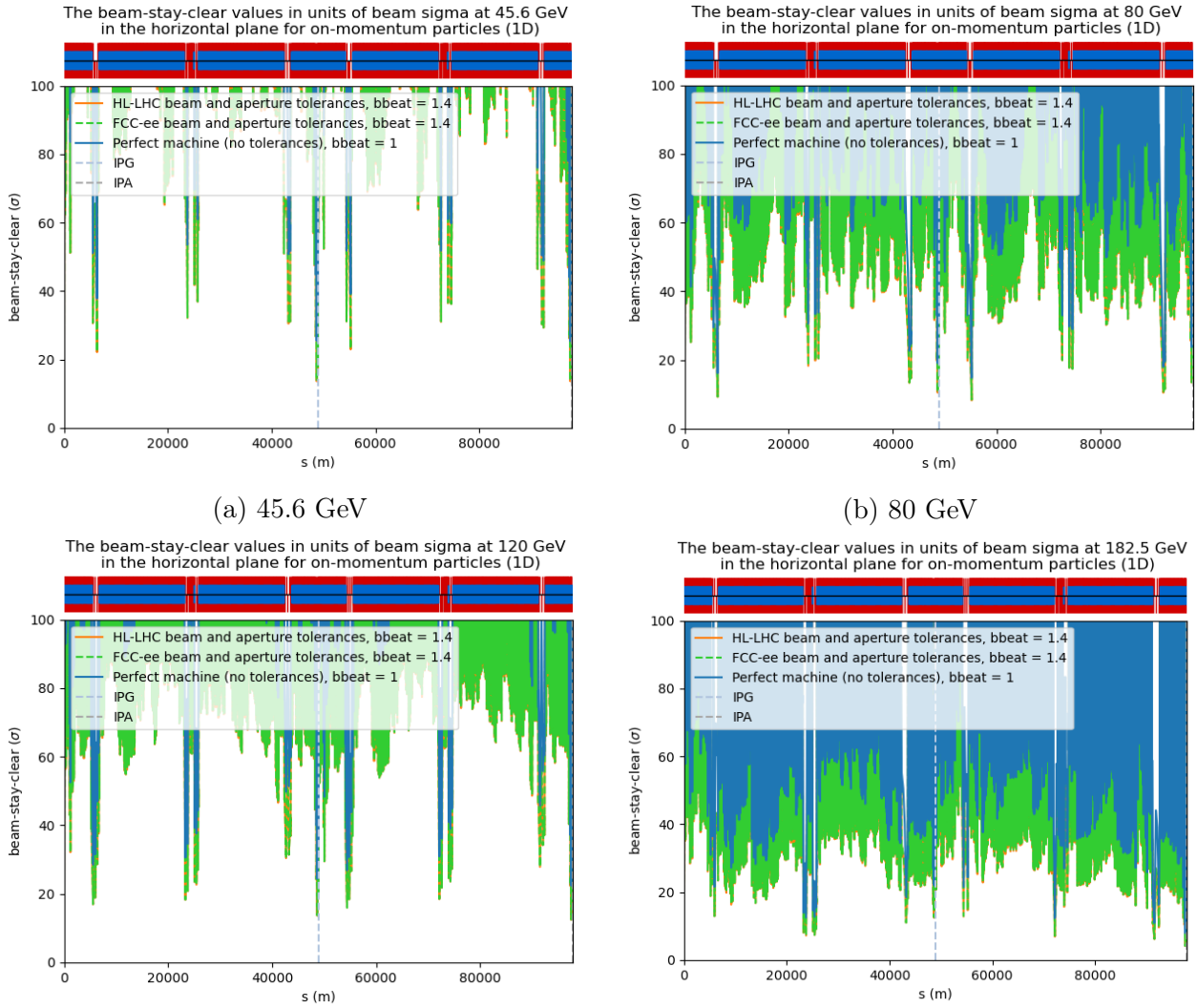

(a) 45.6 GeV

(b) 80 GeV

(c) 120 GeV

(d) 182.5 GeV

Figure 5.15: The beam-stay-clear around the full lattice for particles with an assumed momentum offset of 1% in the **horizontal** plane for each beam energy from the one dimensional calculation. The beam-stay-clear calculated using: 1) no errors is given in blue, 2) FCC-ee tolerances is given in green, 3) HL-LHC tolerances is given in orange. The positions of IPG and IPA have been marked, with the lattice starting from and beginning in the middle of IPA. Above each plot is a schematic diagram of the lattice layout: the central black line indicates drift space, the blue indicates dipoles, and the red elements above and below the drift space represent focusing and defocusing quadrupoles respectively.

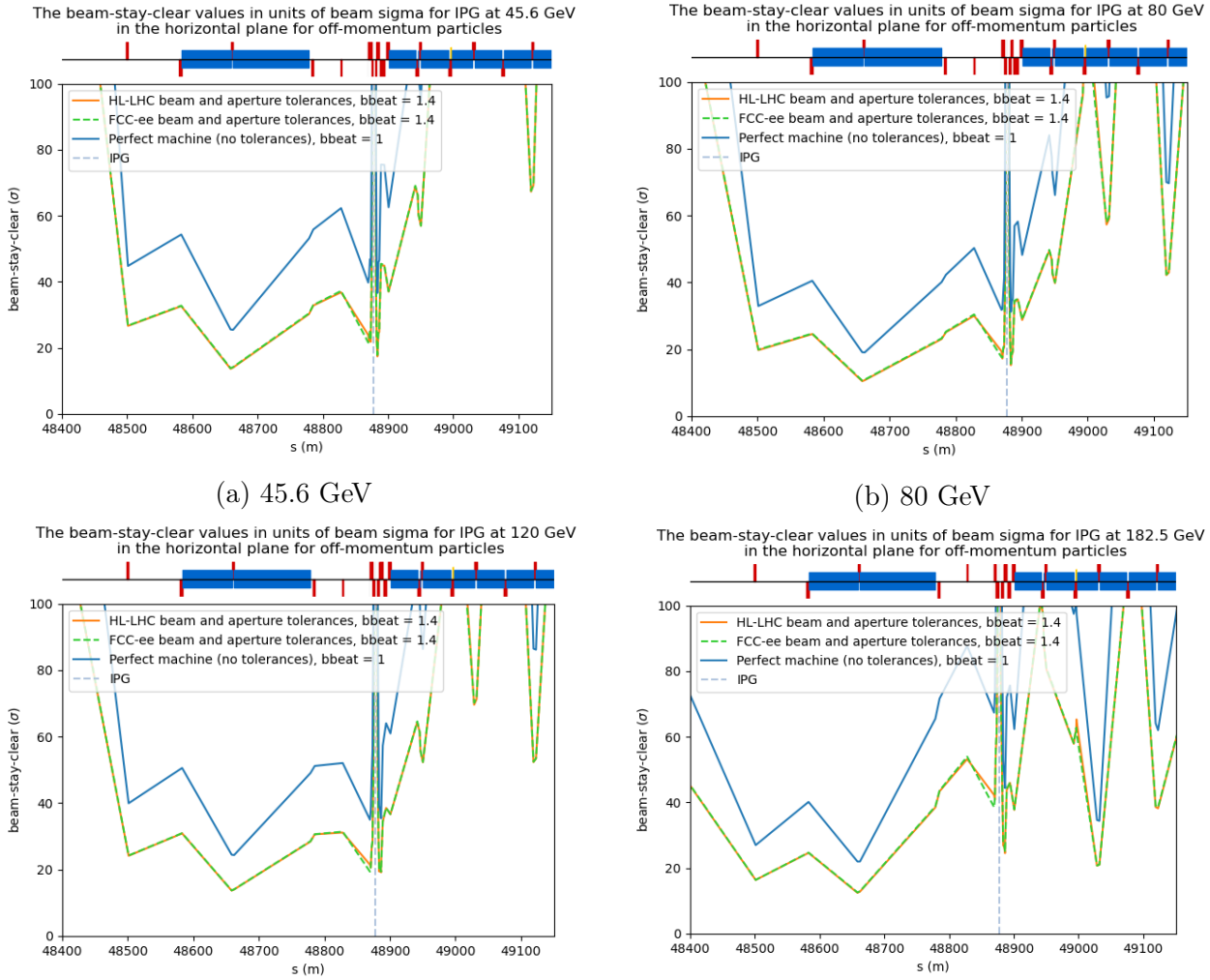

(a) 45.6 GeV

(b) 80 GeV

(c) 120 GeV

(d) 182.5 GeV

Figure 5.16: A close-up of the beam-stay-clear at the interaction point IPG (marked in light blue) for particles with an assumed momentum offset of 1% in the **horizontal** plane for each beam energy from the one dimensional calculation. In the 1D calculation, there is no slicing of elements, hence the normalised aperture is evaluated at the end of each element. The beam-stay-clear calculated using: 1) no errors is given in blue, 2) FCC-ee tolerances is given in green, 3) HL-LHC tolerances is given in orange. Above each plot is a schematic diagram of the lattice layout: the central black line indicates drift space, the blue indicates dipoles, and the red elements above and below the drift space represent focusing and defocusing quadrupoles respectively.

Beam Energy [GeV]	Element	Type	s [m]	beam-stay-clear (σ)		
				No Tolerance	FCC - ee Tolerances	HL - LHC Tolerances
45.6	BC1L.1	Dipole	48658.52735	25.52	13.79	**13.62**
	QC4L.1	Quadrupole	48662.32735	25.41	14.13	13.98
	BC1L.2	Dipole	97536.55949	25.43	**13.74**	13.62
	QC4L.2	Quadrupole	97540.35949	**25.32**	14.07	13.98
80	QN2.2	Quadrupole	6323.400603	16.09	9.27	9.20
	QM0.1	Quadrupole	43207.78292	22.64	13.41	13.30
	QM2.1	Quadrupole	43517.32158	24.64	14.67	14.60
	BC1L.1	Dipole	48658.52735	19.10	10.61	10.44
	QC4L.1	Quadrupole	48662.32735	19.02	10.86	10.71
	QN2.4	Quadrupole	55201.43274	**14.76**	**8.43**	**8.19**
	QM0.2	Quadrupole	92085.81506	17.99	10.47	10.42
	QM1.2	Quadrupole	92388.62606	22.47	13.30	13.27
	QM2.2	Quadrupole	92395.35372	19.58	11.48	11.44
	BC1L.2	Dipole	97536.55949	23.83	13.46	13.39
	QC4L.2	Quadrupole	97540.35949	23.72	13.77	13.72
120	BC1L.1	Dipole	48658.52735	24.42	13.68	13.61
	QC4L.1	Quadrupole	48662.32735	24.32	14.00	13.96
	BC1L.2	Dipole	97536.55949	22.41	**12.47**	**12.35**
	QC4L.2	Quadrupole	97540.35949	**22.32**	12.76	12.67
182.5	QU6.1	Quadrupole	23279.84396	13.85	8.07	7.96
	QU5.1	Quadrupole	23340.84929	22.64	13.63	13.53
	QU4.1	Quadrupole	23514.29479	21.24	12.74	12.67
	QU2.1	Quadrupole	23748.74561	12.46	7.19	7.15
	BI1.1	Dipole	25096.75838	14.75	8.44	8.35
	QI2.1	Quadrupole	25100.55838	14.54	8.51	8.43
	QI3.1	Quadrupole	25307.71655	23.27	14.03	13.97
	QI4.1	Quadrupole	25405.18119	12.70	7.35	7.30
	QI5.1	Quadrupole	25612.33937	19.85	11.86	11.83
	QI6.1	Quadrupole	25709.804	15.45	9.08	9.06
	QM0.1	Quadrupole	43207.78292	18.44	10.97	10.94
	BC1L.1	Dipole	48658.52735	21.95	12.54	12.40
	QC4L.1	Quadrupole	48662.32735	21.95	12.89	12.77
	QN2.3	Quadrupole	54398.70476	21.53	12.93	12.77
	QU6.2	Quadrupole	72157.87611	12.27	7.07	6.83
	QU5.2	Quadrupole	72218.88144	21.81	13.10	12.84
	QM5.2	Quadrupole	91217.60545	22.34	13.44	13.41
	QM4.2	Quadrupole	91224.33094	17.86	10.60	10.58
	QM3I.2	Quadrupole	91232.69348	18.87	11.25	11.23
	QM2I.2	Quadrupole	91535.49635	10.87	6.19	6.11
	QM1.2	Quadrupole	92388.62606	18.83	11.22	11.17
	QM2.2	Quadrupole	92395.35372	16.28	9.61	9.56
	BC3L.2	Dipole	97201.15428	21.23	12.45	12.24
	QY2L.4	Quadrupole	97204.95428	21.39	12.83	12.64
	QC6L.2	Quadrupole	97379.32201	17.59	10.43	10.36
	QC5L.2	Quadrupole	97460.96846	18.16	10.80	10.76
	BC1L.2	Dipole	97536.55949	7.91	**4.09**	**4.06**
	QC4L.2	Quadrupole	97540.35949	**7.86**	4.18	4.16
	BWL.2	Dipole	97656.83018	15.26	8.51	8.46
	QC3L.2	Quadrupole	97663.35831	15.80	9.09	9.05
	QT1L.2	Quadrupole	97705.99119	14.31	8.23	8.11
	QC2L2.2	Quadrupole	97748.87406	11.78	6.11	5.97
	QC2L1.2	Quadrupole	97750.20406	16.09	8.59	8.42
	QC1L3.2	Quadrupole	97751.50406	19.67	9.76	9.52

Table 5.4: Summary of the **horizontal** aperture bottlenecks for particles with an assumed momentum offset of 1% at each beam energy calculated in one dimension using no tolerances, the FCC-ee tolerances, and HL-LHC tolerances. The lowest beam-stay-clear values are in bold for each beam energy and tolerance set.

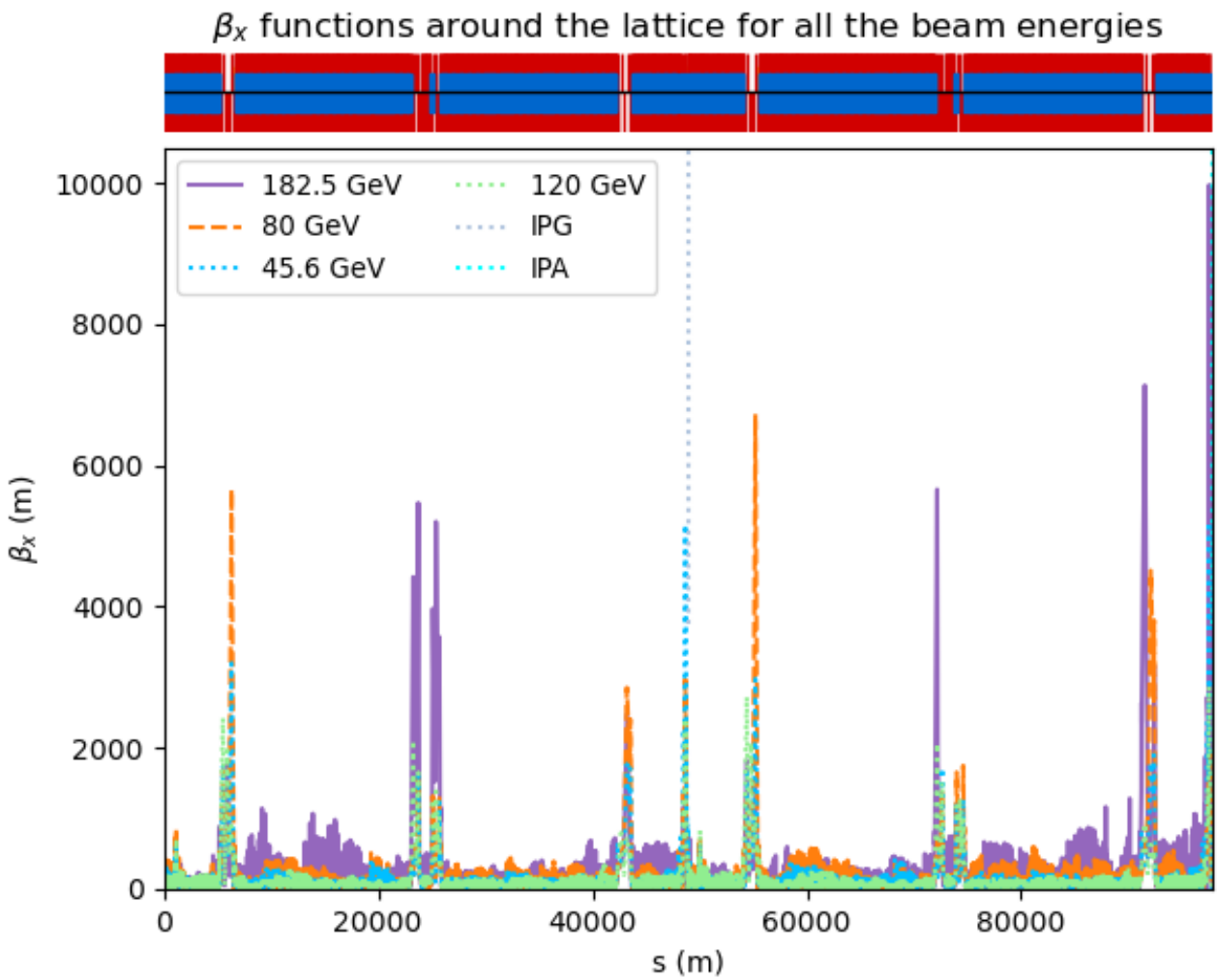

Figure 5.17: The β_x function around the ring for each of the beam energies for particles with an assumed momentum offset of 1%, with the positions of the interaction points IPG and IPA marked. Above the plot is a schematic diagram of the lattice layout: the central black line indicates drift space, the blue indicates dipoles, and the red elements above and below the drift space represent focusing and defocusing quadrupoles respectively.

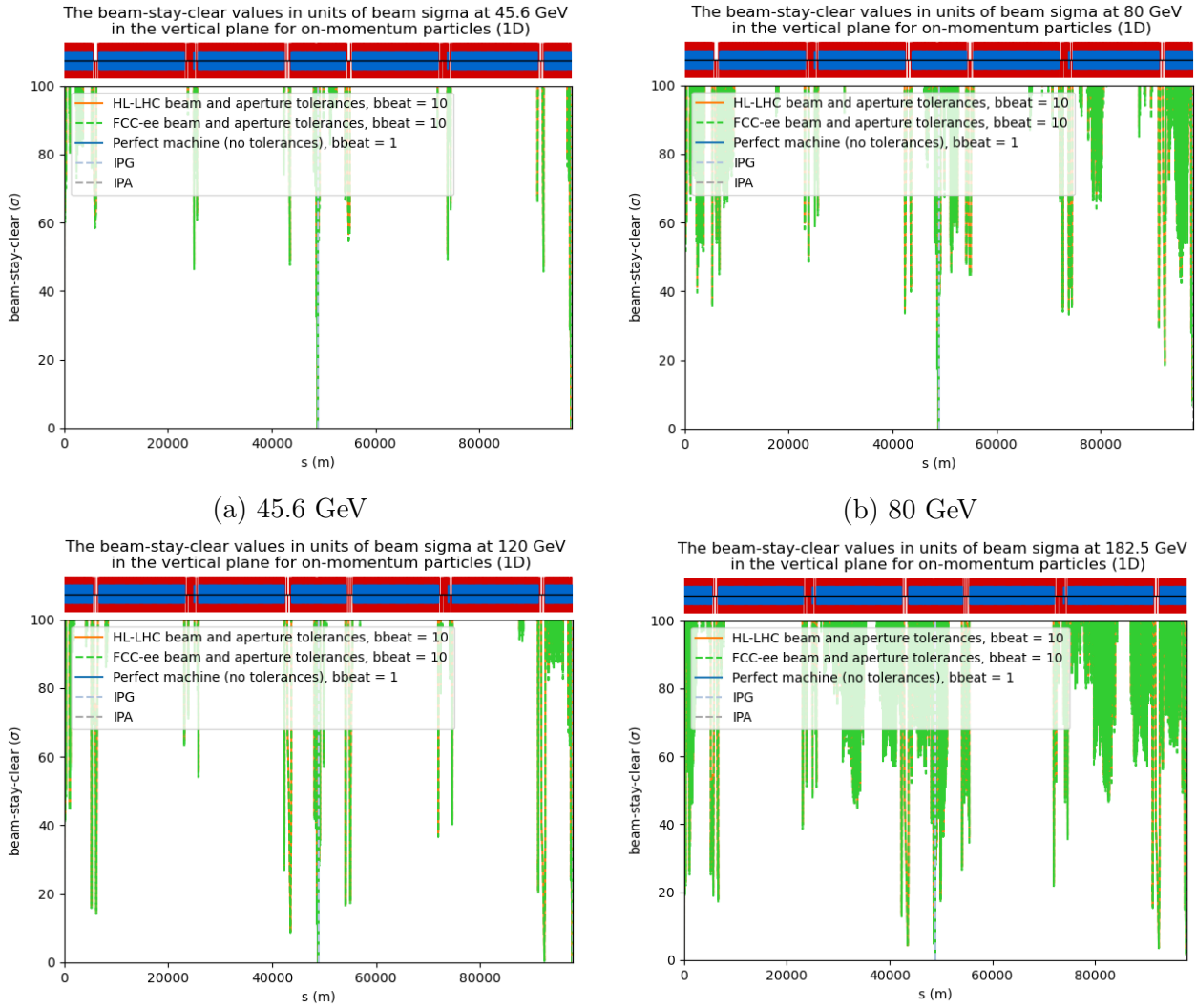

(a) 45.6 GeV

(b) 80 GeV

(c) 120 GeV

(d) 182.5 GeV

Figure 5.18: The beam-stay-clear around the full lattice for particles with an assumed momentum offset of 1% in the **vertical** plane for each beam energy from the one dimensional calculation. The beam-stay-clear calculated using: 1) no errors is given in blue, 2) FCC-ee tolerances is given in green, 3) HL-LHC tolerances is given in orange. The positions of IPG and IPA have been marked, with the lattice starting from and beginning in the middle of IPA. Above each plot is a schematic diagram of the lattice layout: the central black line indicates drift space, the blue indicates dipoles, and the red elements above and below the drift space represent focusing and defocusing quadrupoles respectively.

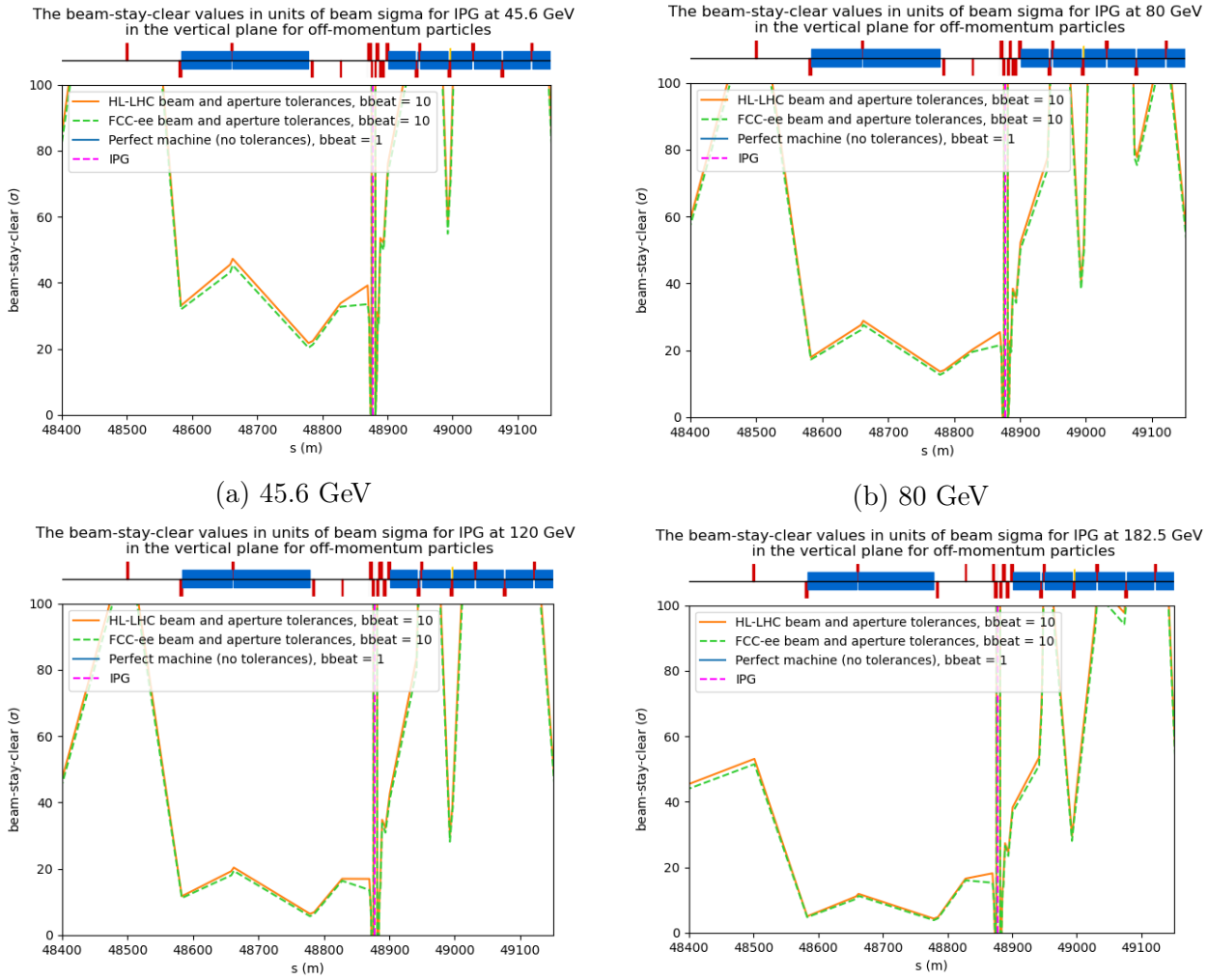

(a) 45.6 GeV

(b) 80 GeV

(c) 120 GeV

(d) 182.5 GeV

Figure 5.19: A close-up of the beam-stay-clear at the interaction point IPG (marked in pink) for particles with an assumed momentum offset of 1% **vertical** plane for each beam energy from the one dimensional calculation. In the 1D calculation, there is no slicing of elements, hence the normalised aperture is evaluated at the end of each element. The beam-stay-clear calculated using: 1) no errors is given in blue, 2) FCC-ee tolerances is given in green, 3) HL-LHC tolerances is given in orange. Above each plot is a schematic diagram of the lattice layout: the central black line indicates drift space, the blue indicates dipoles, and the red elements above and below the drift space represent focusing and defocusing quadrupoles respectively.

Beam Energy [GeV]	Element	Type	s [m]	beam-stay-clear (σ)		
				No Tolerance	FCC - ee Tolerances	HL - LHC Tolerances
45.6	QC1R1.1	Quadrupole	3.400225021	339.99	**0.00**	0.44
	QC1R2.1	Quadrupole	4.480225021	440.37	6.81	8.38
	QC1R3.1	Quadrupole	5.560225021	527.31	13.27	15.25
	QC1L3.1	Quadrupole	48873.47192	410.50	4.59	6.01
	QC1L2.1	Quadrupole	48874.55192	322.56	**0.00**	**0.00**
	QC1L1.1	Quadrupole	48875.83192	359.12	0.77	1.95
	QC1R1.2	Quadrupole	48881.43237	318.75	**0.00**	**0.00**
	QC1R2.2	Quadrupole	48882.51237	412.72	4.75	6.19
	QC1R3.2	Quadrupole	48883.59237	493.93	10.79	12.61
	QC1L3.2	Quadrupole	97751.50406	415.36	4.95	6.40
	QC1L2.2	Quadrupole	97752.58406	326.48	**0.00**	**0.00**
	QC1L1.2	Quadrupole	97753.86406	363.59	1.10	2.31
80	QC1R1.1	Quadrupole	3.400225021	290.65	1.72	2.70
	QC1R2.1	Quadrupole	4.480225021	332.50	4.83	6.01
	QC1R3.1	Quadrupole	5.560225021	409.56	10.56	12.10
	BWL.1	Dipole	48778.79803	385.75	12.65	13.60
	QC3L.1	Quadrupole	48785.32617	383.44	13.30	14.05
	QC1L3.1	Quadrupole	48873.47192	269.39	0.14	1.02
	QC1L2.1	Quadrupole	48874.55192	234.65	**0.00**	**0.00**
	QC1L1.1	Quadrupole	48875.83192	293.13	1.91	2.90
	QC1R1.2	Quadrupole	48881.43237	236.31	**0.00**	**0.00**
	QC1R2.2	Quadrupole	48882.51237	270.28	0.21	1.09
	QC1R3.2	Quadrupole	48883.59237	332.81	4.86	6.03
	QC1L3.2	Quadrupole	97751.50406	410.46	10.63	12.17
	QC1L2.2	Quadrupole	97752.58406	357.75	6.71	8.01
120	QC1R1.1	Quadrupole	3.400225021	248.86	**0.00**	**0.00**
	QC1R2.1	Quadrupole	4.480225021	258.69	**0.00**	**0.00**
	QC1R3.1	Quadrupole	5.560225021	311.97	0.45	1.48
	QN1.2	Quadrupole	6150.019429	416.11	14.07	14.69

Table 5.5 continued from previous page

	QM1.1	Quadrupole	43510.59392	354.69	8.64	9.10
	QC5L.1	Quadrupole	48582.93631	383.04	11.15	11.68
	BWL.1	Dipole	48778.79803	336.65	5.65	6.38
	QC3L.1	Quadrupole	48785.32617	335.89	6.33	6.88
	QC2L2.1	Quadrupole	48870.84192	419.24	11.08	12.15
	QC2L1.1	Quadrupole	48872.17192	351.97	5.65	6.48
	QC1L3.1	Quadrupole	48873.47192	212.72	**0.00**	**0.00**
	QC1L2.1	Quadrupole	48874.55192	198.49	**0.00**	**0.00**
	QC1L1.1	Quadrupole	48875.83192	267.60	**0.00**	**0.00**
	QC1R1.2	Quadrupole	48881.43237	199.52	**0.00**	**0.00**
	QC1R2.2	Quadrupole	48882.51237	207.40	**0.00**	**0.00**
	QC1R3.2	Quadrupole	48883.59237	250.13	**0.00**	**0.00**
	QC2R1.2	Quadrupole	48885.14237	427.99	11.78	12.89
	QM1.2	Quadrupole	92388.62606	260.23	0.28	0.50
	QM2.2	Quadrupole	92395.35372	308.82	4.58	4.92
	QC1L3.2	Quadrupole	97751.50406	295.60	**0.00**	0.18
	QC1L2.2	Quadrupole	97752.58406	275.83	**0.00**	0.00
	QC1L1.2	Quadrupole	97753.86406	371.91	4.91	6.21
182.5	QC1R1.1	Quadrupole	3.400225021	150.36	**0.00**	**0.00**
	QC1R2.1	Quadrupole	4.480225021	138.99	**0.00**	**0.00**
	QC1R3.1	Quadrupole	5.560225021	153.72	**0.00**	**0.00**
	QC2R1.1	Quadrupole	7.110225021	263.93	6.06	6.72
	QC2R2.1	Quadrupole	8.440225021	276.13	7.05	7.75
	QC3.1	Quadrupole	16.14027457	339.22	14.13	14.84
	QM5.1	Quadrupole	42339.57331	316.33	12.76	13.27
	QM1.1	Quadrupole	43510.59392	216.87	3.96	4.21
	QM2.1	Quadrupole	43517.32158	256.77	7.49	7.85
	QC5L.1	Quadrupole	48582.93631	225.52	4.73	5.00
	BC1L.1	Dipole	48658.52735	302.72	10.31	11.06
	QC4L.1	Quadrupole	48662.32735	305.79	11.24	11.85
	BWL.1	Dipole	48778.79803	225.58	3.80	4.29

Table 5.5 continued from previous page

	QC3L.1	Quadrupole	48785.32617	226.57	4.38	4.76
	QC2L2.1	Quadrupole	48870.84192	349.56	12.97	13.94
	QC2L1.1	Quadrupole	48872.17192	282.48	7.56	8.29
	QC1L3.1	Quadrupole	48873.47192	180.58	**0.00**	**0.00**
	QC1L2.1	Quadrupole	48874.55192	192.60	**0.00**	**0.00**
	QC1L1.1	Quadrupole	48875.83192	275.14	5.23	6.23
	QC1R1.2	Quadrupole	48881.43237	194.47	**0.00**	**0.00**
	QC1R2.2	Quadrupole	48882.51237	179.90	**0.00**	**0.00**
	QC1R3.2	Quadrupole	48883.59237	199.17	**0.00**	0.22
	QC2R1.2	Quadrupole	48885.14237	342.78	12.42	13.37
	QC2R2.2	Quadrupole	48886.47237	359.54	13.78	14.78
	QM1.2	Quadrupole	92388.62606	210.48	3.40	3.63
	QM2.2	Quadrupole	92395.35372	249.38	6.84	7.17
	BWL.2	Dipole	97656.83018	303.08	10.34	11.09
	QC3L.2	Quadrupole	97663.35831	303.54	11.05	11.65
	QC2L1.2	Quadrupole	97750.20406	341.98	12.36	13.30
	QC1L3.2	Quadrupole	97751.50406	218.25	1.00	1.73
	QC1L2.2	Quadrupole	97752.58406	232.55	2.06	2.86
	QC1L1.2	Quadrupole	97753.86406	331.84	9.44	10.71

Table 5.5: Summary of the **vertical** aperture bottlenecks for particles with an assumed momentum offset of 1% at each beam energy calculated in one dimension using no tolerances, the FCC-ee tolerances, and HL-LHC tolerances. The lowest beam-stay-clear values are in bold for each beam energy and tolerance set.

5.2 Momentum Acceptance Results

Figure 5.21 presents the maximum momentum acceptance around the lattice in the horizontal plane for each beam energy and Table 5.6 summarises the elements with the lowest maximum momentum acceptance. The lowest momentum acceptance at $8\,\sigma$ betatron amplitude ranges from 5.6%, the lowest at 182.5 GeV, to 6.1%, the highest at 45.6 GeV, all of which are well

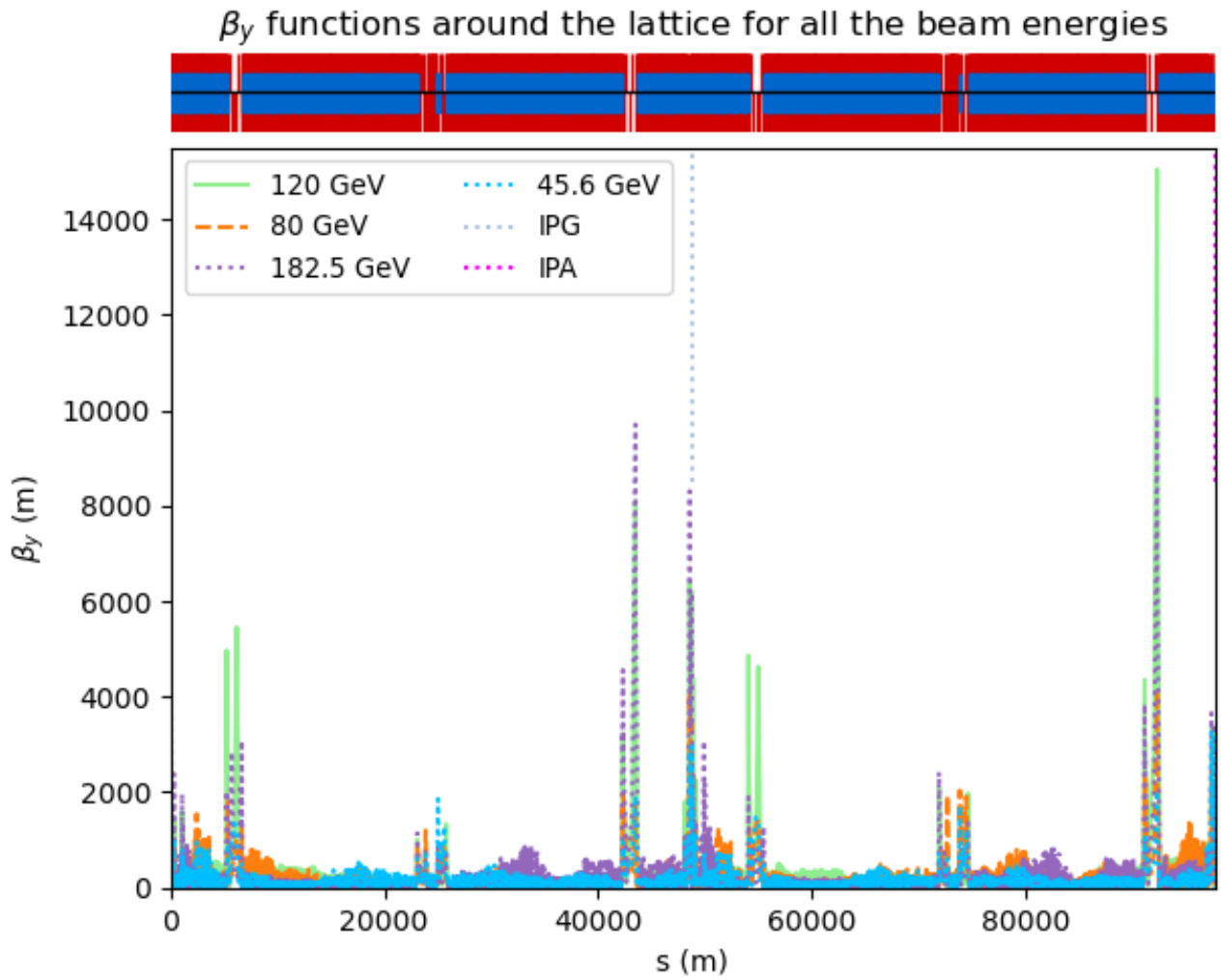

Figure 5.20: The β_y function around the ring for each of the beam energies for particles with an assumed momentum offset of 1%, with the positions of the interaction points IPG and IPA marked. Above the plot is a schematic diagram of the lattice layout: the central black line indicates drift space, the blue indicates dipoles, and the red elements above and below the drift space represent focusing and defocusing quadrupoles respectively.

above the required momentum acceptance defined in the design report [1], listed in Table 4.6. The momentum bottleneck is located at the quadrupoles QY2.1 and QY2.3, which are both located just after IPA and IPG respectively. The corresponding normalised aperture limits using the FCC-ee tolerances are around 150 σ, well above the previously mentioned horizontal aperture bottlenecks.

The corresponding momentum acceptances for the horizontal aperture bottlenecks for on-momentum particles in Table 5.2 are also much greater than the required momentum acceptance at each energy, so there are no bottlenecks in the momentum space.

Beam Energy [GeV]	Element	Type	s [m]	Momentum Acceptance - 0 σ	Momentum Acceptance - 7 σ	Momentum Acceptance - 8 σ	beam-stay-clear (σ)		
							No Tolerance	FCC - ee Tolerances	HL - LHC Tolerances
45.6	BC4.1	Dipole	150.4600956	0.065	0.062	0.062	171.79	150.42	134.97
	QY2.1	Quadrupole	154.2600956	**0.064**	**0.062**	**0.061**	166.97	149.19	134.27
	BG6.1	Dipole	1106.42093	0.078	0.074	0.073	142.69	124.95	112.12
	QG6.1	Quadrupole	1109.62093	0.077	0.074	0.073	145.05	129.61	116.64
	BC4.2	Dipole	49028.49224	0.065	0.062	0.062	171.79	150.42	134.97
	QY2.3	Quadrupole	49032.29224	**0.064**	**0.062**	**0.061**	166.97	149.19	134.27
	BG6.2	Dipole	49984.45307	0.078	0.074	0.073	142.69	124.95	112.12
	QG6.2	Quadrupole	49987.65307	0.077	0.074	0.073	145.05	129.61	116.64
80	BC4.1	Dipole	150.4600956	0.065	0.060	0.059	96.81	84.77	76.06
	QY2.1	Quadrupole	154.2600956	**0.064**	**0.059**	**0.059**	94.10	84.08	75.67
	BG6.1	Dipole	1106.42093	0.078	0.071	0.070	81.42	71.29	63.97
	QG6.1	Quadrupole	1109.62093	0.077	0.071	0.070	82.73	73.93	66.53
	BC4.2	Dipole	49028.49224	0.065	0.060	0.059	96.81	84.77	76.06
	QY2.3	Quadrupole	49032.29224	**0.064**	**0.059**	**0.059**	94.10	84.08	75.67
	BG6.2	Dipole	49984.45307	0.078	0.071	0.070	81.42	71.29	63.97
	QG6.2	Quadrupole	49987.65307	0.077	0.071	0.070	82.73	73.93	66.53
120	BC4.1	Dipole	150.4600956	0.065	0.061	0.060	112.09	98.15	88.07
	QY2.1	Quadrupole	154.2600956	**0.064**	**0.060**	**0.060**	110.12	98.40	88.56
	BC4.2	Dipole	49028.49224	0.065	0.061	0.060	112.09	98.15	88.07
	QY2.3	Quadrupole	49032.29224	**0.064**	**0.060**	**0.060**	110.12	98.40	88.56
175	BC4.1	Dipole	150.4600956	0.065	0.058	0.057	67.70	59.28	53.20
	QY2.1	Quadrupole	154.2600956	**0.064**	**0.057**	**0.057**	67.07	59.93	53.93
	BC4.2	Dipole	49028.49224	0.065	0.058	0.057	67.70	59.28	53.20
	QY2.3	Quadrupole	49032.29224	**0.064**	**0.057**	**0.057**	67.07	59.93	53.93
182.5	BC4.1	Dipole	150.4600956	0.065	0.058	0.057	64.86	56.79	50.96
	QY2.1	Quadrupole	154.2600956	**0.064**	**0.057**	**0.056**	64.25	57.41	51.67
	BC4.2	Dipole	49028.49224	0.065	0.058	0.057	64.86	56.79	50.96
	QY2.3	Quadrupole	49032.29224	**0.064**	**0.057**	**0.056**	64.25	57.41	51.67

Table 5.6: Summary of the elements with the lowest maximum momentum acceptance in the **horizontal** plane using zero, seven and eight sigma betatron amplitudes, with the corresponding beam-stay-clear values calculated in MAD-X using no tolerances, FCC-ee tolerances, and HL-LHC tolerances. The lowest momentum acceptance for each beam energy and betatron amplitude are in bold.

5.3 Collimator Cuts

The results of the aperture calculations presented above involve only the first estimates of the FCC-ee tolerances. There should be future iterations of these studies using improved

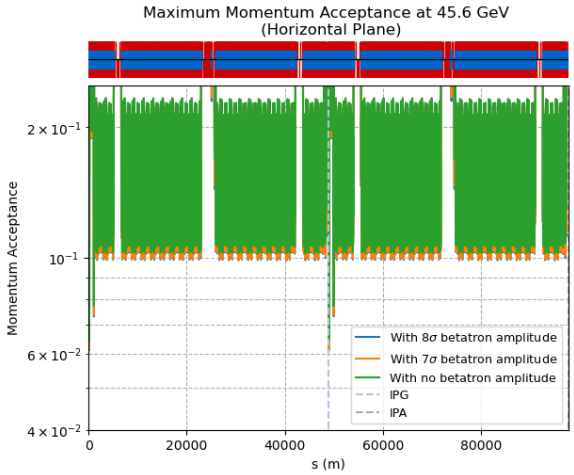

(a) 45.6 GeV

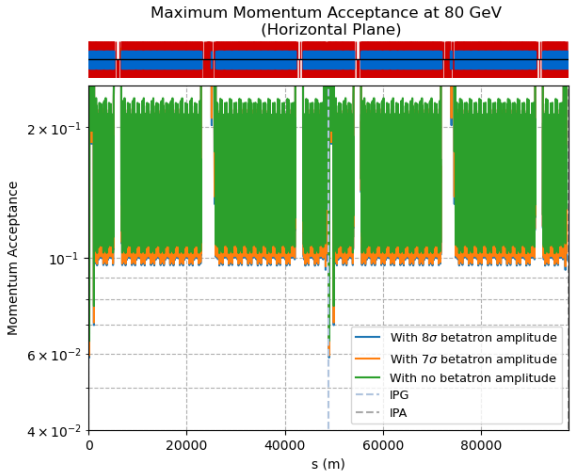

(b) 80 GeV

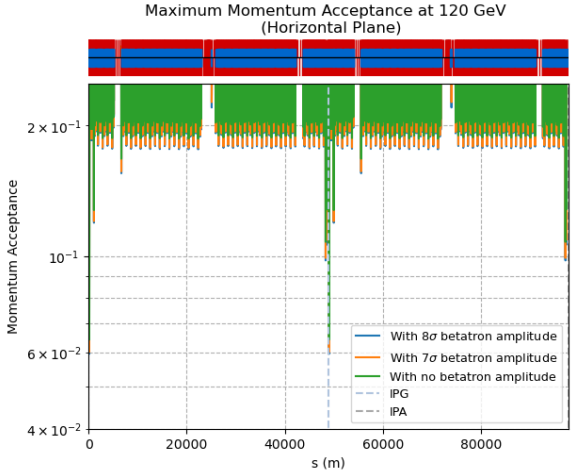

(c) 120 GeV

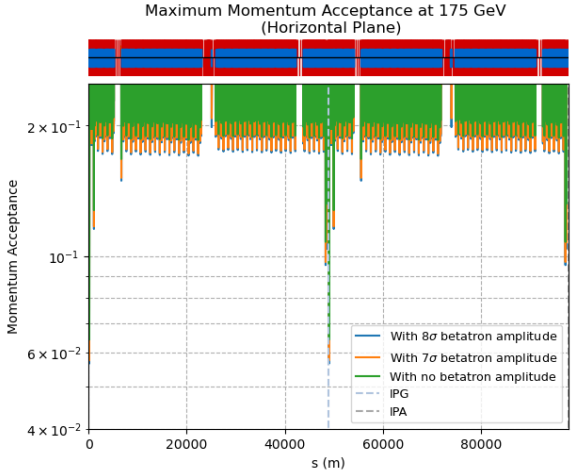

(d) 175 GeV

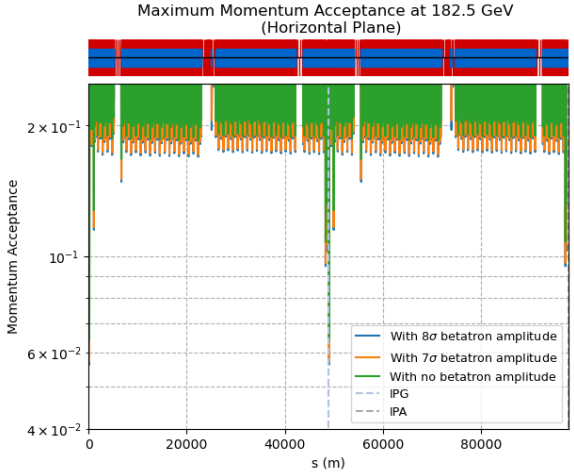

(e) 182.5 GeV

Figure 5.21: The momentum acceptance around the ring in the **horizontal** plane for each beam energy. The momentum acceptance calculated using: 1) no betatron amplitude is given in green, 2) 7 sigma betatron amplitude is given in orange, 3) 8 sigma betatron amplitude is given in blue. The positions of IPG and IPA have been marked, with the lattice starting from and beginning in the middle of IPA. Above each plot is a schematic diagram of the lattice layout: the central black line indicates drift space, the blue indicates dipoles, the red elements above and below the drift space represent focusing and defocusing quadrupoles respectively.

corrections, in particular once the local optics corrections have been performed and the off-momentum corrections are more mature, and also taking into account other beam growth effects such as the beam-beam effect. Nevertheless, the above results give an overview of the aperture that has to be protected, and allows us to define a first guess on the required collimator cuts, in other words, the placement of the collimator jaw openings.

The lowest normalised aperture bottleneck for on-momentum particles in the horizontal plane was around $14.88\,\sigma$, therefore a first minimum estimate for the betatron collimator cuts at $12\,\sigma$ can be proposed. As for the vertical plane for on-momentum particles, the lowest aperture bottleneck was found to be around $10.26\,\sigma$, so a first minimum estimate of $8\,\sigma$ can be proposed for the collimator cuts. These two estimates would allow room to place the collimators and guarantee beam lifetime. The off-momentum aperture studies must be more refined in order to propose collimator cuts that also accounts for the off-momentum aperture bottlenecks.

As for the momentum space, the lowest momentum bottleneck was 5.6%, and the maximum required momentum acceptance is 2.4% in order to guarantee beam lifetime at the interaction points, therefore a momentum cut can be proposed at 3%, which would provide some operational margins for both beam lifetime and aperture protection.

Chapter 6

Conclusion

With the total beam-stored energy reaching values of up to 20 MJ in the FCC-ee, there is a need for halo collimation to protect elements in the machine from severe damage. The purpose of this work was to study the halo collimation requirements in the FCC-ee at the different foreseen center of mass energies.

The first aim was to create an aperture model of the lattice that can be used to study the available normalised aperture around the ring for on-momentum and off-momentum particles. The aperture model was created by implementing a circular vacuum chamber with a radius of 35 mm into the remaining arc sections of the existing aperture model, where only the apertures for the experimental insertions, IRA and IRG, were defined. This is the foreseen design for the present ring layout and no element is expected to have an aperture below this level, meaning this is a conservative assumption. Figure 4.1 presents the aperture model and in future work, the model can be adjusted to include the antechambers (see Figure 4.2).

This aperture model was then used to calculate the available aperture, normalised to the local betatronic RMS beam size, around the ring as beam-stay-clear values in units of beam sigma using the aperture command in MAD-X. The aperture command takes mechanical tolerances, which refer to the misalignment of elements around the ring, and beam tolerance parameters, referring to uncertainties in beam size and position, as input to define the errors it uses when calculating the available normalised aperture. The first estimates of the FCC-ee mechanical tolerances are presented in Table 4.2 and were computed from the misalignment tolerances presented in the global optics correction results in [20], from which the first estimates on the

FCC-ee beam tolerances were also derived as part of this work, detailed in Chapter 4. The available normalised aperture was then calculated using three different tolerance sets; firstly, for an ideal machine with no errors (no mechanical or beam tolerances), in order to get the bare lattice acceptance, secondly, using the FCC-ee mechanical and beam tolerances, and finally using the HL-LHC mechanical and beam tolerances for comparison. The available normalised aperture was also investigated for particles with the nominal momentum and for particles with a 1% deviation from the nominal momentum in the horizontal and vertical planes at each beam energy, all of which were also calculated using a one-dimensional standalone calculation as a comparison to the MAD-X results.

The next aim was to identify potential performance bottlenecks and use these results to propose an initial estimate of the required collimator cuts (the placement of the collimator jaw openings). This is detailed in Chapter 5: The normalised aperture bottlenecks are located in elements surrounding the interaction points, IPG and IPA, in the horizontal and vertical planes for the on-momentum particles. In the horizontal plane, the lowest aperture bottleneck was $14.88\,\sigma$, and in the vertical plane it was $10.26\,\sigma$. In practical terms, a minimum of $8\,\sigma$ is required in order to guarantee a smooth operation without a strong lifetime degradation. So if the openings of the collimator jaws are to be placed at $8\,\sigma$ as an initial estimate, this would mean that the available normalised aperture must be at least $10\,\sigma$ in order to fit the collimators. From experience, ideally, the minimum aperture should be a few beam σ larger to accommodate for operational margins. Therefore, a first estimate of the betatron collimator cuts of $12\,\sigma$ and $8\,\sigma$ is proposed for the horizontal and vertical planes respectively. It should be noted that the 1D calculations also produced agreeing results; the calculation is only valid when the aperture bottleneck fully lies in the plane that is being considered, which was found to be the case, confirming the validity and reliability of the calculation.

The results for particles with momentum deviations were calculated only using the 1D calculation due to issues with the off-momentum calculations in the MAD-X tool, and these studies should be further extended in the future to complete the investigation. For both planes, the aperture bottlenecks are located mostly at the interaction regions, IRA and IRG, but appear elsewhere around the lattice at higher beam energies. Numerous bottlenecks have normalised aperture limits which are less than $10\,\sigma$, with some as low as $4\,\sigma$ in the horizontal plane, going down to $0\,\sigma$ at multiple locations in the vertical plane. This is because the estimates used for

the beam size growth parameter came from very preliminary off-momentum optics studies, for which the local optics corrections are yet to be performed. Clearly, such low apertures are unacceptable and the machine simply cannot function, therefore, the residual beam size increase factor must be limited to 1.2 and 5.0 in the horizontal and vertical planes respectively, and the fractional parasitic dispersion must be corrected to at least 0.02 for both planes, in order to obtain normalised aperture limits above $10\,\sigma$. This could be the goal of the local optics corrections that should be carried out in the future.

The available aperture around the ring was also studied in momentum space by using a one dimensional calculation to calculate the maximum momentum acceptance around the ring for each operational beam energy, detailed in Chapter 3. Using a betatron amplitude of $8\,\sigma$, the lowest maximum momentum acceptance ranges from 5.6% to 6.1% across all the beam energies, which is well above the required momentum acceptances specified in the design report, listed in Table 4.6. The lowest momentum bottleneck was 5.6% and the maximum required momentum acceptance is 2.4%, therefore a momentum cut can be proposed at 3% to accommodate for operational margins as well as guarantee aperture protection with significant margins.

The work presented here provides a first overview of the aperture that needs to be protected in the FCC-ee, using initial estimates for the FCC-ee tolerance parameters. Future iterations of this work should be carried out once the off-momentum optics corrections are more mature and a viable off-momentum optics is available, for example once the local optics corrections have been performed and other effects have been accounted for, such as the strong beam-beam effects which also contributes to beam growth. The issues with the MAD-X off-momentum calculations should also be investigated. In future work, the tilting of the beam ellipse in the physical $x - y-$space and its impact on the aperture limits should be studied, which would require a new version of MAD-X that can incorporate this.

Acknowledgements

Firstly, I would like start off by thanking my supervisors: Roderik Bruce, for his guidance, patience and kindness; having the opportunity to work at CERN was a daunting yet exciting experience, and he was very approachable and welcoming. Many thanks to Tatiana Pieloni for her guidance, organisation and encouragement throughout the project.

CERN truly embodies the spirit of scientific collaboration, and so I have numerous other researchers to thank. Thank you to Andrey Abramov for his help throughout the project, in particular with python and MAD-X debugging, and thank you to Stefano Redaelli for his feedback and discussions, and for proofreading my French abstract. Many thanks to Tessa Charles, Michael Hofer, and Tobias Persson for their work in providing us with the first estimates of errors. Thank you to Frank Zimmermann and Roberto Kersevan for answering our questions on the optics design and for their useful inputs and discussions. And many thanks also to Rogelio Tomas Garcia, Leon Van Riesen-Haupt, Helmut Burkhardt, Ghislain Roy, Katsunobu Oide, and Manuela Boscolo for their useful suggestions and discussions.

Next, I would like thank Professor Mike Seidel, who taught the Introduction to Particle Accelerators module at EPFL, which I thoroughly enjoyed. It was actually through Professor Seidel that I found this project, therefore, I extend my gratitude to him. Alongside, there is also Werner Herr, whom I would like to thank for helping me with learning MAD-X at the beginning of this project, and for answering my many questions. From Imperial, I would like to thank Professor Gavin Davies for coordinating the Year Abroad programme so well, and for his support during the year. I would also like to acknowledge the pastoral and academic support from my personal tutor, Professor Fay Dowker, who kept in touch with me throughout my year abroad and supported me through many applications. My heartiest thanks to her.

Finally, I have many people to thank on a personal level. First and foremost, I express my heartfelt gratitude to my parents, Rituparna Bhattacharyya and Jayanta Biswa Sarma, for believing in me, encouraging me, and doing everything possible in their capacity so that I may study well and do this project. Next, I would like to thank my brother and the rest of my family for their constant well-wishes, love and support. Many thanks to my friends, Maxime Chevalier and Melissa Faggella, for also proofreading my French abstract. Finally, I extend my gratitude to my friends, Tejasva Malhotra, the 'Gita Gang', my flatmate Maria Tsagkri, Max Leftley, and the rest of my Imperial crew, who were crucial in helping me get through this year.

Appendix A

Total Stored Beam Energy for Different Lepton Colliders

Table A.1 summarises the machine parameters [1, 6, 3, 23, 24] needed to calculate the total stored beam energy for different lepton colliders.

Machine	**Maximum Energy (GeV)**	**No. of Bunches**	**No. of Particles per Bunch**	**Total Beam Energy (GeV)**	**Total Beam Energy (MJ)**
LEP 2	96	8	4.86×10^{11}	3.73×10^{14}	0.06
SuperKEKB (for e-)	7.007	2500	6.53×10^{10}	1.14×10^{15}	0.18
SuperKEKB (for e+)	4	2500	9.04×10^{10}	9.04×10^{14}	0.14
HERA (leptons)	27.5	189	4.00×10^{10}	2.08×10^{14}	0.03
PEP II (e-)	9	1658	4.00×10^{10}	5.97×10^{14}	0.10
PEP II (e+)	3.1	1658	6.00×10^{10}	3.08×10^{14}	0.05
FCC-ee: 182.5 GeV	182.5	48	2.30×10^{11}	2.01×10^{15}	0.32
FCC-ee: 175 GeV	175	59	2.20×10^{11}	2.27×10^{15}	0.36
FCC-ee: 120 GeV	120	328	1.80×10^{11}	7.08×10^{15}	1.13
FCC-ee: 80 GeV	80	2000	1.50×10^{11}	2.40×10^{16}	3.84
FCC-ee: 45.6 GeV	45.6	16640	1.70×10^{11}	1.29×10^{17}	20.66

Table A.1: The parameters required to calculated the total stored beam energy for various lepton colliders.

Bibliography

[1] A. Abada et al. FCC-ee: The Lepton Collider. *The European Physical Journal Special Topics*, 228(2):261–623, Jun 2019. doi: 10.1140/epjst/e2019-900045-4.

[2] S. Redaelli. Beam Cleaning and Collimation Systems. *2014 Joint International Accelerator School: Beam Loss and Accelerator Protection, Proceedings*, pages 403–437, aug 2016. doi: 10.5170/CERN-2016-002.403. URL http://arxiv.org/abs/1608.03159.

[3] K. Akai, K. Furukawa, and H. Koiso. Superkekb collider. *Nuclear Instruments and Methods in Physics Research Section A: Accelerators, Spectrometers, Detectors and Associated Equipment*, 907:188–199, 2018. ISSN 0168-9002. doi: https://doi.org/10.1016/j.nima.2018.08.017. URL https://www.sciencedirect.com/science/article/pii/S0168900218309616. Advances in Instrumentation and Experimental Methods (Special Issue in Honour of Kai Siegbahn).

[4] T. Ishibashi, S. Terui, Y. Suetsugu, K. Watanabe, and M. Shirai. Movable collimator system for superkekb. *Phys. Rev. Accel. Beams*, 23:053501, May 2020. doi: 10.1103/PhysRevAccelBeams.23.053501. URL https://link.aps.org/doi/10.1103/PhysRevAccelBeams.23.053501.

[5] H. Wiedemann. *Particle Accelerator Physics*. Springer, third edition, 2007.

[6] Carlo Wyss. *LEP design report, v.3: LEP2*. CERN, Geneva, 1996. URL https://cds.cern.ch/record/314187. Vol. 1-2 publ. in 1983-84.

[7] S. G. DeBarger, S. G. Metcalfe, C. G. Ng, T. G. Porter, J. G. Seeman, M. G. Sullivan, and U. G. Wienands. The pep-ii movable collimators, Mar 2006. URL https://digital.library.unt.edu/ark:/67531/metadc877307/.

[8] P.M. Lewis, I. Jaegle, H. Nakayama, A. Aloisio, F. Ameli, M. Barrett, A. Beaulieu, L. Bosisio, P. Branchini, T.E. Browder, A. Budano, G. Cautero, C. Cecchi, Y.-T. Chen, K.-N. Chu, D. Cinabro, P. Cristaudo, S. de Jong, R. de Sangro, G. Finocchiaro, J. Flanagan, Y. Funakoshi, M. Gabriel, R. Giordano, D. Giuressi, M.T. Hedges, N. Honkanen, H. Ikeda, T. Ishibashi, H. Kaji, K. Kanazawa, C. Kiesling, S. Koirala, P. Križan, C. La Licata, L. Lanceri, J.-J. Liau, F.-H. Lin, J.-C. Lin, Z. Liptak, S. Longo, E. Manoni, C. Marinas, K. Miyabayashi, E. Mulyani, A. Morita, M. Nakao, M. Nayak, Y. Ohnishi, A. Passeri, P. Poffenberger, M. Ritzert, J.M. Roney, A. Rossi, T. Röder, R.M. Seddon, I.S. Seong, J.-G. Shiu, F. Simon, Y. Soloviev, Y. Suetsugu, M. Szalay, S. Terui, G. Tortone, S.E. Vahsen, N. van der Kolk, L. Vitale, M.-Z. Wang, H. Windel, and S. Yokoyama. First measurements of beam backgrounds at superkekb. *Nuclear Instruments and Methods in Physics Research Section A: Accelerators, Spectrometers, Detectors and Associated Equipment*, 914:69–144, 2019. ISSN 0168-9002. doi: https://doi.org/10.1016/j.nima.2018.05.071. URL `https://www.sciencedirect.com/science/article/pii/S0168900218306909`.

[9] P. Schmüser. Basic course on accelerator optics. 1987. doi: 10.5170/CERN-1987-010.1. URL `https://cds.cern.ch/record/370628`.

[10] S. Myers. *Particle Physics Reference Library: Volume 3: Accelerators and Colliders*, volume 3. Springer Nature, 2020.

[11] L. Z. Rivkin. Introduction to dynamics of electrons in rings in the presence of radiation. 1998. doi: 10.5170/CERN-1998-004.45. URL `https://cds.cern.ch/record/375974`.

[12] F. Tecker. Longitudinal beam dynamics. pages 1–22. 21 p, 2014. doi: 10.5170/CERN-2014-009.1. URL `https://cds.cern.ch/record/1982417`. 21 pages, contribution to the CAS - CERN Accelerator School: Advanced Accelerator Physics Course, Trondheim, Norway, 18-29 Aug 2013.

[13] M. A. V. García and F. Zimmermann. Beam blow up due to beamstrahlung in circular e^+e^- colliders. 2019. URL `https://arxiv.org/pdf/1911.03420.pdf`.

[14] G. Robert-Demolaize. *Design and Performance Optimization of the LHC Collimation System*. PhD thesis, Universite Joseph Fourier, Grenoble, 2006.

[15] L. Deniau, E. Forest, H. Grote, and F. Schmidt. Mad-x user's guide, 2020. URL `http://mad.web.cern.ch/mad/webguide/manual.html`.

[16] M. Luckhof. Fcc-ee optics files, cern gitlab respository. https://gitlab.cern.ch/fcc-optics/FCC-ee-lattice/-/tree/2851dbd9c69d5876552a6802137bdbb28abda6f9/Optics, 2019. GitLab revision number: 2851dbd9c69d5876552a6802137bdbb28abda6f9.

[17] R. Bruce, R. de Maria, S. Fartoukh, M. Giovannozzi, S. Redaelli, R. Tomas, and J. Wenninger. Parameters for HL-LHC aperture calculations. *CERN Report CERN-ACC-2014-0044*, 2014. URL http://cds.cern.ch/record/1697805?ln=en.

[18] J.B. Jeanneret and R. Ostojic. Geometrical acceptance in LHC version 5.0. *LHC Project Note 111, CERN*, 1997. URL http://cdsweb.cern.ch/record/691826?ln=en.

[19] M. Sands. The Physics of Electron Storage Rings: An Introduction. *Conf. Proc. C*, 6906161:257–411, 1969. URL https://inspirehep.net/files/0f9249be89a808732c1451100b84d55a.

[20] T. Charles. Summary of beta-beating & orbit after global corrections, 2021. URL https://indico.cern.ch/event/1017226/contributions/4269347/attachments/2211950/3743714/March2021.pdf.

[21] R. Bruce, C. Bracco, R. De Maria, M. Giovannozzi, S. Redaelli, R. Tomas, F. Velotti, and J. Wenninger. Updated parameters for hl-lhc aperture calculations for proton beams. *CERN-ACC-2017-0051*, 2017. URL https://cds.cern.ch/record/2274330?ln=en.

[22] T. Charles. Status of fcc-ee tuning studies, 2021. URL https://indico.cern.ch/event/1032213/contributions/4334651/attachments/2234808/3787647/LNO_04_2021.pdf.

[23] B.J. Holzer. HERA: Lessons learned from the HERA upgrade. page 5 p, 2009. doi: 10.5170/CERN-2009-004.30. URL https://cds.cern.ch/record/1204549.

[24] A Hutton and MS Zisman. Pep-ii: an asymmetric b factory based on pep. *IEEE*, 1:84–86, 1991. URL http://accelconf.web.cern.ch/p91/PDF/PAC1991_0084.PDF.